

Extending the QuikSCAT Data Record with the  
Oceansat-2 Scatterometer

Joshua P. Bradley

A thesis submitted to the faculty of  
Brigham Young University  
in partial fulfillment of the requirements for the degree of  
Master of Science

David G. Long, Chair  
Richard W. Christiansen  
D. J. Lee

Department of Electrical and Computer Engineering  
Brigham Young University  
August 2012

Copyright © 2012 Joshua P. Bradley  
All Rights Reserved



## ABSTRACT

### Extending the QuikSCAT Data Record with the Oceansat-2 Scatterometer

Joshua P. Bradley  
Department of Electrical and Computer Engineering  
Master of Science

Originally designed for wind velocity estimation over the ocean, scatterometers have since been applied to climate studies of the Earth's cryosphere and biosphere. As an integral part of climatological studies of the planet, the NASA Scatterometer Climate Record Pathfinder (SCP) supplies scatterometer-based products designed to aid researchers in climatological studies of the planet. In this thesis, necessary steps are taken to facilitate data from the Oceansat-2 Ku-band scatterometer (OSCAT) to be used in extending the Ku-band SCP dataset of conically scanning pencil-beam scatterometers begun by the Seawinds scatterometer flown on the QuikSCAT mission 1999-2009.

As a standard SCP product, a temporal resolution enhancement technique for the scatterometer image reconstruction (SIR) algorithm is applied to OSCAT data. A relative cross-calibration method is developed to ensure consistency amongst datasets of conically scanning pencil-beam scatterometers in the SCP data time series. By application of the method, both raw data and SIR image data of OSCAT is cross-calibrated with QuikSCAT. To enable creation of SCP products requiring knowledge of the spatial response function (SRF) with OSCAT data, a method of estimating the SRF of pencil-beam scatterometers is developed. The estimation method employs rank-reduced least-squares to invert the radar equation using measurements over islands. A simulation is performed to validate the efficacy of the method and provide optimum choice of island size and number of singular values used in rank-reduced least-squares. The utility of the SRF estimates is demonstrated by applying an estimate of the OSCAT SRF to SIR image construction with OSCAT data.

Keywords: OSCAT, QuikSCAT, SIR algorithm, scatterometer calibration, local time of day processing, spatial response function



## ACKNOWLEDGMENTS

Special thanks be to Dr. Long for all of the hard work he has done in making this thesis come to fruition. He believed in me enough to let me take on the assignment of preparing OSCAT for use in the MERS lab. Through his mentoring I was able to develop the skills and knowledge necessary to complete this thesis and enter into the workplace confidently.

Special thanks to my parents for being there for me in any capacity necessary at the time. I thank them for raising me to have the tenacity to accomplish great things and be a self-reliant individual.

I couldn't have done this without the constant support of my wife, including delicious lunches, moral support, and selflessly looking after our son Morgan, who is the joy of our lives.

Thanks to NASA JPL for funding the work done here in the MERS lab, and ISRO for creating OSCAT. Without either of them I would not have had a job or such an interesting project to work on.

Also, thanks to the other research students and faculty of the MERS lab that helped to maintain sanity and lend a helping hand when needed.



# Table of Contents

<b>List of Tables</b>	<b>xi</b>
<b>List of Figures</b>	<b>xiii</b>
<b>1 Introduction</b>	<b>1</b>
1.1 Thesis Statement . . . . .	2
1.2 Thesis Organization . . . . .	4
<b>2 Background</b>	<b>5</b>
2.1 Scatterometer Fundamentals . . . . .	5
2.1.1 Post-launch Scatterometer Calibration . . . . .	6
2.2 Instrument Description . . . . .	8
2.2.1 Data Description . . . . .	11
2.3 Scatterometer Climate Record Pathfinder . . . . .	11
2.3.1 Scatterometer Image Reconstruction (SIR) . . . . .	12
<b>3 Local Time of Day Processing with OSCAT</b>	<b>15</b>
3.1 Local Time of Day Characteristics of OSCAT . . . . .	16
3.2 Local Time of Day Comparison between Scatterometers . . . . .	18
3.3 Local Time of Day Images . . . . .	23
3.4 Summary . . . . .	23

<b>4</b>	<b>Relative Cross-calibration</b>	<b>29</b>
4.1	Sampling Region . . . . .	30
4.1.1	Data Selection Mask . . . . .	31
4.2	Raw Data Calibration Procedure . . . . .	34
4.2.1	Incidence Response . . . . .	35
4.2.2	Azimuth Response . . . . .	38
4.2.3	Data Analysis . . . . .	46
4.3	SIR Data Calibration Procedure . . . . .	52
4.3.1	Data Analysis . . . . .	52
4.4	Summary . . . . .	56
<b>5</b>	<b>Estimating the OSCAT Spatial Response Function Using Island Targets</b>	<b>59</b>
5.1	The Spatial Response Function . . . . .	60
5.2	Mathematical Formulation . . . . .	61
5.2.1	Least-squares . . . . .	62
5.2.2	Rank Reduced Least-squares . . . . .	64
5.2.3	Parameterization . . . . .	66
5.3	Geographic Sampling Region . . . . .	66
5.3.1	Island Targets . . . . .	67
5.3.2	Background $\sigma^\circ$ . . . . .	67
5.4	Simulation . . . . .	68
5.4.1	Simulation Procedure . . . . .	69
5.4.2	Simulation Results . . . . .	73
5.5	Spatial Response Function Estimates . . . . .	74
5.6	Summary . . . . .	83

<b>6</b>	<b>Conclusion</b>	<b>85</b>
6.1	Contributions . . . . .	85
6.1.1	Temporal Enhancement of OSCAT SIR Imagery . . . . .	86
6.1.2	Relative Cross-calibration Procedure . . . . .	86
6.1.3	Scatterometer Spatial Response Function Estimation . . . . .	87
6.2	Future Work . . . . .	87
6.2.1	Validation of Calibration Factors . . . . .	88
6.2.2	Diurnal Fluctuation in Greenland . . . . .	88
6.2.3	Spatial Response Function Estimation Method Improvement . . . . .	88
6.2.4	Further Validation of OSCAT Spatial Response Function Estimates . . . . .	88
6.2.5	Validation of Spatial Response Function Estimation Method . . . . .	89
6.2.6	Implementation of OSCAT Spatial Response Function Estimates . . . . .	89
	<b>Bibliography</b>	<b>90</b>
	<b>A Acronyms, Nomenclature, and Indicators</b>	<b>95</b>
	<b>B Relative Cross-calibration of 2009 Raw Data</b>	<b>99</b>
B.1	Incidence Resonse . . . . .	99
B.2	Azimuth Response . . . . .	102
B.3	Data Analysis . . . . .	109
B.4	Summary . . . . .	109
	<b>C Geolocation Error in OSCAT <math>\sigma^\circ</math> Measurements</b>	<b>115</b>
C.1	Longitudinal Bias . . . . .	115
C.2	Longitude Bias Correction Algorithm . . . . .	116
C.3	Summary . . . . .	119

<b>D Estimation of the OSCAT Antenna Azimuth Angle</b>	<b>123</b>
D.1 Estimation of the Antenna Azimuth Angle . . . . .	123
D.2 Summary . . . . .	125

## List of Tables

2.1	Comparative summary of major characteristics of QuikSCAT and OSCAT . . . . .	10
4.1	Relative calibration factors $\beta_h$ and $\beta_v$ in dB for $\sigma^\circ$ of OSCAT egg and slice measurements for ascending, descending, and combined passes. . . . .	46
4.2	Relative calibration factors $\beta_h$ and $\beta_v$ in dB for $\sigma^\circ$ of OSCAT egg and slice SIR image data for the Amazon and Greenland. . . . .	55
5.1	Approximate values of $\gamma$ computed for Peter I and Bear islands. . . . .	75
5.2	Calculated 3 dB beamwidths for OSCAT H-pol SRF estimates. . . . .	77
5.3	Calculated 3 dB beamwidths for OSCAT V-pol SRF estimates. . . . .	77
B.1	Relative calibration factors $\beta_h$ and $\beta_v$ for $\sigma^\circ$ of OSCAT egg and slice measurements for ascending, descending, and combined passes. . . . .	109
C.1	Horizontal distances $\Delta_x$ (km) between the island centroids of the SIR images and their actual geographical center locations. . . . .	122



## List of Figures

2.1	Specular scattering over (a) a smooth surface and diffuse scattering over (b) a rough surface. The $\sigma^\circ$ vs. incidence angle $\theta$ curve for (c) specular scattering drops off quickly, while for (d) diffuse scattering the curve drops off more slowly with a linear region of $\sigma^\circ$ . . . . .	7
2.2	(a) OSCAT and QuikSCAT orbital observation geometry. The dual pencil beam antenna spins about nadir as the spacecraft moves along its orbit. OSCAT is depicted in orange and QuikSCAT is depicted in green. (b) Conceptual diagram of the OSCAT 3 dB elliptical antenna footprint with iso-range lines. The shaded area illustrates a “slice” resolution area. . . . .	9
2.3	The frame by frame construction of a SIR image over the Antarctic for 6 passes. The SIR image is constructed by collocating and averaging together measurements from each pass of the satellite. The averaging can be seen in the overlap of the passes. The grayscale represents average time in minutes from the start of the day. . . . .	13
2.4	SIR images of $\sigma^\circ$ over Greenland for OSCAT V-pol (a) eggs and (b) slices corresponding to JD 242 of 2011. . . . .	13
3.1	The measurements that fall in the (a) Amazon and (b) Arctic study regions are used to create respective histograms of LTD in (c) and (d) for ascending and descending pass data. . . . .	17
3.2	Diagram illustrating the transition from ascending to descending pass in the Arctic. . . . .	18
3.3	The study regions (in red) used for measurement LTD extraction in the multi-scatterometer LTD analysis are outlined on $\mathcal{A}_v$ -SIR images for the (a) northern hemisphere and (b) southern hemisphere. . . . .	19
3.4	Scatterplots of LTD versus UTC for measurements taken from the Arctic study region of Figure 3.3a for OSCAT, Seawinds, and QuikSCAT. . . . .	20
3.5	Scatterplots of LTD versus UTC for measurements taken from the Antarctic study region of Figure 3.3b for OSCAT, Seawinds, and QuikSCAT. . . . .	21

3.6	Local time of day window boundaries defined for QuikSCAT, ASCAT, Sea-winds, and OSCAT. . . . .	22
3.7	OSCAT evening LTD $\mathcal{A}_v$ - and $\mathbf{p}$ -SIR images of the Arctic and Antarctic regions for JD 310-312 of 2009. . . . .	24
3.8	OSCAT midday and morning LTD $\mathcal{A}_v$ - and $\mathbf{p}$ -SIR images for JD 310-312 of 2009 for the Arctic and Antarctic, respectively. . . . .	25
3.9	OSCAT daily non-LTD $\mathcal{A}_v$ - and $\mathbf{p}$ -SIR images of the Arctic and Antarctic regions for JD 311 of 2009. . . . .	26
4.1	Images of mean QuikSCAT egg $\mathcal{A}_h$ - and $\mathcal{A}_v$ -SIR images corresponding to morning and evening passes over the Amazon for JD 181-205 of 2009. The color scale is in dB. . . . .	30
4.2	Images of standard deviation QuikSCAT egg $\mathcal{A}_h$ - and $\mathcal{A}_v$ -SIR images corresponding to morning and evening passes over the Amazon for JD 181-205 of 2009. . . . .	31
4.3	Images of the intermediate data selection masks generated for H-pol and V-pol $\sigma^\circ$ measurements corresponding to the morning and evening passes over the Amazon. White represents the data selection mask, gray represents land, and black represents ocean. The adjusted range of mean $\sigma^\circ$ used to generate a mask is specified in the square brackets in each image. . . . .	32
4.4	Image of the final data selection mask for the Amazon basin. The mask, shown in red, is superimposed on a QuikSCAT slice $\mathcal{A}_v$ -SIR image of the Amazon corresponding to JD 205-208 of 2009. The grayscale is in dB. . . . .	33
4.5	Image of the final data selection mask for the interior of Greenland. The mask, shown in red, is superimposed on a QuikSCAT slice $\mathcal{A}_v$ -SIR image of Greenland corresponding to JD 325 of 2009. The grayscale is in dB. . . . .	33
4.6	Scatterplots of egg $\sigma^\circ$ versus $\theta$ for combined pass data of OSCAT (a) H-pol and (b) V-pol, and QuikSCAT (c) H-pol and (d) V-pol. . . . .	35
4.7	Scatterplots of slice $\sigma^\circ$ versus $\theta$ for combined pass data of OSCAT (a) H-pol and (b) V-pol, and QuikSCAT (c) H-pol and (d) V-pol. . . . .	36
4.8	Scatterplots of slice $\sigma^\circ$ versus $\theta$ for ascending pass data of OSCAT (a) H-pol and (b) V-pol, and QuikSCAT (c) H-pol and (d) V-pol. . . . .	37
4.9	Scatterplots of slice $\sigma^\circ$ versus $\theta$ for descending pass data of OSCAT (a) H-pol and (b) V-pol, and QuikSCAT (c) H-pol and (d) V-pol. . . . .	37

4.10	Scatterplots of egg $\sigma^\circ$ versus $\phi$ for combined pass data of OSCAT (a) H-pol and (b) V-pol, and QuikSCAT (c) H-pol and (d) V-pol. . . . .	38
4.11	Scatterplots of $\theta$ normalized slice $\sigma^\circ$ versus $\phi$ for combined pass data of OSCAT (a) H-pol and (b) V-pol, and QuikSCAT (c) H-pol and (d) V-pol. . . . .	39
4.12	Scatterplots of $\phi$ normalized egg $\sigma^\circ$ versus $\phi$ for combined pass data of OSCAT (a) H-pol and (b) V-pol, and QuikSCAT (c) H-pol and (d) V-pol. . . . .	40
4.13	Scatterplots of $\theta$ and $\phi$ normalized slice $\sigma^\circ$ versus $\phi$ for combined pass data of OSCAT (a) H-pol and (b) V-pol, and QuikSCAT (c) H-pol and (d) V-pol. . . . .	41
4.14	Scatterplots of egg $\sigma^\circ$ versus $\phi$ for ascending pass data of OSCAT (a) H-pol and (b) V-pol, and QuikSCAT (c) H-pol and (d) V-pol. . . . .	42
4.15	Scatterplots of $\phi$ normalized egg $\sigma^\circ$ versus $\phi$ for ascending pass data of OSCAT (a) H-pol and (b) V-pol, and QuikSCAT (c) H-pol and (d) V-pol. . . . .	42
4.16	Scatterplots of egg $\sigma^\circ$ versus $\phi$ for descending pass data of OSCAT (a) H-pol and (b) V-pol, and QuikSCAT (c) H-pol and (d) V-pol. . . . .	43
4.17	Scatterplots of $\phi$ normalized egg $\sigma^\circ$ versus $\phi$ for descending pass data of OSCAT (a) H-pol and (b) V-pol, and QuikSCAT (c) H-pol and (d) V-pol. . . . .	43
4.18	Scatterplots of $\theta$ normalized slice $\sigma^\circ$ versus $\phi$ for ascending pass data of OSCAT (a) H-pol and (b) V-pol, and QuikSCAT (c) H-pol and (d) V-pol. . . . .	44
4.19	Scatterplots of $\theta$ and $\phi$ normalized slice $\sigma^\circ$ versus $\phi$ for ascending pass data of OSCAT (a) H-pol and (b) V-pol, and QuikSCAT (c) H-pol and (d) V-pol. . . . .	44
4.20	Scatterplots of $\theta$ normalized slice $\sigma^\circ$ versus $\phi$ for descending pass data of OSCAT (a) H-pol and (b) V-pol, and QuikSCAT (c) H-pol and (d) V-pol. . . . .	45
4.21	Scatterplots of $\theta$ and $\phi$ normalized slice $\sigma^\circ$ versus $\phi$ for descending pass data of OSCAT (a) H-pol and (b) V-pol, and QuikSCAT (c) H-pol and (d) V-pol. . . . .	45
4.22	Plots of measurement distribution $f_{\sigma^\circ}(\sigma^\circ)$ for normalized H- and V-pol egg measurements of the (a)-(b) ascending, (c)-(d) descending, and (e)-(f) combined passes. . . . .	47
4.23	Measurement distributions $f_{\sigma^\circ}(\sigma^\circ)$ for normalized H- and V-pol slice measurements of the (a)-(b) ascending, (c)-(d) descending, and (e)-(f) combined passes. . . . .	48
4.24	Mean values of normalized egg $\sigma^\circ$ from OSCAT and QuikSCAT versus local time of day. . . . .	49

4.25	Mean values of normalized egg $\sigma^\circ$ from SeaWinds and QuikSCAT versus local time of day. . . . .	49
4.26	Mean values of normalized egg $\sigma^\circ$ from OSCAT and QuikSCAT versus local time of day after adjustment of OSCAT data by the calibration factors. . . . .	50
4.27	Scatterplot of OSCAT and QuikSCAT normalized slice $\sigma^\circ$ versus $\theta$ for combined pass data of both beams. “x” marks the mean response of each beam. . . . .	51
4.28	Scatterplot of OSCAT and QuikSCAT normalized slice $\sigma^\circ$ versus $\theta$ for descending pass data of both beams. “x” marks the mean response of each beam. . . . .	51
4.29	Measurement distributions $f_{\sigma^\circ}(\sigma^\circ)$ for (a) H-pol and (b) V-pol egg SIR image $\sigma^\circ$ measurements for corresponding passes of each instrument over the Amazon region. . . . .	53
4.30	Measurement distributions $f_{\sigma^\circ}(\sigma^\circ)$ for (a) H-pol and (b) V-pol egg SIR image $\sigma^\circ$ measurements for the corresponding passes of each instrument over the Greenland region. . . . .	53
4.31	Measurement distributions $f_{\sigma^\circ}(\sigma^\circ)$ for (a) H-pol and (b) V-pol slice SIR image $\sigma^\circ$ measurements for corresponding passes of each instrument over the Amazon region. . . . .	54
4.32	Measurement distributions $f_{\sigma^\circ}(\sigma^\circ)$ for (a) H-pol and (b) V-pol slice SIR image $\sigma^\circ$ measurements for the corresponding passes of each instrument over the Greenland region. . . . .	54
4.33	Time series of $\mathcal{A}_h$ -SIR images of Greenland during the evening. The time series covers JD 2-13 of 2012. . . . .	57
5.1	Signal-only simulated measurements $z_s$ for eggs with island size corresponding to $\gamma = 0.75$ . . . . .	69
5.2	Singular value curves of $G_s(\gamma)$ for (a) egg and (b) slice simulations. . . . .	70
5.3	Images of (a) the egg $\mathbf{h}_s$ and (b)-(d) its estimates $\hat{\mathbf{h}}_s$ for $\gamma = 0.15$ , and (e) the slice $\mathbf{h}_s$ and (f)-(g) its estimates $\hat{\mathbf{h}}_s$ for $\gamma = 1.35$ . . . . .	71
5.4	Images of the normalized distribution of island $\sigma^\circ$ locations over the observation window for (a) $\gamma = 0.25$ with respect to the egg $\mathbf{h}_s$ , and (b) $\gamma = 0.15$ with respect to the slice $\mathbf{h}_s$ . . . . .	72
5.5	Images of $\hat{\mathbf{h}}_s$ corresponding to the optimum values of $\gamma$ and $L$ for (a) egg and (b) slice $\mathbf{h}_s$ . . . . .	72

5.6	Gridded images of the RMS reconstruction error $\delta$ for (a) eggs and (c) slices, and the absolute value of the difference $\epsilon$ of mean 3 dB beamwidths $B_3$ for (b) eggs and (d) slices. The grids represent $\delta$ and $\epsilon$ for $\gamma$ versus $L$ . A yellow contour line is shown on images of $\delta$ at values 25% greater than the respective minimum of each image. . . . .	73
5.7	A QuikSCAT slice $\mathcal{A}_h$ -SIR image of the Peter I Island for JD 180-210 of 2008. The image represents $\sigma^\circ$ in dB over the island using a Lambert equal-area projection with a pixel resolution of about 1.113 km per pixel. The red line traces out the elliptical approximation used for the island in estimation. . . . .	75
5.8	Singular value curve of $G$ constructed for the Peter I island using H-pol egg measurements. . . . .	76
5.9	Images of egg (a) H-pol $\hat{\mathbf{h}}_{\text{SVD}}$ , (b) H-pol $\hat{\mathbf{h}}_{\text{Par}}$ , (c) V-pol $\hat{\mathbf{h}}_{\text{SVD}}$ , and (d) V-pol $\hat{\mathbf{h}}_{\text{Par}}$ . . . . .	78
5.10	Images of $\hat{\mathbf{h}}_{\text{SVD}}$ for all H-pol slices computed over the Peter I Island using $L = 225$ . . . . .	79
5.11	Images of $\hat{\mathbf{h}}_{\text{SVD}}$ for all V-pol slices computed over the Peter I Island using $L = 225$ . . . . .	80
5.12	OSCAT egg $\mathcal{A}_h$ -SIR images of the Amazon basin for JD 25-26 of 2012 created using (a) the current simple approximation, (b) an improved approximation, and (c) the H-pol egg $\hat{\mathbf{h}}_{\text{Par}}$ . . . . .	81
5.13	Images of (a) the simple approximation, (b) the improved approximation, and (c) the parameterized estimate $\hat{\mathbf{h}}_{\text{Par}}$ of H-pol egg SRF used in creating the $\mathcal{A}_h$ -SIR images of the Amazon basin for JD 25-26 of 2012. . . . .	81
5.14	OSCAT egg $\mathcal{A}_v$ -SIR images of the Amazon basin for JD 25-26 of 2012 created using (a) the current simple approximation, (b) an improved approximation, and (c) the V-pol egg $\hat{\mathbf{h}}_{\text{Par}}$ . . . . .	82
5.15	Images of (a) the simple approximation, (b) the improved approximation, and (c) the parameterized estimate $\hat{\mathbf{h}}_{\text{Par}}$ of V-pol egg SRF used in creating the $\mathcal{A}_v$ -SIR images of the Amazon basin for JD 25-26 of 2012. . . . .	82
5.16	A QuikSCAT egg (a) $\mathcal{A}_h$ -SIR image and (b) $\mathcal{A}_v$ -SIR image of the Amazon basin for JD 25-28 of 2009. . . . .	83
B.1	Scatterplots of egg $\sigma^\circ$ versus $\theta$ for ascending and combined pass data of OSCAT (a) H-pol and (b) V-pol, and QuikSCAT (c) H-pol and (d) V-pol. . . . .	100

B.2	Scatterplots of slice $\sigma^\circ$ versus $\theta$ for ascending and combined pass data of OSCAT (a) H-pol and (b) V-pol, and QuikSCAT (c) H-pol and (d) V-pol. . . . .	100
B.3	Scatterplots of slice $\sigma^\circ$ versus $\theta$ for ascending pass data of OSCAT (a) H-pol and (b) V-pol, and QuikSCAT (c) H-pol and (d) V-pol. . . . .	101
B.4	Scatterplots of slice $\sigma^\circ$ versus $\theta$ for descending pass data of OSCAT (a) H-pol and (b) V-pol, and QuikSCAT (c) H-pol and (d) V-pol. . . . .	101
B.5	Scatterplots of egg $\sigma^\circ$ versus $\phi$ for combined pass data of OSCAT (a) H-pol and (b) V-pol, and QuikSCAT (c) H-pol and (d) V-pol. . . . .	103
B.6	Scatterplots of $\theta$ normalized slice $\sigma^\circ$ versus $\phi$ for combined pass data of OSCAT (a) H-pol and (b) V-pol, and QuikSCAT (c) H-pol and (d) V-pol. . . . .	103
B.7	Scatterplots of $\phi$ normalized egg $\sigma^\circ$ versus $\phi$ for combined pass data of OSCAT (a) H-pol and (b) V-pol, and QuikSCAT (c) H-pol and (d) V-pol. . . . .	104
B.8	Scatterplots of $\theta$ and $\phi$ normalized slice $\sigma^\circ$ versus $\phi$ for combined pass data of OSCAT (a) H-pol and (b) V-pol, and QuikSCAT (c) H-pol and (d) V-pol. . . . .	104
B.9	Scatterplots of egg $\sigma^\circ$ versus $\phi$ for ascending pass data of OSCAT (a) H-pol and (b) V-pol, and QuikSCAT (c) H-pol and (d) V-pol. . . . .	105
B.10	Scatterplots of $\phi$ normalized egg $\sigma^\circ$ versus $\phi$ for ascending pass data of OSCAT (a) H-pol and (b) V-pol, and QuikSCAT (c) H-pol and (d) V-pol. . . . .	105
B.11	Scatterplots of egg $\sigma^\circ$ versus $\phi$ for descending pass data of OSCAT (a) H-pol and (b) V-pol, and QuikSCAT (c) H-pol and (d) V-pol. . . . .	106
B.12	Scatterplots of $\phi$ normalized egg $\sigma^\circ$ versus $\phi$ for descending pass data of OSCAT (a) H-pol and (b) V-pol, and QuikSCAT (c) H-pol and (d) V-pol. . . . .	106
B.13	Scatterplots of $\theta$ normalized slice $\sigma^\circ$ versus $\phi$ for ascending pass data of OSCAT (a) H-pol and (b) V-pol, and QuikSCAT (c) H-pol and (d) V-pol. . . . .	107
B.14	Scatterplots of $\theta$ and $\phi$ normalized slice $\sigma^\circ$ versus $\phi$ for ascending pass data of OSCAT (a) H-pol and (b) V-pol, and QuikSCAT (c) H-pol and (d) V-pol. . . . .	107
B.15	Scatterplots of $\theta$ normalized slice $\sigma^\circ$ versus $\phi$ for descending pass data of OSCAT (a) H-pol and (b) V-pol, and QuikSCAT (c) H-pol and (d) V-pol. . . . .	108
B.16	Scatterplots of $\theta$ and $\phi$ normalized slice $\sigma^\circ$ versus $\phi$ for descending pass data of OSCAT (a) H-pol and (b) V-pol, and QuikSCAT (c) H-pol and (d) V-pol. . . . .	108

B.17	Plots of measurement distribution $f_{\sigma^\circ}(\sigma^\circ)$ for normalized H- and V-pol egg measurements of the (a)-(b) ascending, (c)-(d) descending, and (e)-(f) combined passes. . . . .	110
B.18	Measurement distributions $f_{\sigma^\circ}(\sigma^\circ)$ for normalized H- and V-pol slice measurements of the (a)-(b) ascending, (c)-(d) descending, and (e)-(f) combined passes. . . . .	111
B.19	Mean values of normalized egg $\sigma^\circ$ from OSCAT and QuikSCAT versus local time of day. . . . .	112
B.20	Mean values of normalized egg $\sigma^\circ$ from OSCAT and QuikSCAT versus local time of day after adjustment of OSCAT data by the calibration factors. . . .	112
B.21	Scatterplot of OSCAT and QuikSCAT normalized slice $\sigma^\circ$ versus $\theta$ for combined pass data of both beams. “x” marks the mean response of each beam. . . . .	113
B.22	Scatterplot of OSCAT and QuikSCAT normalized slice $\sigma^\circ$ versus $\theta$ for descending pass data of both beams. “x” marks the mean response of each beam. . . . .	113
C.1	Ascending and descending, slice (a)-(b) $\mathcal{A}_h$ -SIR images and (c)-(d) $\mathcal{A}_v$ -SIR images of the Bear island for JD 073-082 of 2011. . . . .	116
C.2	Ascending and descending, slice (a)-(b) $\mathcal{A}_h$ -SIR images and (c)-(d) $\mathcal{A}_v$ -SIR images of the Peter I island for JD 073-082 of 2011. . . . .	117
C.3	Ascending and descending, slice (a)-(b) $\mathcal{A}_h$ -SIR images and (c)-(d) $\mathcal{A}_v$ -SIR images of the Niue island for JD 073-082 of 2011. . . . .	118
C.4	Ascending and descending, slice (a)-(b) $\mathcal{A}_h$ -SIR images and (c)-(d) $\mathcal{A}_v$ -SIR images of the Bear island for JD 073-082 of 2011. . . . .	119
C.5	Ascending and descending, slice (a)-(b) $\mathcal{A}_h$ -SIR images and (c)-(d) $\mathcal{A}_v$ -SIR images of the Peter I island for JD 073-082 of 2011. . . . .	120
C.6	Ascending and descending, slice (a)-(b) $\mathcal{A}_h$ -SIR images and (c)-(d) $\mathcal{A}_v$ -SIR images of the Niue island for JD 073-082 of 2011. . . . .	121
D.1	A diagram of the along track and cross track geometry with the antenna azimuth angle and antenna azimuth exclude angles. . . . .	124
D.2	A diagram of the along track and cross track geometry with the antenna azimuth angle and antenna azimuth exclude angles. . . . .	124



# Chapter 1

## Introduction

Space-borne scatterometers are active radar devices that are invaluable in Earth remote sensing applications. Normalized radar backscatter ( $\sigma^\circ$ ) measurements provided by scatterometers are used in weather forecasting, scientific studies of global climatological and geophysical phenomena, and monitoring of large scale human interaction on the planet. Though originally intended for estimation of wind speed and direction over the ocean, scatterometers have since been utilized to estimate soil moisture [1–3], detect polar sea ice extent [4–8], track icebergs [9], monitor global vegetation [10–14], map deep sea oil spills [15], and other applications [16, 17].

The first (referred to as QuikSCAT) of two SeaWinds Ku-band scatterometers was launched onboard the QuikSCAT satellite on June 19, 1999 as a “quick” recovery to the NASA scatterometer (NSCAT) mission, which prematurely ended after only 9 months in June 1997 due to a power failure. Three years later in December of 2002, the second (referred to as SeaWinds) SeaWinds scatterometer was launched onboard the Japanese Advanced Earth Observation Satellite 2 (ADEOS-II) to begin the tandem SeaWinds scatterometer mission with QuikSCAT. However, a power system failure on ADEOS-II brought an early end to the mission on October 24, 2003. QuikSCAT, on the other hand, continued relentlessly for 5 years past its mission expiration date until a bearing froze in the antenna rotation mechanism prohibiting normal operation and finally bringing an end to the mission on November 23, 2009.

Collecting over a decade’s worth of unprecedentedly accurate Ku-band  $\sigma^\circ$  observations with high daily spatial coverage of the Earth’s surface [16], QuikSCAT made a lasting impact on the remote sensing community. QuikSCAT opened the door to many scientific studies, better detection in tropical storm nowcasting, more accurate numerical weather

prediction, and algorithms used in creating a Ku-band climate product dataset. Upon failure of QuikSCAT, it was predicted that the marine nowcasting community and ocean wave community would see an 80 to 90% decrease in detected hurricane force from extratropical cyclones, and reduce the impact of scatterometer data on forecasting skill in numerical weather prediction centers [17]. After the QuikSCAT mission came to end, so did the extensive climate product dataset that began with it. For the NASA Scatterometer Climate Record Pathfinder (SCP) and its derivatives, this includes high-resolution Ku-band  $\sigma^\circ$  imagery, maps of the polar sea ice extent, a Ku-band Antarctic iceberg location database, and other derived products [18]. To fill the void in the SCP left by QuikSCAT's absence, there is a need for a suitable replacement.

Fortunately, on September 23, 2009, the Indian Space Research Organisation (ISRO) launched the Oceansat-2 satellite into orbit with a pencil-beam Ku-band scatterometer (OSCAT). The satellite orbits about the Earth's poles in a sun-synchronous orientation. The design and orbit geometry of OSCAT make it an excellent candidate for continuing the SCP dataset of QuikSCAT. To minimize inconsistencies in the climate product dataset due to instrument change, instrument cross-calibration is necessary.

Many of the SCP products require knowledge of the spatial response function (SRF) to enhance the utility of scatterometer data, such as ultra-high resolution wind retrieval (UHR Winds) [19], scatterometer image reconstruction (SIR) [20], and more [21–23]. Thus, continuing the SCP data time series through OSCAT requires knowledge of the OSCAT SRF as well as cross-calibration with QuikSCAT. For QuikSCAT, creation of SCP products was simplified by computing and tabulating its SRF [24]. However, having only limited details of signal processing performed onboard OSCAT, computation of its SRF is impossible. Therefore, must estimate it for use in the creation of climate products.

## 1.1 Thesis Statement

The purpose of this thesis is to help ensure a seamless transition from QuikSCAT to OSCAT in the SCP dataset through relative cross-calibration of the two instruments and estimation of the OSCAT spatial response function. Based on previous methods of post-launch calibration using extended-area natural land targets [25–28], a modified approach

is presented in which raw  $\sigma^\circ$  measurements are normalized by estimates of the azimuthal and incidence modulation. The normalized measurements of both instruments are obtained and the mean and standard deviation of the measurements are compared to get a relative calibration factor. Because the Amazon is widely accepted as a calibration site [25–29], the procedure is performed over an extended-area of the Amazon. Ideally, by application of the relative calibration factor to raw  $\sigma^\circ$  measurements, the OSCAT  $\sigma^\circ$  signature will be consistent with that of QuikSCAT and can be used to create SCP image products, such as SIR images, that maintain consistency amongst conically scanning pencil-beam scatterometer datasets in the SCP. This will help minimize variability in SCP products due to instrument biases and provide a consistent extended Ku-band climate record for use in scientific studies.

However, to simplify creation of SCP products, a relative calibration factor that can be applied directly to SCP products is desired so that they can be made without adjusting raw measurements prior. This is done for SIR  $\sigma^\circ$  images in this thesis. Following a similar procedure for raw measurements, the mean and variance of  $\sigma^\circ$  values of SIR images are compared to obtain a relative calibration factor applicable to OSCAT SIR imagery. The interior regions of Greenland are considered in addition to the Amazon as calibration sites due to their seasonal stability and minimal azimuthal dependence. To minimize biases in relative calibration factors that can occur as a result of diurnal variability in  $\sigma^\circ$  measurements [11, 26, 30], methods for improving temporal sampling based on local time of day [31] are analyzed for OSCAT and applied to SIR images.

To create the climate products necessitating knowledge of the SRF, a method of estimating the OSCAT SRF using natural land targets is presented. The method entails inverting the scatterometer measurement model of OSCAT using  $\sigma^\circ$  measurements over an island target to solve for an estimate of the SRF. By introducing a simplified model of the scattering characteristics of island targets, the solution is reduced to rank-reduced least-squares estimation approach. A simulation is performed to validate the efficacy of the estimation procedure and optimize for related parameters.

## 1.2 Thesis Organization

The organization of this thesis is as follows. Chapter 2 provides background on basic scatterometry principles, design characteristics of OSCAT and QuikSCAT, the SIR algorithm, and post-launch calibration methods for spaceborne scatterometers. Chapter 3 discusses local time of day processing for OSCAT and compares it to that of QuikSCAT and SeaWinds. Chapter 4 explains the relative cross-calibration of OSCAT and QuikSCAT. It describes and presents the results of the modified relative cross-calibration approach using extended-area natural land targets for both raw measurements and SIR imagery. Chapter 5 discusses the SRF estimation method for OSCAT, including details on the simulation and results for real data. Chapter 6 concludes, giving a summary of contributions made and providing direction for further research. Appendix A contains results of applying the relative cross-calibration procedure of Chapter 4 to early versions of raw OSCAT data. Appendix B discusses an apparent longitudinal bias in the reported center locations of  $\sigma^\circ$  measurements and provides a simple correction algorithm. Finally, Appendix C demonstrates the algorithm used for derivation of the OSCAT antenna azimuth angle for SIR processing.

## Chapter 2

### Background

Starting from the fundamentals of scatterometry, this chapter explains pertinent background information crucial to understanding the work described in this thesis. After an overview of scatterometer fundamentals, an introduction to post-launch scatterometer calibration approaches using extended-area natural land targets is given. Next, the characteristics of both the QuikSCAT and OSCAT instruments are compared and contrasted. The scatterometer climate pathfinder record is discussed along with the scatterometer image reconstruction (SIR) algorithm, and then the chapter concludes with a brief description of the data used in this thesis.

#### 2.1 Scatterometer Fundamentals

As an active radar device, the main function of a scatterometer is to transmit a pulse of electromagnetic energy to a target and then precisely measure the amount of power scattered back. The backscattered power  $P_b$  from a target is given by the mono-static form of the radar equation

$$P_b = \frac{P_t \lambda^2 Q^2 \sigma}{(4\pi)^3 r^4}, \quad (2.1)$$

where  $P_t$  is the transmitted power,  $Q$  is the gain of the antenna,  $\lambda$  is the signal wavelength,  $r$  is the range from the transmitter/receiver to the target, and  $\sigma$  is the radar cross-section of the target. Due to noise caused by instrument electronics and atmospheric effects, the actual power received  $P_r$  by the radar is  $P_b$  plus noise power  $P_n$ .

The radar cross-section  $\sigma$  is essentially a measure of the effective size of a point target, and is useful in target detection based radar applications. However, for distributed targets, such as the surface of the Earth, it is more useful to know the scattering characteristics of the surface illuminated by the antenna. Thus, in scatterometry,  $\sigma$  is normalized to the area

$A$  of Earth’s surface illuminated by the antenna to give the normalized radar cross-section  $\sigma^\circ = \sigma/A$ , also referred to as the normalized radar backscatter. The scatterometer obtains measured values of  $\sigma^\circ$  from

$$\sigma^\circ = \frac{(4\pi)^3 P_b r^4}{P_t \lambda^2 Q^2 A}, \quad (2.2)$$

where  $P_b$  is calculated by subtracting a measurement of  $P_n$  from  $P_r$ , and other parameters are determined at the time of measurement or are known prior to the measurement.

The quantity  $\sigma^\circ$  is effectively a measure of how well the illuminated surface of the Earth reflects the incident pulse of electromagnetic energy back to the scatterometer. Measurements of  $\sigma^\circ$  are affected by the physical properties of the illuminated surface of the Earth, such as dielectric constant, shape, roughness, and orientation relative to the scatterometer. Measurements of  $\sigma^\circ$  can vary with time, transmit frequency, polarization of the electromagnetic wave, and azimuth  $\phi$  and incidence  $\theta$  angles of the incident electromagnetic wave. The relationship between  $\sigma^\circ$  and  $\theta$  is largely affected by the roughness of the surface illuminated by the antenna. Specular scattering over smooth surface causes  $\sigma^\circ$  to drop off rapidly with  $\theta$ , while diffuse scattering over rough surfaces results in a slower rate of change in  $\sigma^\circ$  with  $\theta$ , as illustrated in Figure 2.1.

### 2.1.1 Post-launch Scatterometer Calibration

Because pre-launch calibration alone is often insufficient for attaining proper levels of precision in  $\sigma^\circ$  measurements, post-launch calibration techniques were developed to ensure expected accuracy and consistency between instruments. There are two key approaches for post-launch calibration: 1) ground stations [29, 32] and 2) homogeneous extended-area natural land targets [25–29, 33]. The latter approach is not only more cost effective, but also lends itself better to relative cross-calibration efforts between instruments because it can be done remotely.

Past locations chosen for post-launch calibration using homogeneous extended-area natural land targets include the Congo [25, 28], the Sahara [27], and central Russia [29]. Traditionally, however, the site most frequently chosen is the Amazon [25–29, 33]. This is because random orientation of individual scatterers in the uniform and dense canopy of the

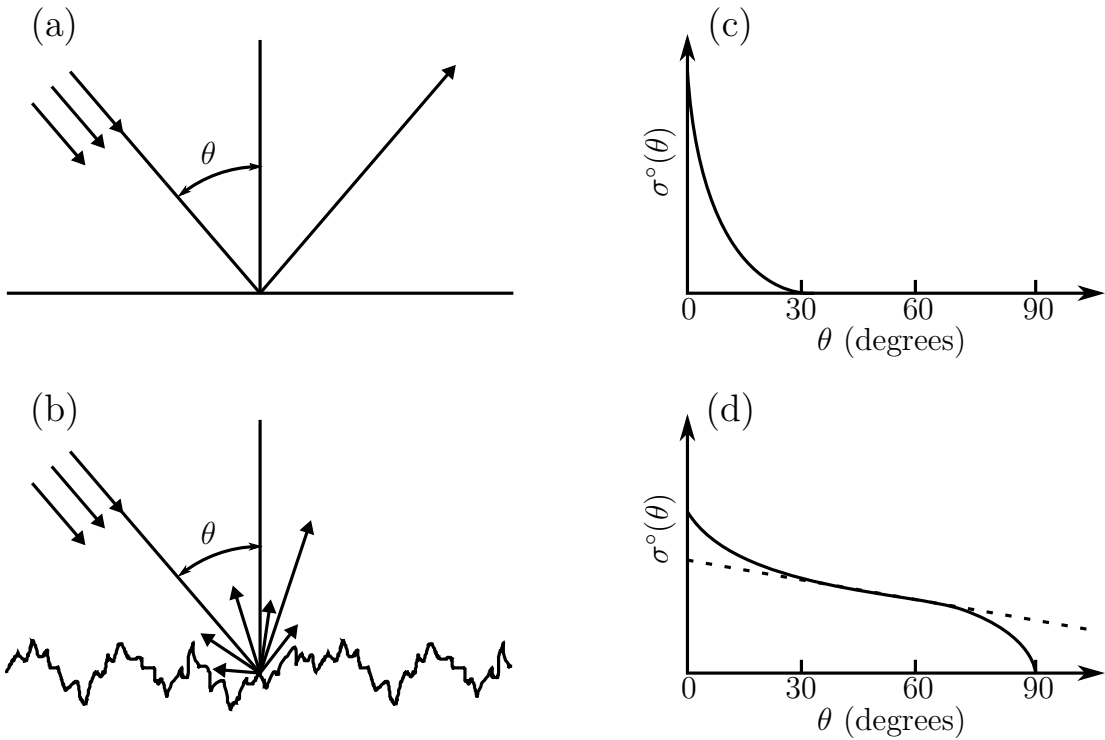


**Figure 2.1:** Specular scattering over (a) a smooth surface and diffuse scattering over (b) a rough surface. The  $\sigma^o$  vs. incidence angle  $\theta$  curve for (c) specular scattering drops off quickly, while for (d) diffuse scattering the curve drops off more slowly with a linear region of  $\sigma^o$ .

Amazon make  $\sigma^o$  essentially insensitive to polarization and independent of azimuth angle, while its equatorial location minimizes seasonal variability [29], limiting dependence of  $\sigma^o$  to incidence angle over the region. By using a simplified linear model for the relationship between incidence angle and  $\sigma^o$ , the incidence angle dependence of  $\sigma^o$  can be adjusted for and statistics of measured  $\sigma^o$  can be compared between different antennas of the same instrument or other instruments free of dependency biases. The linear model for incidence angle dependence of  $\sigma^o$  is given by

$$\sigma^o(\theta) = \mathcal{A} + \mathcal{B}(\theta - \Theta), \quad (2.3)$$

where  $\mathcal{A}$  is the corrected backscatter value,  $\mathcal{B}$  is the linear dependence of  $\sigma^o$  on incidence angle, and  $\Theta$  is the nominal incidence angle about which  $\sigma^o$  is linearized [27, 30, 34]. This

model is particularly useful over natural land targets, where diffuse scattering increases the range of incidence angles over which  $\sigma^\circ$  appears linear as illustrated in Figure 2.1d.

For traditional fan beam scatterometers that observe  $\sigma^\circ$  at multiple incidence angles and few azimuth angles, this approach allows for a simple beam balance technique in which  $\sigma^\circ$  for each antenna beam is forced to the mean response of all beams relative to  $\Theta = 40^\circ$  [33]. For conically scanning pencil-beam scatterometers that measure  $\sigma^\circ$  over the entire range of azimuth angles and exactly two incidence angles ( $46^\circ$  and  $54^\circ$  for QuikSCAT), this beam balancing approach is not applicable because of the incidence angle difference between the beams and lack of a suitable reference. Thus, for QuikSCAT, an alternative beam balance approach for the range cell data based on the  $\sigma^\circ$  azimuth response and only a small incidence angle correction is applied [33]. The launch of SeaWinds provided a suitable reference for QuikSCAT, and the relative cross-calibration of the instruments is analyzed based on the  $\sigma^\circ$  incidence response of each instrument [27].

## 2.2 Instrument Description

OSCAT and QuikSCAT are both dual-pencil beam scatterometers employing a 1 m dish antenna which transmits and receives a horizontally polarized inner beam and vertically polarized outer beam at 13.5 GHz for OSCAT and 13.4 GHz for QuikSCAT. Their inner and outer beams are at incidence angles of  $49^\circ$  and  $57^\circ$  respectively for OSCAT, and  $46^\circ$  and  $49^\circ$  respectively for QuikSCAT. The inner and outer beams are transmitted alternately at a pulse repetition frequency (PRF) of 96.5 Hz per beam for OSCAT and 92.5 Hz per beam for QuikSCAT. They each rotate about the Earth in a sun-synchronous polar orbit while tracing out a helix on the earth by conically scanning their antenna about the nadir vector. OSCAT has 2-day exact-repeat orbit and an antenna scan rate of 20.5 rpm that is synchronous with the PRF [35], while QuikSCAT has a 4-day near-repeat orbit and an antenna scan rate of 18 rpm that is asynchronous with the PRF. The instrument altitude at the equator is 720 km for OSCAT and 803 km for QuikSCAT, and the swath traced out by their inner and outer beams are approximately 1400 km and 1836 km respectively for OSCAT, and 1400 km and 1800 km respectively for QuikSCAT. Figure 2.2a illustrates the relative measurement geometry of OSCAT and QuikSCAT.

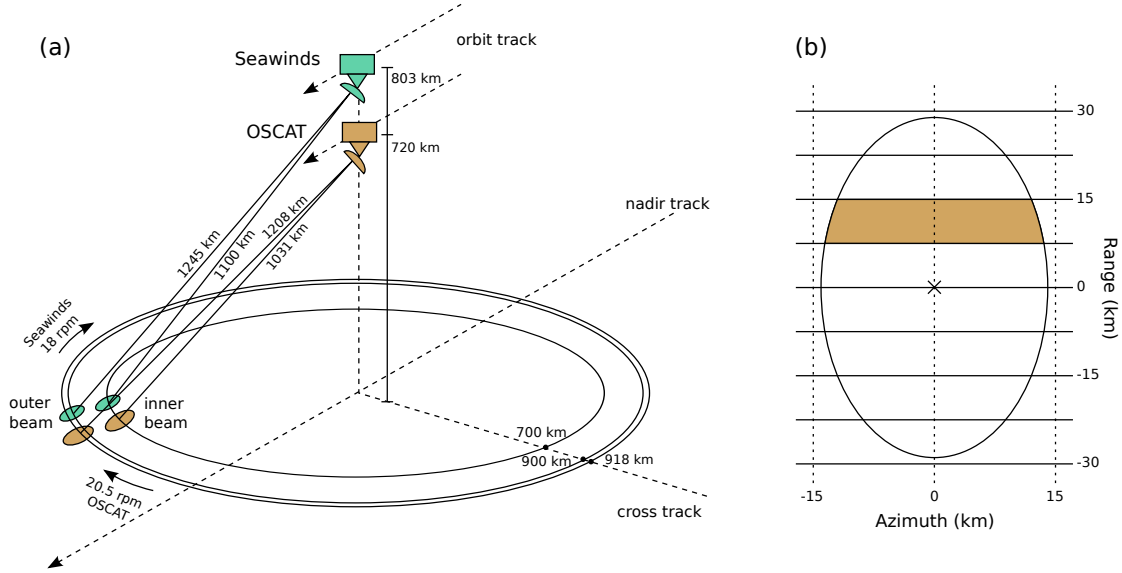


**Figure 2.2:** (a) OSCAT and QuikSCAT orbital observation geometry. The dual pencil beam antenna spins about nadir as the spacecraft moves along its orbit. OSCAT is depicted in orange and QuikSCAT is depicted in green. (b) Conceptual diagram of the OSCAT 3 dB elliptical antenna footprint with iso-range lines. The shaded area illustrates a “slice” resolution area.

Both scatterometers transmit and receive using a linear frequency modulated (LFM) chirp. The radar echo from the surface undergoes signal processing to compute an estimate of the  $\sigma^\circ$  of the surface illuminated by the antenna. The 3 dB footprint illuminated by the antenna for the inner and outer beam is elliptically shaped with dimensions of approximately 26.8 x 45.1 km and 29.7 x 68.5 km respectively for OSCAT and 24.0 x 31.0 km and 26.0 x 36.0 km respectively for QuikSCAT. Measurements computed from the antenna footprint are termed “eggs”. In addition, range compression is performed onboard to separate the return echo into multiple range bins, as depicted in Figure 2.2. Measurements of  $\sigma^\circ$  corresponding to individual range bins are termed “slices”. There are a total of 7 slices reported for an inner beam echo and 12 slices reported for an outer beam echo of OSCAT [35]. For QuikSCAT there are 8 slices reported for each beam echo [24]. There is a corresponding spatial response function (SRF) associated with each individual egg and slice.

The return echo experiences a Doppler shift caused by motion and attitude of the spacecraft, azimuth position of the antenna, and rotation of the Earth. Doppler shift induced by azimuth position of the antenna is corrected for onboard, while Earth rotation and space-

**Table 2.1:** Comparative summary of major characteristics of QuikSCAT and OSCAT [35]

Parameter	QuikSCAT		OSCAT	
Antenna Type	1 m dual-feed parabolic		1 m dual-feed parabolic	
Orbital Period	101 min (14.25 orbits/day)		99.31 min (14.5 orbits/day)	
Asc Node Time	6:00 a.m. $\pm$ 30 min		12:00 midnight $\pm$ 30 min	
Satellite Altitude	803 km at equator		720 km at equator	
Frequency	13.402 GHz		13.515 GHz	
Wavelength	0.0224 m		0.0221 m	
Scan Rate	18 rpm		20.5 rpm	
PRF (per beam)	92.5 Hz		96.5 Hz	
Start Date	June 19, 1999		Sept. 23, 2009	
End Date	Nov. 23, 2009		—	
	Inner Beam	Outer Beam	Inner Beam	Outer Beam
Polarization	HH	VV	HH	VV
Reported Slices	8	8	7	12
Incidence Angle	46°	54°	49°	57°
Slant Range	1100 km	1245 km	1031 km	1208 km
Swath Width	1400 km	1800 km	1400 km	1836 km
Beamwidth (Az x El)	1.6° x 1.8°	1.4° x 1.7°	1.47° x 1.62°	1.39° x 1.72°
Footprint (km) (Az x El)	24.0 x 31.0	26.0 x 36.0	26.8 x 45.1	29.7 x 68.5

craft attitude induced Doppler shift is compensated for by providing sufficient bandwidth for the return echo [35]. Across each slice, differential Doppler shift can cause the shape and orientation of the SRF to vary. However, this does not affect an egg SRF, and its effects on a slice SRF is assumed negligible when performing SRF estimation in Chapter 4. The common characteristics of OSCAT and QuikSCAT are summarized in Table 2.1 for comparison.

The orientation of the Oceansat-2 orbit and synchronicity of antenna rotation with PRF means that a given spot on the Earth’s surface is observed by finite azimuthal and incidence geometries. As a consequence, regions of the Earth covered by only few passes of the scatterometer, such as low latitude locations, exhibit very limited azimuth and incidence angle diversity. Synchronizing the PRF with antenna scan rate decreases azimuthal and incidence geometries by limiting azimuth angle looks per satellite revolution and scan frame. For SRF estimation, this can be an inhibiting characteristic that results in directional biases in estimates of the SRF. When performing SRF estimation as outlined in this paper, care

should be taken to choose geographic sampling regions with high diversity of azimuthal and incidence geometries.

### **2.2.1 Data Description**

L1B data of OSCAT and QuikSCAT are used in the creation of all SIR imagery used within this thesis. Also, L1B data is used as raw measurements in the procedures and analyses of this thesis. The most recent version of QuikSCAT L1B data spans the entire length of the QuikSCAT mission and is used for QuikSCAT. For OSCAT there are currently three versions of L1B data. The first version spans from Julian Day (JD) 309 of 2009 to JD 120 of 2010. The second version spans from JD 73 to 354 of 2011 and was internally calibrated by ISRO. The most recent version of OSCAT L1B data is available from Julian Day (JD) 355 of 2011 to the present and is another internal calibration by ISRO with a major change to the data format, including access to more geometry measurements than previous formats. ISRO is expected to retroactively apply the processing algorithms from the most recent version to the entire mission dataset, which will hopefully result in availability of the full mission data. However, the procedures and analyses of this thesis are performed with the L1B data available at the time.

### **2.3 Scatterometer Climate Record Pathfinder**

The NASA Scatterometer Climate Record Pathfinder [36] is a project sponsored by NASA with a goal of supporting climate studies of the Earth's cryosphere and biosphere through the development of a scatterometer-based data time series. The data time series contains scatterometer-based datasets that are useful to climate studies because the microwave radar signal of scatterometers can penetrate the surface of the Earth and observe subsurface climate related features. Using the Seasat scatterometer (SASS) as a baseline for measuring global change, other missions have been adopted to the SCP to provide updated coverage of the planet. These missions include the C-band European Space Agency (ESA) Earth Remote Sensing (ERS) -1 and -2 (1999-2000), the NASA Scatterometer (NSCAT) (1996-97), QuikSCAT (1999-2009), SeaWinds (2003), the ESA Advanced Scatterometer (ASCAT)

(2009+), and the Indian Space Research Organisation (ISRO) Oceansat-2 Scatterometer (OSCAT) (2009+) [37].

The SCP datasets are based on a time series of enhanced resolution  $\sigma^\circ$  images created using the SIR algorithm. For the traditional fan-beam scatterometers (SASS, NSCAT, ERS, and ASCAT)  $\mathcal{A}$ - and  $\mathcal{B}$ -SIR images are made from  $\sigma^\circ$ , where  $\mathcal{A}$  and  $\mathcal{B}$  are with reference to Eq. 2.3 and  $\Theta = 40^\circ$ . In other words,  $\mathcal{A}$ -SIR images for fan-beam scatterometers are SIR images of  $\sigma^\circ$  normalized to  $40^\circ$  incidence angle in dB, and  $\mathcal{B}$ -SIR images are SIR images of the slope of  $\sigma^\circ$  vs. incidence angle in dB/degree. For SeaWinds and QuikSCAT  $\mathcal{A}_h$ - and  $\mathcal{A}_v$ -SIR images are made from  $\sigma^\circ$  at the observation incidence angles of the horizontally polarized inner beam and vertically polarized outer beam, respectively. In addition to SIR images, a number of derived products are also provided, including sea ice extent maps, sea ice motion datasets, current Antarctic iceberg locations, the Antarctic iceberg location database, animated visualizations of  $\sigma^\circ$ , ultra-high resolution winds (UHR Winds), and tropical cyclone wind observation databases [37]. To maintain consistency amongst conically scanning pencil-beam scatterometers as has been done for fan-beam scatterometers by linearizing  $\sigma^\circ$  about  $40^\circ$  incidence angle, a  $\sigma^\circ$  normalization scheme based on the incidence angle is needed. Therefore, the  $\sigma^\circ$  of future conically scanning pencil-beam scatterometers added to the SCP can be normalized to the observation incidence angles of SeaWinds and QuikSCAT.

### 2.3.1 Scatterometer Image Reconstruction (SIR)

Scatterometer image reconstruction (SIR) is a type of enhanced resolution imaging (ERI) used to enhance the utility of scatterometer data for land and ice studies. The SIR algorithm is based on a multivariate form of block multiplicative algebraic reconstruction. It is used as a part of the SCP to create high-resolution imagery of scatterometer measurements. It does this by combining overlapping measurements for multiple scatterometer passes over the same region to solve for the true surface image of the region. To solve for the true surface image it effectively inverts the effects of irregular sample spacing and aperture filtering. For a single pixel this is done by computing the weighted average of measurements for which a portion of their aperture function (or spatial response function) overlaps that pixel. The weighting is the value of the aperture function over that pixel. This results in enhanced



**Figure 2.3:** The frame by frame construction of a SIR image over the Antarctic for 6 passes. The SIR image is constructed by collocating and averaging together measurements from each pass of the satellite. The averaging can be seen in the overlap of the passes. The grayscale represents average time in minutes from the start of the day.

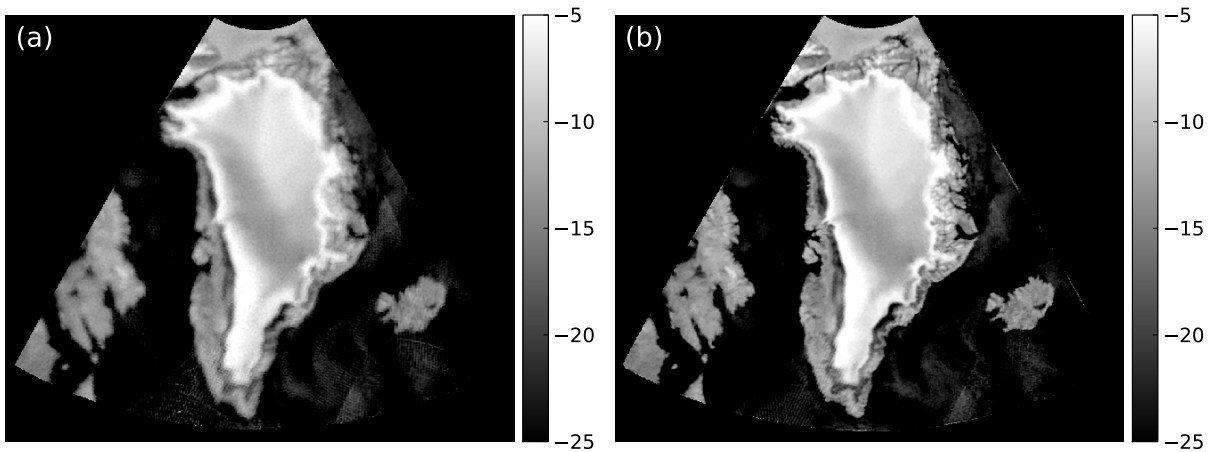


**Figure 2.4:** SIR images of  $\sigma^\circ$  over Greenland for OSCAT V-pol (a) eggs and (b) slices corresponding to JD 242 of 2011.

image resolution by recovering high frequency information suppressed by the aperture function [38]. The frame by frame construction of a SIR image of measurement observation times is demonstrated in Figure 2.3 as an example.

Daily SIR images are made for QuikSCAT and OSCAT using both egg and slice measurements for each beam. SIR images made using egg measurements have a grid spacing of approximately 4.45 km/pix and have an effective resolution of 9 km. SIR images made using slice measurements have a grid spacing of approximately 2.225 km/pix and have an effective resolution between 3-6 km. An example of an OSCAT egg and slice  $\sigma^\circ$  SIR image of Greenland corresponding to JD 10 of 2012 can be seen in Figure 2.4.



## Chapter 3

### Local Time of Day Processing with OSCAT

The wide swath and sun-synchronous polar orbit of OSCAT enables both high temporal and spatial sampling of normalized radar backscatter  $\sigma^\circ$  over the earth's entire surface. Surrounding the poles, the sampling is particularly dense because of overlapping passes. This dense sampling is useful in supporting image reconstruction algorithms such as SIR, in which collocated measurements from multiple passes are averaged together to create a regional image of the earth. An undesirable feature that can occur as a result of averaging measurements close to the poles, as done in SIR processing, is poor temporal resolution with respect to local time at the observed location.

The local time at the observed location is referred to as the local time of day (LTD). The time referenced by the satellite for observations is Coordinated Universal Time (UTC), which is the time associated with  $0^\circ$  longitude. For a location at  $180^\circ$  longitude, the LTD is 12 hours backwards or forwards in relation to UTC. Thus, a 24 hour UTC observation period can result in observations over the polar regions that may vary in LTD by up to 48 hours. Such behavior can result in complications in tracking diurnal phenomena such as sea ice extent, icebergs, melting patterns in ice over sea or land, etc.

One approach to ameliorate poor temporal resolution is to separate the data based on ascending and descending passes of the satellite. This method yields satisfactory results for locations close to the equator, where observation LTD is fixed by the ascending and descending nodes of the satellite. For locations near the pole, however, swath overlap and day boundary effects render ascending and descending pass processing inadequate for achieving optimum temporal resolution [31].

Following the approach taken for Seawinds, QuikSCAT [31], AMSR [39], and ASCAT [40], diurnal temporal resolution can be achieved over the polar regions with OSCAT

by separately processing observations with similar local time. In this chapter, I provide a breakdown of the LTD characteristics of OSCAT in Section 3.1, compare the LTD characteristics of OSCAT with that of QuikSCAT and Seawinds in Section 3.2, and then discuss multi-day LTD SIR images for OSCAT in Section 3.3. The chapter concludes with a summary in Section 3.4.

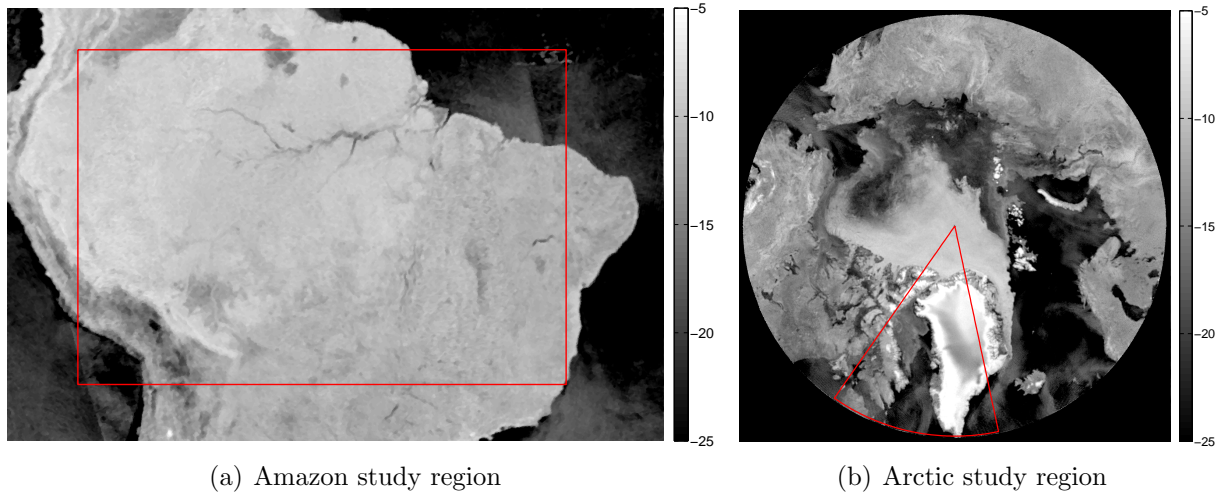
### 3.1 Local Time of Day Characteristics of OSCAT

The Oceansat-2 satellite has an ascending and descending node of approximately 12:00 am and 12:00 pm, meaning the satellite’s northward and southward crossing of the equator are 12:00 am and 12:00 pm local time, respectively. As a result, the LTD of OSCAT observations in equatorial regions are tightly centered around these two times, where LTD for a given observation with longitude and UTC is given by

$$LTD[\text{minutes}] = UTC[\text{minutes}] + 4 \left[ \frac{\text{minutes}}{\text{degree}} \right] \cdot \text{longitude}[\text{degrees}]. \quad (3.1)$$

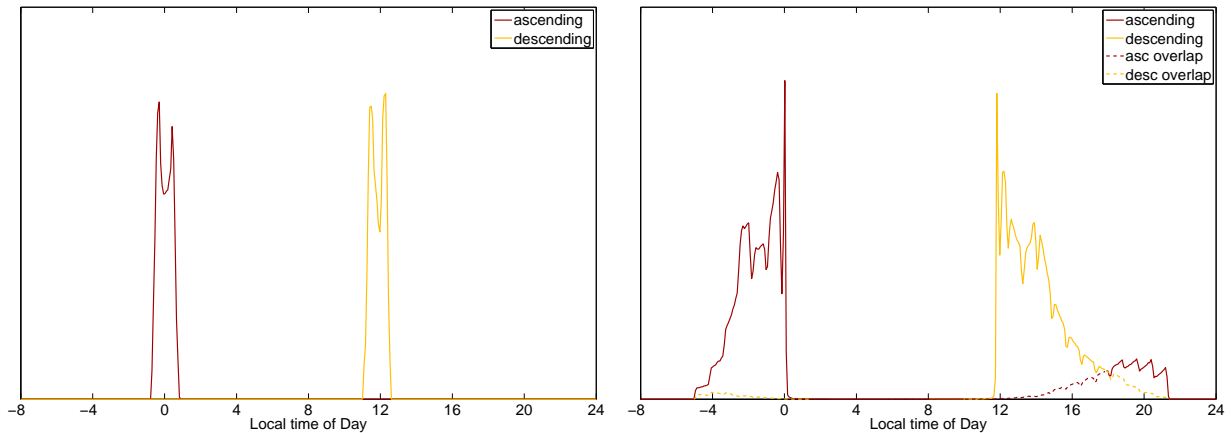
In Figure 3.1c, histograms of LTD for both ascending and descending pass observations are shown over the Amazon region of Figure 3.1a, defined by [33° W to 80° W, 24° S to 7° N]. Comparing the histograms of Figure 3.1c to histograms of the same type over a study region in the Arctic (Figures 3.1b and 3.1d), defined by [33° W to 80° W, 60° N to 90° N], reveals the effects of high latitude on observation LTD. In the polar regions there is a larger spread of measurement LTD for ascending and descending passes as well as swath overlap and day boundary effects near the poles. These have the effect of decreasing temporal resolution.

Swath overlap, a phenomenon common to polar orbiting satellites, is a physical overlapping of measurements from ascending and descending swaths near their points of transition [31], as depicted in Figure 3.2. In relation to LTD, swath overlap effects are manifest as the overlap of ascending and descending LTD coverage as depicted in the histograms of Figure 3.1d. The overlap makes it impossible to uniquely resolve LTD through separation of ascending and descending passes. At lower latitudes, day boundary effects cause  $\sigma^\circ$  measurements from the Arctic study region to be separated in LTD by up to 28 hours.



(a) Amazon study region

(b) Arctic study region



(c) Amazon LTD histogram

(d) Arctic LTD histogram

**Figure 3.1:** The measurements that fall in the (a) Amazon and (b) Arctic study regions are used to create respective histograms of LTD in (c) and (d) for ascending and descending pass data. The study regions are outlined in red on top of  $\mathcal{A}_v$ -SIR images. The grayscale in (a) and (b) is in dB. Note that (d) shows the overlap in LTD for ascending and descending passes at high latitudes, as well as the partition of both ascending and descending measurement LTD individually.

Increased temporal resolution can be achieved over polar regions by exploiting the effects of swath overlap and day boundaries through separation of observations based on similar LTD rather than ascending or descending passes. Data gathered for multiple UTC days over polar regions exhibit LTD overlap in observations from one day to the next. The inter-daily LTD overlap corresponds to similar LTD ranges with high volume of samples. Using the intersection points of ascending and descending swath overlaps as boundaries for

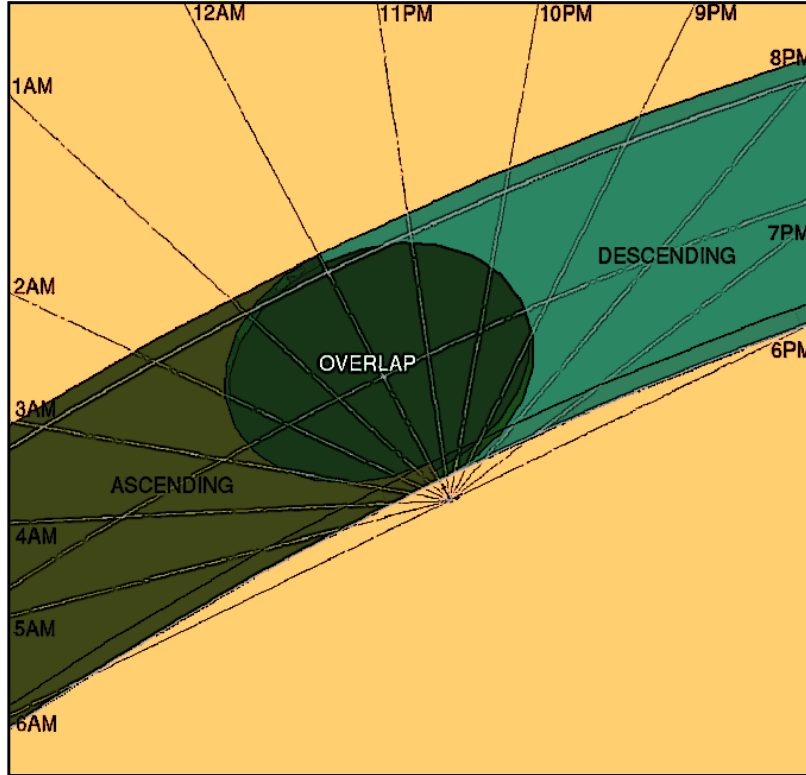


**Figure 3.2:** Diagram illustrating the transition from ascending to descending pass in the Arctic. The lines radiating out from the center depict the local time zone boundaries. Note that there is significant overlap of the ascending and descending data near the pole.

LTD separation, as shown in Figure 3.1d, observations with similar LTD can be subdivided into smaller 8-hour windows, which are defined to correspond to morning (Morn), midday (Mid), and evening (Eve) with respect to local time. A more detailed explanation of LTD windows is given in the next section.

For each polar region, the LTD window that contains no observations is considered invalid. In a given polar region, the valid LTD windows of the scatterometer data are a function of the swath and orbit geometry. A comparative analysis of LTD is performed for various scatterometers in the next section in order to determine the valid LTD windows of polar regions for OSCAT.

### 3.2 Local Time of Day Comparison between Scatterometers

To determine the valid LTD windows of OSCAT used in measurement extraction over polar regions, a LTD analysis of  $\sigma^\circ$  observation times is performed for measurements that

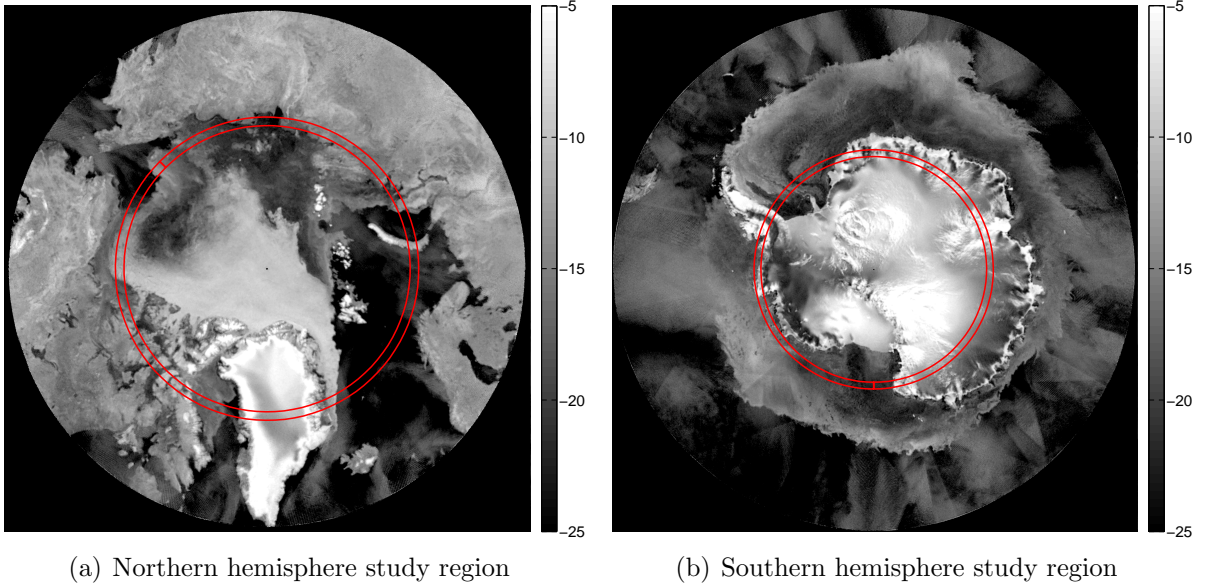


**Figure 3.3:** The study regions (in red) used for measurement LTD extraction in the multi-scatterometer LTD analysis are outlined on  $\mathcal{A}_v$ -SIR images for the (a) northern hemisphere and (b) southern hemisphere. The grayscale is in dB.

lie in the study regions shown for the northern hemisphere (NHe) and southern hemisphere (SHe) in Figure 3.3, defined by  $[180^\circ \text{ W to } 180^\circ \text{ E}, 72^\circ \text{ N to } 73^\circ \text{ N}]$  and  $[180^\circ \text{ W to } 180^\circ \text{ E}, 72^\circ \text{ S to } 73^\circ \text{ S}]$  respectively. For the analysis, the LTD of measurements taken over 3 days UTC in the study regions are plotted versus UTC for different longitude bins as scatterplots. The resulting scatterplots for OSCAT, Seawinds, and QuikSCAT are shown in Figures 3.4 and 3.5 for the Arctic and Antarctic, respectively.

The LTD window boundaries depend on the ascending and descending nodes of the scatterometer. Since the ascending and descending nodes for Seawinds (11 am, 11 pm), QuikSCAT (6 am, 6 pm), and OSCAT (12 am, 12 pm) are all different, their respective LTD window boundaries differ. The plots show that we can define LTD window boundaries for Seawinds and QuikSCAT so they align, though Seawinds should actually be an hour later. As a part of the tandem mission for Seawinds and QuikSCAT, the LTD window boundaries for Seawinds are purposefully chosen to align with QuikSCAT so the windows would correspond exactly between the two. This was done so there would be at least one overlapping window

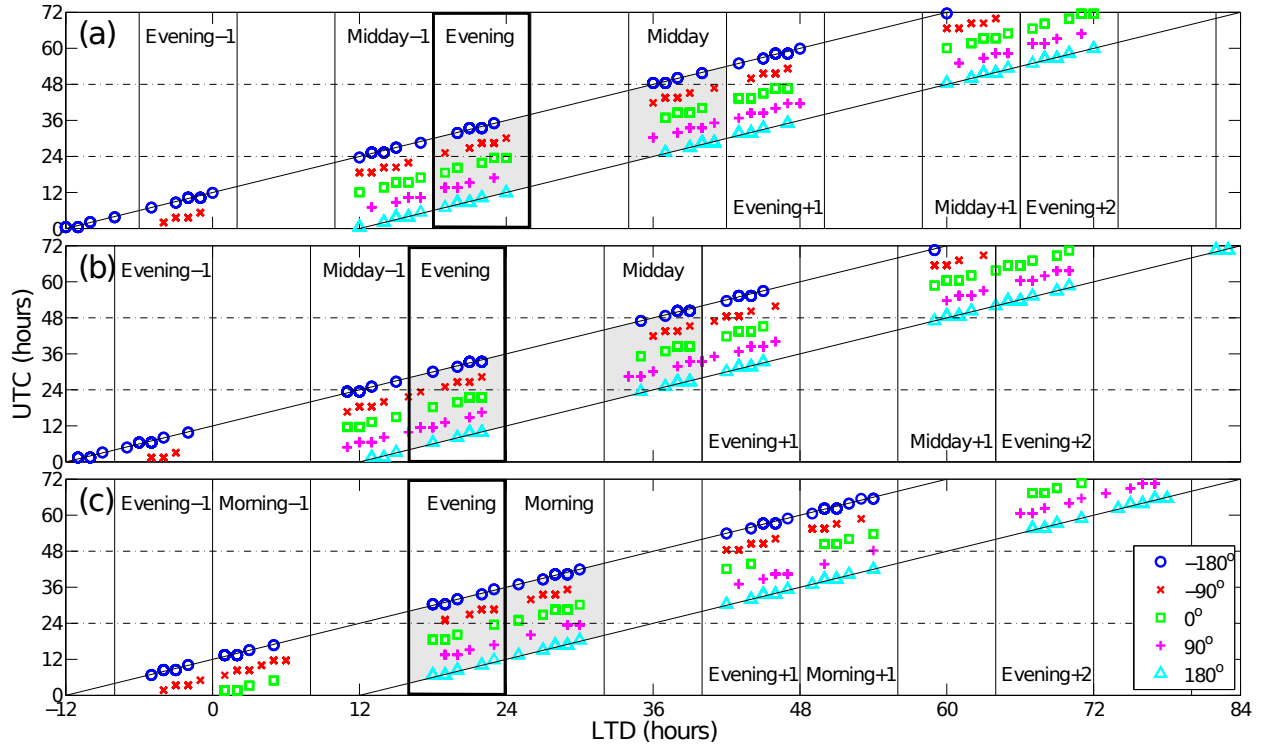


**Figure 3.4:** Scatterplots of LTD versus UTC for measurements taken from the Arctic study region of Figure 3.3a for (a) OSCAT, (b) Seawinds, and (c) QuikSCAT. The scatterplots are binned according to longitude to show the relationship between LTD, UTC, and longitude in the polar regions. The UTC day boundaries are shown as dashed lines. The two lines sloping to the upper right show the linear relationship between LTD and UTC for  $-180^\circ$  and  $180^\circ$  longitude, which show the absolute range for all measurements. The solid vertical lines are the boundaries for the 8-hour LTD windows and contain within them the assigned title for the window. The LTD windows that coincides closely between the scattermeters are given thick black borders. The trapezoidal boxes, referred to as temporal data windows, show the two-dimensional data coverage of the scattermeter with respect to LTD and UTC for a given LTD window. The temporal data windows, out of which measurements are extracted for LTD image processing, are shaded gray. Corresponding LTD windows for 24-hour LTD increments before or after the windows of interest are represented with the name plus  $-1$ ,  $+1$ ,  $+2$ .

(NHe Eve, SHe Morn) of data between the two in each hemisphere that could be used for comparison and validation in scientific studies.

Since the ascending and descending node times of OSCAT correspond most closely with those of Seawinds, the associated time of day assigned to valid LTD windows of Seawinds were also used for OSCAT, even though the window ranges differ by about 2 hours. The

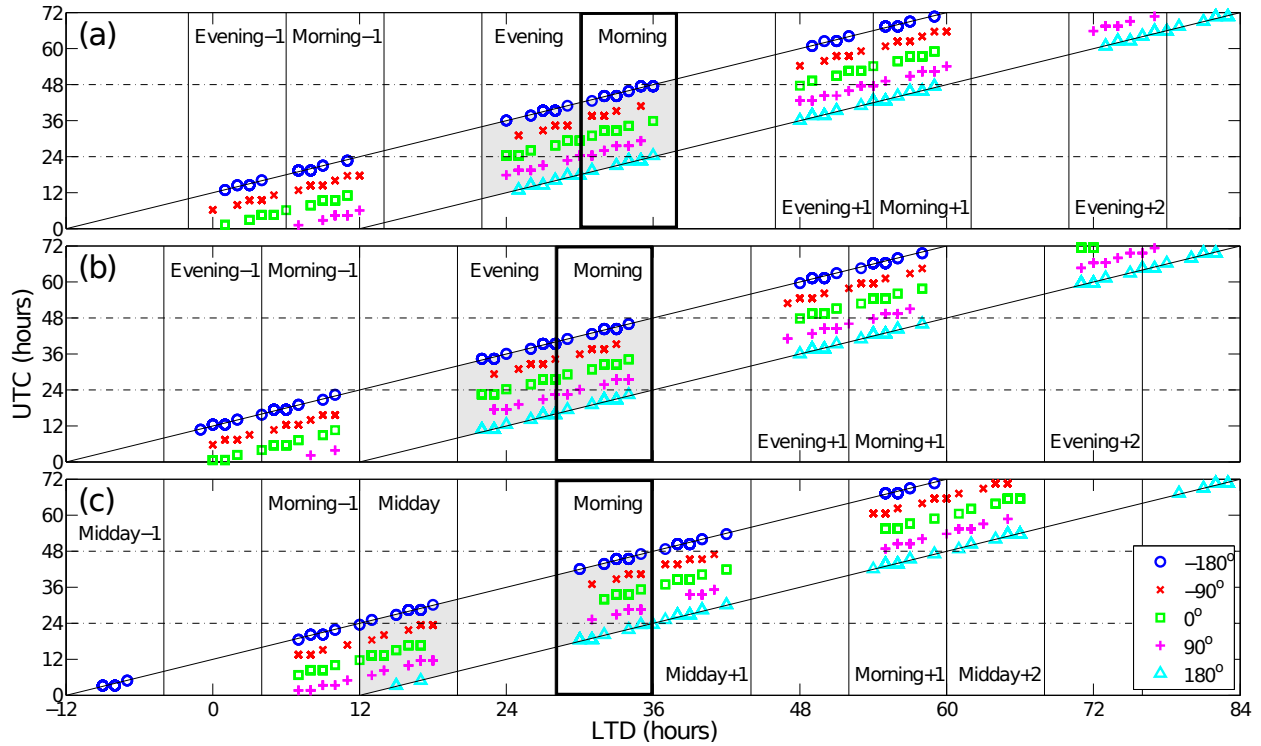


**Figure 3.5:** Scatterplots of LTD versus UTC for measurements taken from the Antarctic study region of Figure 3.3b for (a) OSCAT, (b) Seawinds, and (c) QuikSCAT. The scatterplots are binned according to longitude to show the relationship between LTD, UTC, and longitude in the polar regions. The UTC day boundaries are shown as dashed lines. The two lines sloping to the upper right show the linear relationship between LTD and UTC for  $-180^\circ$  and  $180^\circ$  longitude, which show the absolute range for all measurements. The solid vertical lines are the boundaries for the 8-hour LTD windows and contain within them the assigned title for the window. The LTD windows that coincides closely between the scattermeters are given thick black borders. The trapezoidal boxes, referred to as temporal data windows, show the two-dimensional data coverage of the scattermeter with respect to LTD and UTC for a given LTD window. The temporal data windows, out of which measurements are extracted for LTD image processing, are shaded gray. Corresponding LTD windows for 24-hour LTD increments before or after the windows of interest are represented with the name plus  $-1$ ,  $+1$ ,  $+2$ .

associated time of day for the LTD windows of OSCAT are NHe Eve and Mid, and SHe Eve and Morn (see Figures 3.4 and 3.5).

For a particular scattermeter, the selection of valid LTD windows used for measurement extraction are based on: 1) achieving full temporal data coverage, 2) minimizing number of UTC days used for temporal data extraction, and 3) having temporal data windows coincide as close as possible between scattermeters. In Figures 3.4 and 3.5 trapezoidal

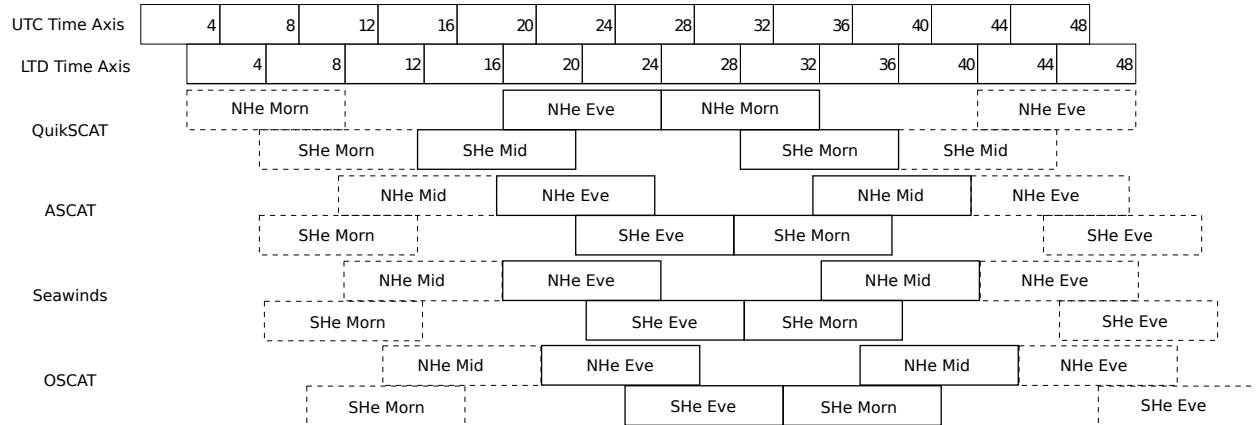


**Figure 3.6:** Local time of day window boundaries defined for QuikSCAT, ASCAT, Seawinds, and OSCAT. Dashed boxes indicate where LTD processing would cover for the adjacent overlapping days' data.

boxes, referred to as temporal data windows, show the two-dimensional data coverage of the scatterometer with respect to LTD and UTC for a given LTD window. Partial temporal data windows are not considered for measurement extraction because of insufficient spatial coverage. Conveniently, QuikSCAT forms two complete temporal data windows in both the NHe and SHe within 48 hours of UTC time, meaning that two days' time is all that is needed to extract enough data for LTD SIR processing at high latitudes.

OSCAT and Seawinds, on the other hand, do not form two complete temporal data windows in both hemispheres within 48 hours of UTC time. Using these two scatterometers, an extra UTC day interval is needed to extract enough data for SIR image processing at high latitudes. Extending to a third day of UTC results in additional temporal data windows that could be considered for LTD processing. For measurement extraction, we choose the earliest two temporal data windows so that the LTD of resultant SIR images coincide with other scatterometers for the given UTC observation interval. All the LTD window boundary definitions for QuikSCAT, ASCAT, Seawinds, and OSCAT are shown for comparison purposes in Figure 3.6.

Although OSCAT LTD window boundaries do not perfectly align with that of QuikSCAT, there is one LTD window in each hemisphere that coincides very closely (outlined in thick black borders in Figures 3.4 and 3.5, the NHe Eve and SHe Morn. This can be

very useful in cross-calibration efforts between the two scatterometers as well as extending long term scientific studies of diurnal phenomena in the polar regions through OSCAT.

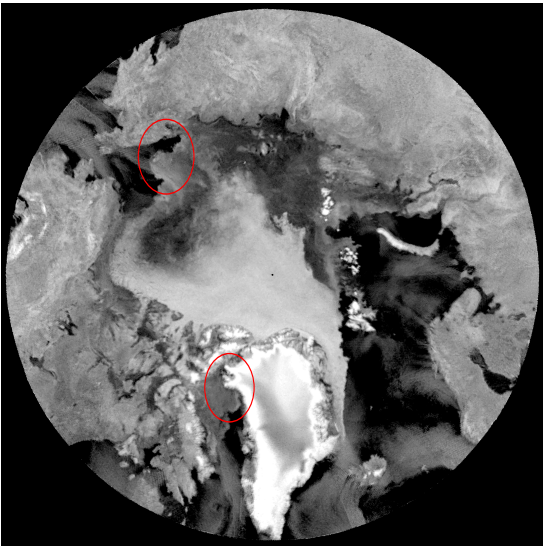
### 3.3 Local Time of Day Images

Looking at the plots of Figures 3.4 and 3.5, it is important to notice that there is a one-to-one relationship between LTD and UTC, and the LTD windows repeat every 24 hours of LTD. This means that SIR images can be created daily (every 24 hours UTC) using LTD processing. Because the daily LTD SIR images incorporate data that spans more than 24 hours of UTC, the images require extraction of measurements from more than one UTC day, as shown by the shaded areas in Figures 3.4 and 3.5. For OSCAT, daily NHe and SHe Eve SIR images require 2 days of UTC data, and daily NHe Mid and SHe Morn SIR images require 3 days of UTC data. The UTC day for which the LTD SIR images best correspond is somewhat ambiguous because each longitude corresponds to a different 24-hour subset of UTC. However, we choose the UTC day interval that is representative of the majority of the measurements to be used in LTD SIR processing. Thus, an LTD image whose day range is  $d_1$  to  $d_2 = d_1 + 2$  corresponds to a daily UTC image for day  $d = d_1 + 1$ .

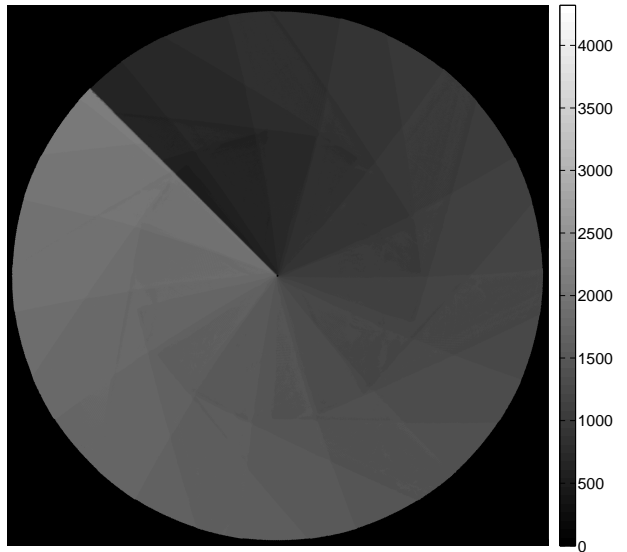
To test LTD processing on OSCAT,  $\mathcal{A}_v$ - and  $\mathbf{p}$ -SIR images of the Arctic and Antarctic regions are created for JD 310-312 of 2009. For an  $\mathcal{A}_v$ -SIR image, each pixel is the weighted average  $\sigma^\circ$  value of all measurements covering that pixel. For a  $\mathbf{p}$ -SIR image, each pixel is the weighted average UTC value of all measurements covering that pixel. Resulting  $\mathcal{A}_v$ - and  $\mathbf{p}$ -SIR images are shown in Figures 3.7 and 3.8. For comparison, the  $\mathcal{A}_v$ - and  $\mathbf{p}$ -SIR images for the same regions made without LTD processing are shown in Figure 3.9. Differences can be seen in the LTD  $\mathcal{A}_v$ -SIR images that can't be seen in the non-LTD  $\mathcal{A}_v$ -SIR images as a result of diurnal earthly phenomena. Examples of diurnal earthly phenomena might include surface ice melting events, sea ice formation, snow accumulation, etc.

### 3.4 Summary

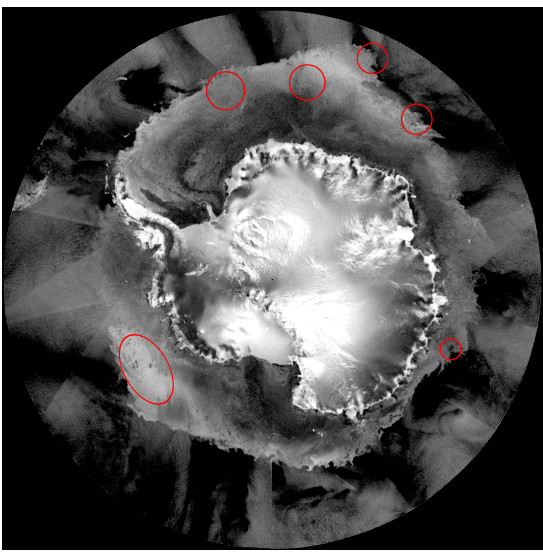
Local time of day processing can be used to improve temporal resolution of OSCAT SIR images over the polar regions. Local time of day processing is a temporal resolution improvement procedure for SIR imagery of polar-orbiting sun-synchronous remote sensing



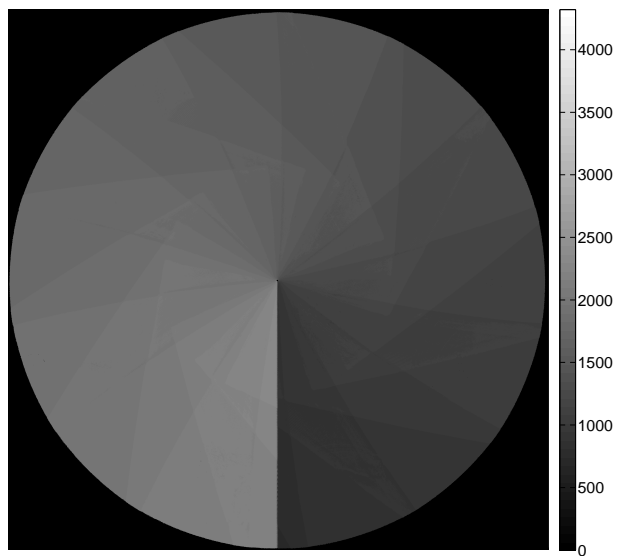
(a) Arctic evening LTD  $\mathcal{A}_v$ -SIR



(b) Arctic evening LTD  $\mathbf{p}$ -SIR

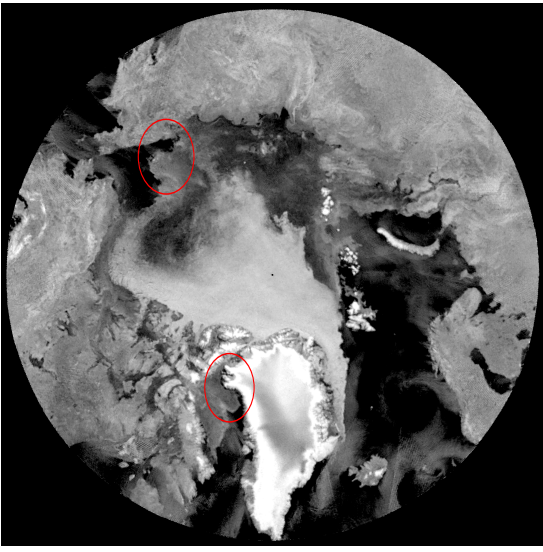


(c) Antarctic evening LTD  $\mathcal{A}_v$ -SIR

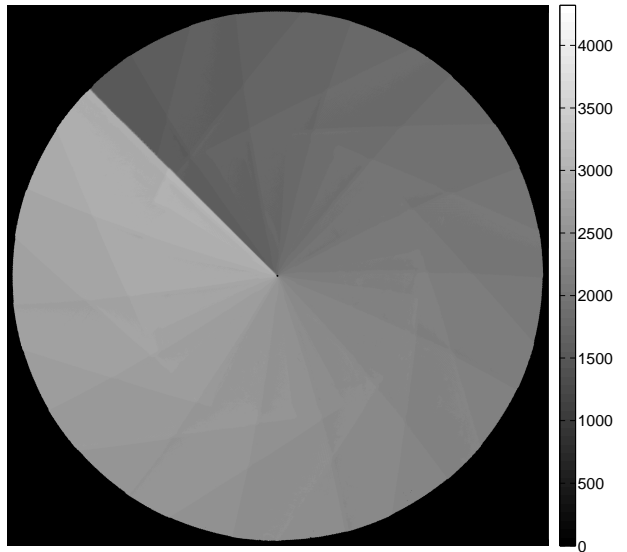


(d) Antarctic evening LTD  $\mathbf{p}$ -SIR

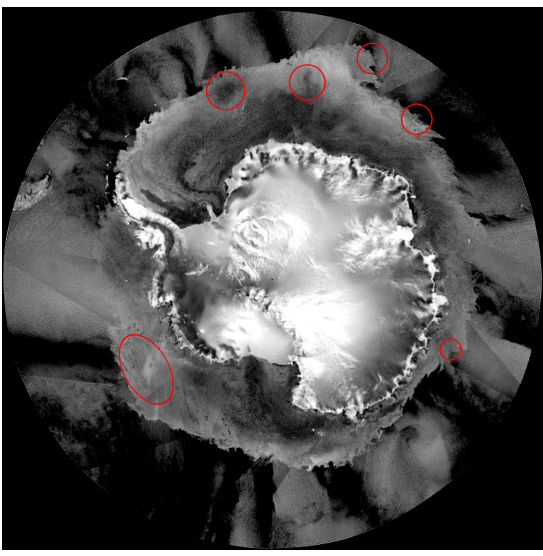
**Figure 3.7:** OSCAT evening LTD  $\mathcal{A}_v$ - and  $\mathbf{p}$ -SIR images of the Arctic and Antarctic regions for JD 310-312 of 2009. The  $\mathcal{A}_v$ -SIR images are measured in dB, and the  $\mathbf{p}$ -SIR images are measured in minutes from UTC midnight of JD 310 of 2009. The red circles mark areas in the image that exhibit some notable changes.



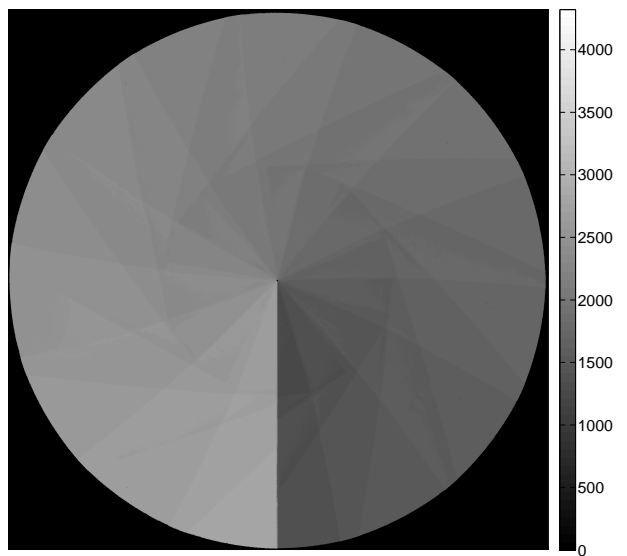
(a) Arctic midday LTD  $\mathcal{A}_v$ -SIR



(b) Arctic midday LTD  $\mathbf{p}$ -SIR

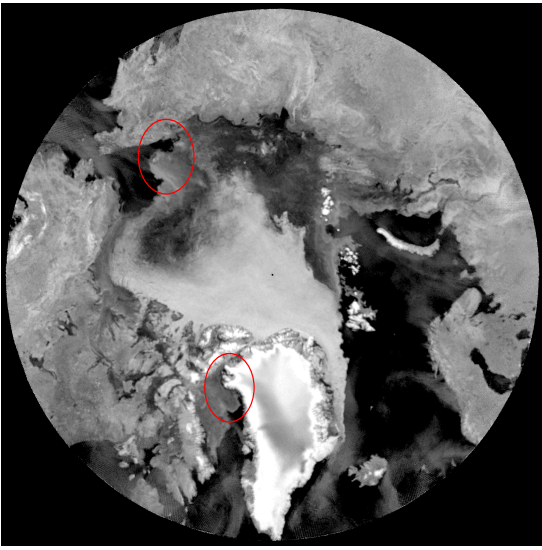


(c) Antarctic morning LTD  $\mathcal{A}_v$ -SIR

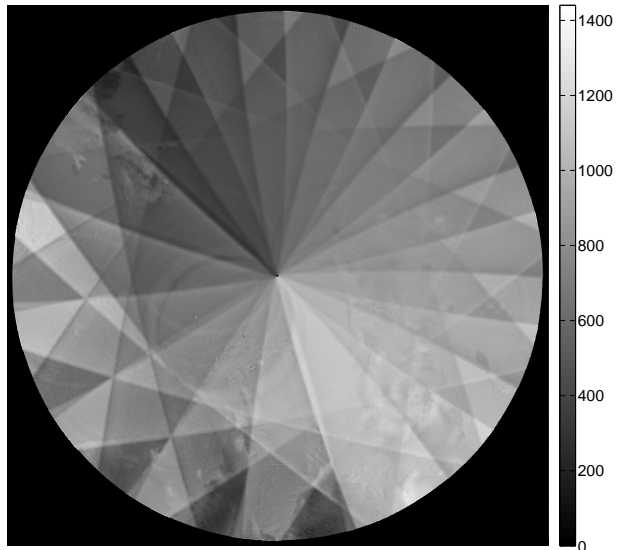


(d) Antarctic morning LTD  $\mathbf{p}$ -SIR

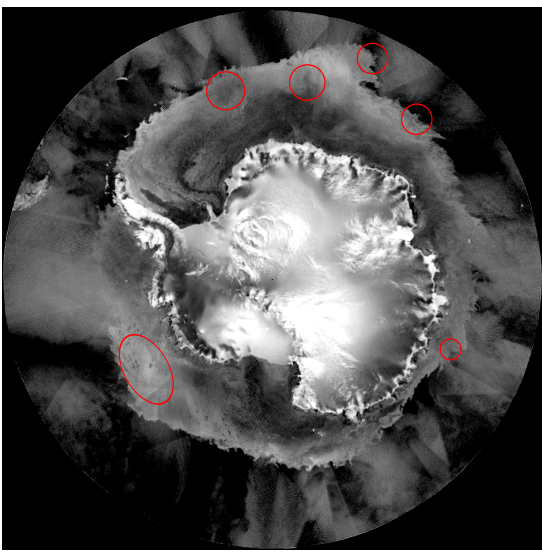
**Figure 3.8:** OSCAT midday and morning LTD  $\mathcal{A}_v$ - and  $\mathbf{p}$ -SIR images for JD 310-312 of 2009 for the Arctic and Antarctic, respectively. The  $\mathcal{A}_v$ -SIR images are measured in dB, and the  $\mathbf{p}$ -SIR images are measured in minutes from UTC midnight of JD 310 of 2009. The red circles mark areas in the image that exhibit some notable changes.



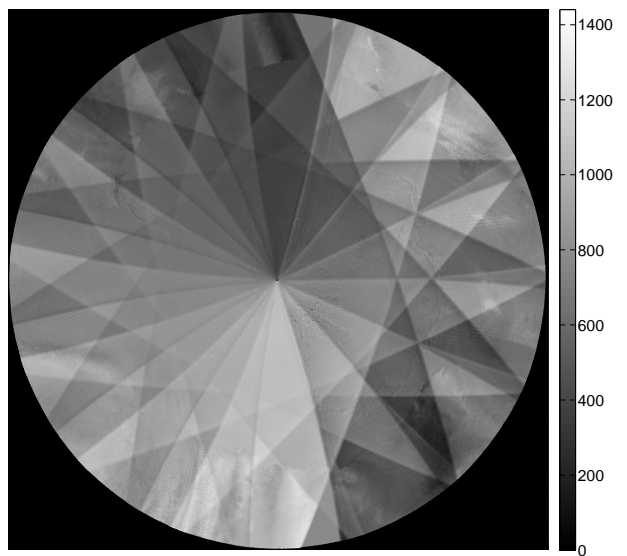
(a) Arctic daily non-LTD  $\mathcal{A}_v$ -SIR



(b) Arctic daily non-LTD  $\mathbf{p}$ -SIR



(c) Antarctic daily non-LTD  $\mathcal{A}_v$ -SIR



(d) Antarctic daily non-LTD  $\mathbf{p}$ -SIR

**Figure 3.9:** OSCAT daily non-LTD  $\mathcal{A}_v$ - and  $\mathbf{p}$ -SIR images of the Arctic and Antarctic regions for JD 311 of 2009. The  $\mathcal{A}_v$ -SIR images are measured in dB and  $\mathbf{p}$ -SIR images are measured in minutes from UTC midnight of JD 311 2010. The red circles mark areas in the image that exhibit some notable changes.

instruments. For LTD processing,  $\sigma^\circ$  observations used to create SIR images of polar regions are processed separately according to corresponding 8-hour LTD windows. Seawinds and OSCAT have similar LTD characteristics, including LTD window boundaries within an hour of each other and four corresponding temporal data windows. Based on the results of Seawinds, four temporal data windows have been defined for OSCAT: NHe Eve, NHe Mid, SHe Eve, and SHe Morn. OSCAT daily LTD images are created for NHe and SHe Eve temporal data windows using 2-day UTC intervals, and 3-day UTC intervals for NHe Mid and SHe Morn temporal data windows. LTD images allow for resolution of diurnal features of the polar caps. This can help alleviate calibration biases due to diurnal fluctuation in  $\sigma^\circ$  during relative cross-calibration procedures based on extended-area natural land targets.



## Chapter 4

### Relative Cross-calibration

A seamless transition in the SCP data time series from QuikSCAT to OSCAT requires a thorough relative cross-calibration of the instruments. In this chapter, cross-calibration is done separately for raw  $\sigma^\circ$  data and SIR  $\sigma^\circ$  image data by comparing the mean and standard deviation of data collected from homogeneous extended-area targets over the Amazon to obtain a relative calibration factor. For SIR image  $\sigma^\circ$  data, an additional extended-area target over the interior of Greenland is also utilized. Because of insufficient azimuthal geometries in  $\sigma^\circ$  measurements over parts of Greenland, the intended cross-calibration procedure for raw measurements over Greenland has limitations.

Both regions have been found to be mostly homogeneous; however, some concern has been noted over observed diurnal cycles in  $\sigma^\circ$  [11, 26, 30, 31, 41]. For example, diurnal fluctuation of  $\sigma^\circ$  over the Amazon caused by dew accumulation in the canopy during the early morning (local time) is reported as being within 0.5-1.0 dB [11, 26, 30]. To avoid potential biases in relative calibration factors, data is analyzed separately based on local time of day (LTD). Thus, I separately analyze data based on ascending or descending pass over the Amazon and using LTD SIR images over Greenland.

The chapter begins by presenting a method for selecting an extended-area target for use in cross-calibration in Section 4.1. Next, Section 4.2 presents the cross-calibration method employed for raw  $\sigma^\circ$  data, including insights into the stability of the OSCAT instrument and the diurnal cycle of the Amazon. The method for cross-calibration of SIR image  $\sigma^\circ$  data is then presented in Section 4.3, and the chapter is concluded with a summary in Section 4.4.

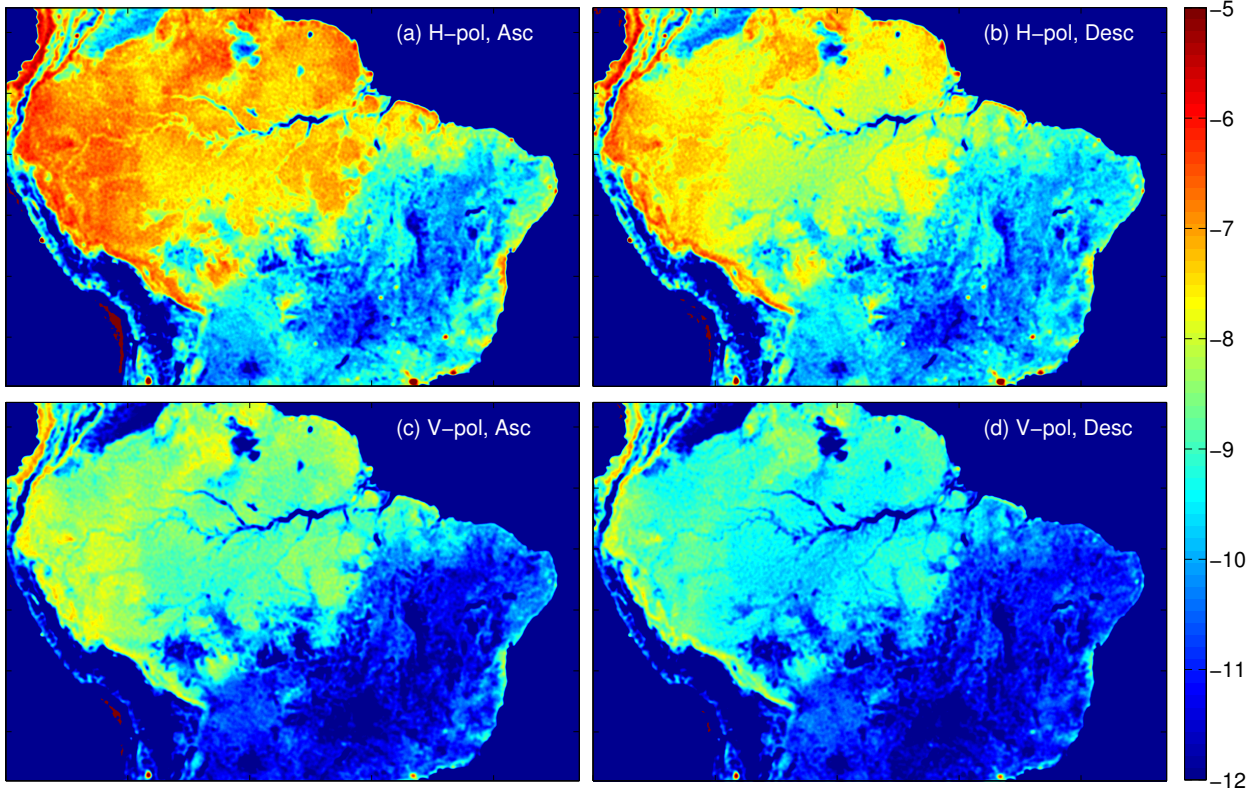


**Figure 4.1:** Images of mean QuikSCAT egg  $\mathcal{A}_h$ - and  $\mathcal{A}_v$ -SIR images corresponding to morning and evening passes over the Amazon for JD 181-205 of 2009. The color scale is in dB.

#### 4.1 Sampling Region

For measurement cross-calibration purposes, it is important that the extended-area target be homogeneous, isotropic, and temporally stable to avoid potential biases in relative calibration factors due to effects of polarization, azimuth response of  $\sigma^\circ$ , or temporal fluctuation in  $\sigma^\circ$ . It is also important that the extended-area target is large enough to provide a sufficient number of measurements for reduction of noise and to ensure that the response function of the antenna is mostly contained within the region. To determine an extended-area target exhibiting a homogeneous, isotropic, and temporally stable backscatter response, a method of generating a data selection mask using QuikSCAT egg  $\mathcal{A}_h$ - and  $\mathcal{A}_v$ -SIR images is employed. The method is similar to approaches taken by previous researchers [27, 28], except that it takes into account possible time of day fluctuations in the backscatter response. QuikSCAT SIR images of the Amazon used in the method are created separately

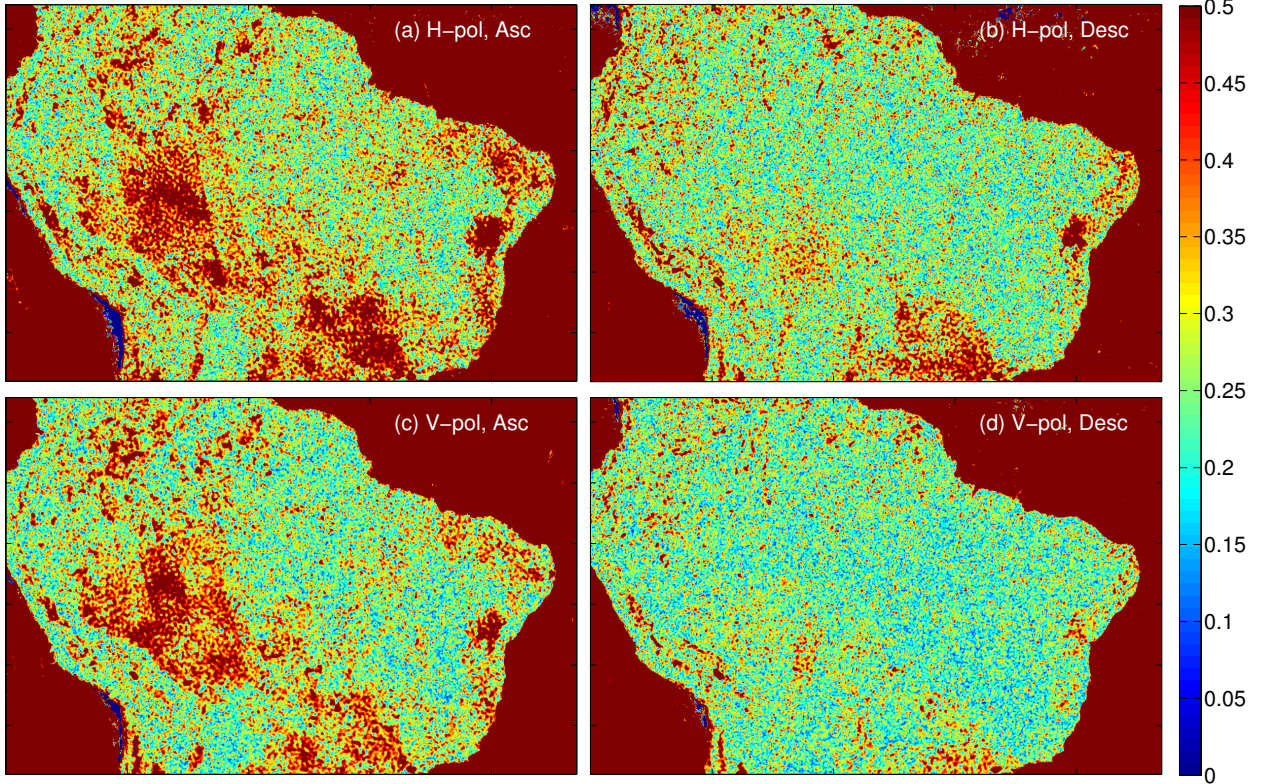


**Figure 4.2:** Images of standard deviation QuikSCAT egg  $\mathcal{A}_h$ - and  $\mathcal{A}_v$ -SIR images corresponding to morning and evening passes over the Amazon for JD 181-205 of 2009.

for ascending and descending passes using three days of data every four days, and LTD SIR images of Greenland are created as outlined in the previous section.

#### 4.1.1 Data Selection Mask

To determine a data selection mask for the Amazon area, mean and standard deviation images of  $\sigma^\circ$  are computed for H-pol and V-pol based on the LTD as shown in Figures 4.1 and 4.2. Pixels corresponding to locations in the Amazon with a mean radar response within  $\pm 0.5$  dB of a typical H-pol  $\sigma^\circ$  value  $\alpha_{h,m} = -7.2$  dB during the morning with a standard deviation less than 0.5 dB are intermediately masked. The typical  $\sigma^\circ$  value  $\alpha_{\text{pol,LTD}}$  for the remaining combinations of polarization and LTD are determined by

$$\alpha_{\text{pol,LTD}} = (\alpha_{h,m} - \bar{\alpha}_{h,m}) + \bar{\alpha}_{\text{pol,LTD}}, \quad (4.1)$$

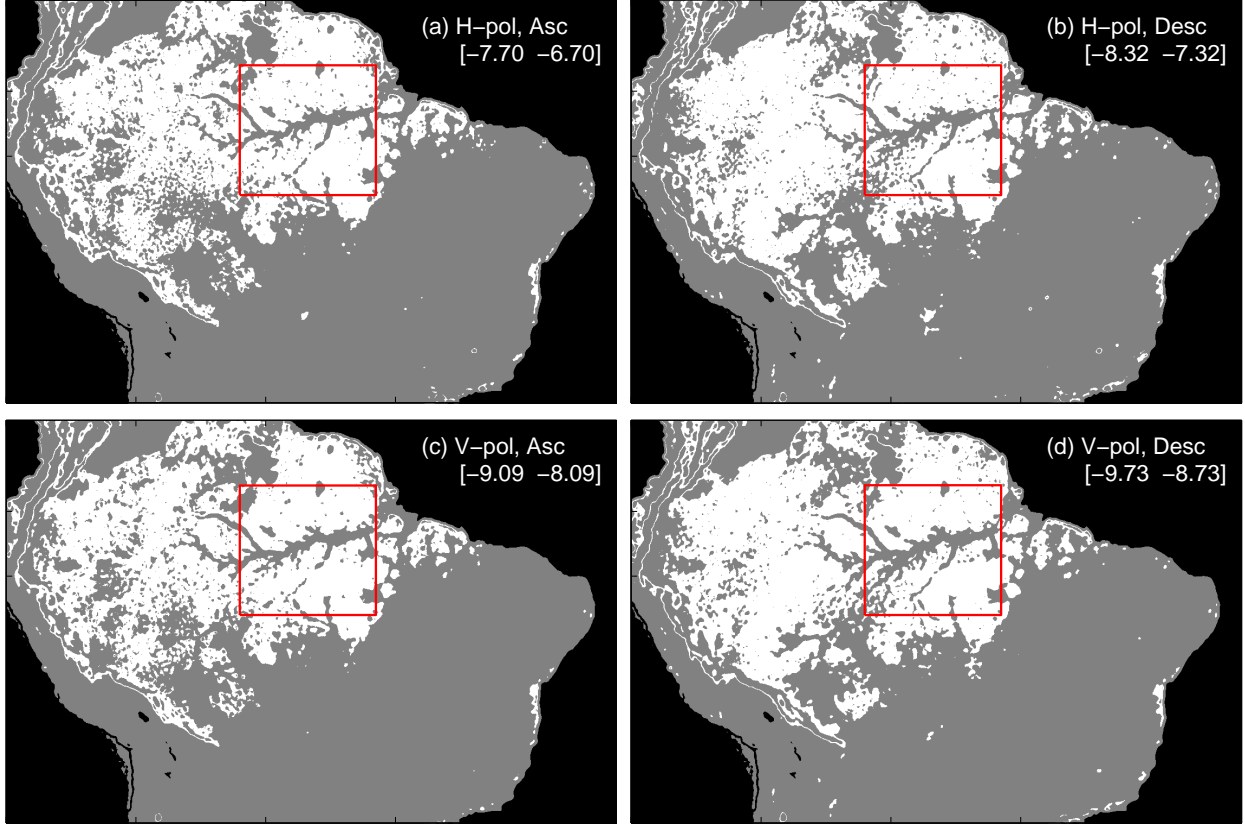


**Figure 4.3:** Images of the intermediate data selection masks generated for H-pol and V-pol  $\sigma^\circ$  measurements corresponding to the morning and evening passes over the Amazon. White represents the data selection mask, gray represents land, and black represents ocean. The adjusted range of mean  $\sigma^\circ$  used to generate a mask is specified in the square brackets in each image.

where  $\bar{\alpha}_{h,m}$  is the mean of H-pol morning  $\sigma^\circ$  contained within the intermediate H-pol morning mask and  $\bar{\alpha}_{\text{pol,LTD}}$  is the mean  $\sigma^\circ$  contained within the intermediate morning mask for a particular polarization and LTD. As was done for H-pol  $\sigma^\circ$  of the morning, intermediate masks are created for the remaining combinations of polarization and LTD by selecting pixels within  $\alpha_{\text{pol,LTD}} \pm 0.5$  dB for each polarization and LTD. Examples of intermediate masks generated for the Amazon are shown in Figure 4.3.

The final data selection mask is generated by combining the overlapping pixels of the intermediate masks into one and median filtering to help smooth edges and promote a contiguous sampling region. For the Amazon basin, only mask locations that fall within a box defined by  $[51^\circ 30' \text{ W to } 62^\circ \text{ W}, 8^\circ \text{ S to } 2^\circ \text{ N}]$  are included in the final data selection

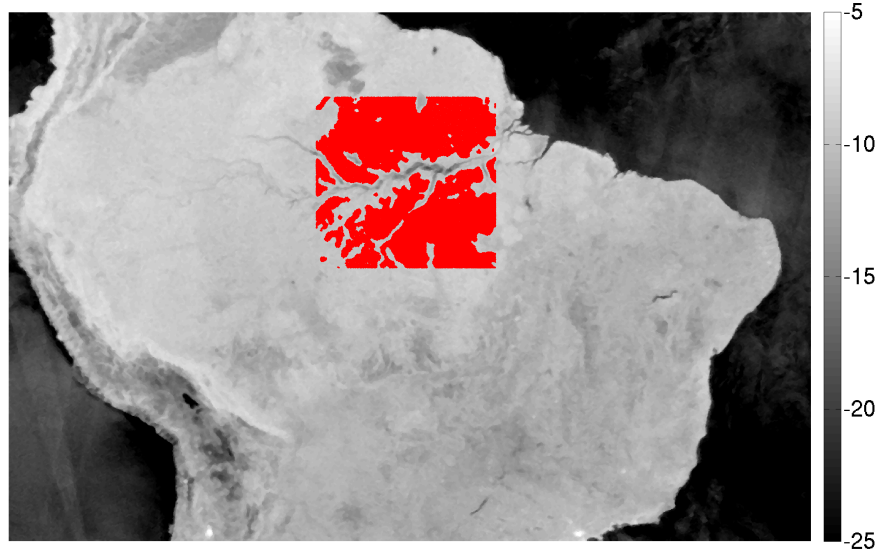


**Figure 4.4:** Image of the final data selection mask for the Amazon basin. The mask, shown in red, is superimposed on a QuikSCAT slice  $\mathcal{A}_v$ -SIR image of the Amazon corresponding to JD 205-208 of 2009. The grayscale is in dB.

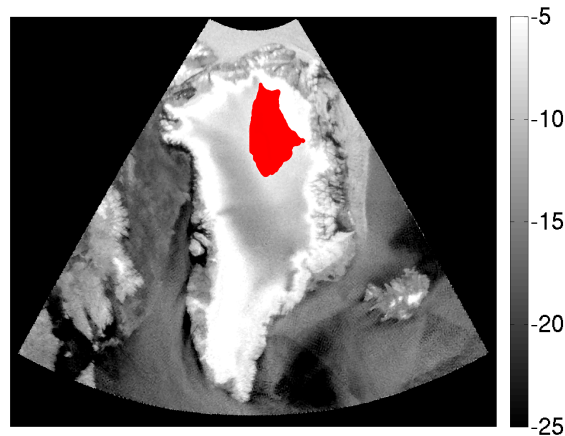


**Figure 4.5:** Image of the final data selection mask for the interior of Greenland. The mask, shown in red, is superimposed on a QuikSCAT slice  $\mathcal{A}_v$ -SIR image of Greenland corresponding to JD 325 of 2009. The grayscale is in dB.

mask. Figure 4.4 shows the final data selection mask for the Amazon basin. The same basic procedure is followed to create a data selection mask for the interior region of Greenland, except that the first intermediate mask is made using the typical H-pol  $\sigma^\circ$  value  $\alpha_{h,e} = -6.1$  dB during the evening. Figure 4.5 shows the final data selection mask for the interior region of Greenland.

## 4.2 Raw Data Calibration Procedure

Because OSCAT and QuikSCAT are conically scanning pencil-beam scatterometers, the methodology for analyzing their raw data differs from traditional fan-beam scatterometers. The azimuthal response of raw  $\sigma^\circ$  measurements selected from the homogeneous extended-area target of the Amazon basin is analyzed per beam between OSCAT and QuikSCAT to verify homogeneity of instrument backscatter response over the region. Azimuth dependence in the observed  $\sigma^\circ$  measurements over the extended-area target is estimated and used to normalize the measurements. Because of the extended incidence angle range of slice measurements, a small incidence angle correction based on Eq. (2.3) is applied prior to analyzing the azimuthal response of slice  $\sigma^\circ$  measurements. The mean and standard deviation statistics of the normalized  $\sigma^\circ$  measurements are then compared to determine a relative calibration factor to be applied to OSCAT L1B data.

From JD 309 to 327 of 2009, the OSCAT and QuikSCAT missions overlap, allowing direct comparison of L1B data corresponding to the same time period. This limits temporal biases in relative cross-calibration. Because the OSCAT L1B data corresponding to these days are not representative of the most recent data processing algorithms employed by ISRO, the results are not necessarily valid for future data. However, since the results are valid for a large portion of the OSCAT L1B data currently available, they are provided in Appendix A for reference. The results demonstrate the poor quality of the initial OSCAT  $\sigma^\circ$  data, while also providing relative calibration factors valid for the raw  $\sigma^\circ$  measurements of the earlier L1B data.

In this chapter, only results obtained with the most recent version of OSCAT data are provided. The procedure is performed using OSCAT L1B data for JD 3 through 20 of 2012 and QuikSCAT L1B data for JD 3 through 20 of 2009 to provide a relative calibration factor valid for future OSCAT data. Though it is possible that there may be a mean difference in the  $\sigma^\circ$  response between the two years, choosing days corresponding to the same season helps to minimize temporal biases.

To account for the possible diurnal effects on the  $\sigma^\circ$  response, the data is analyzed for ascending and descending passes separately, while also being analyzed collectively. This is done to investigate biases that result from not accounting for LTD fluctuations in  $\sigma^\circ$ . It is

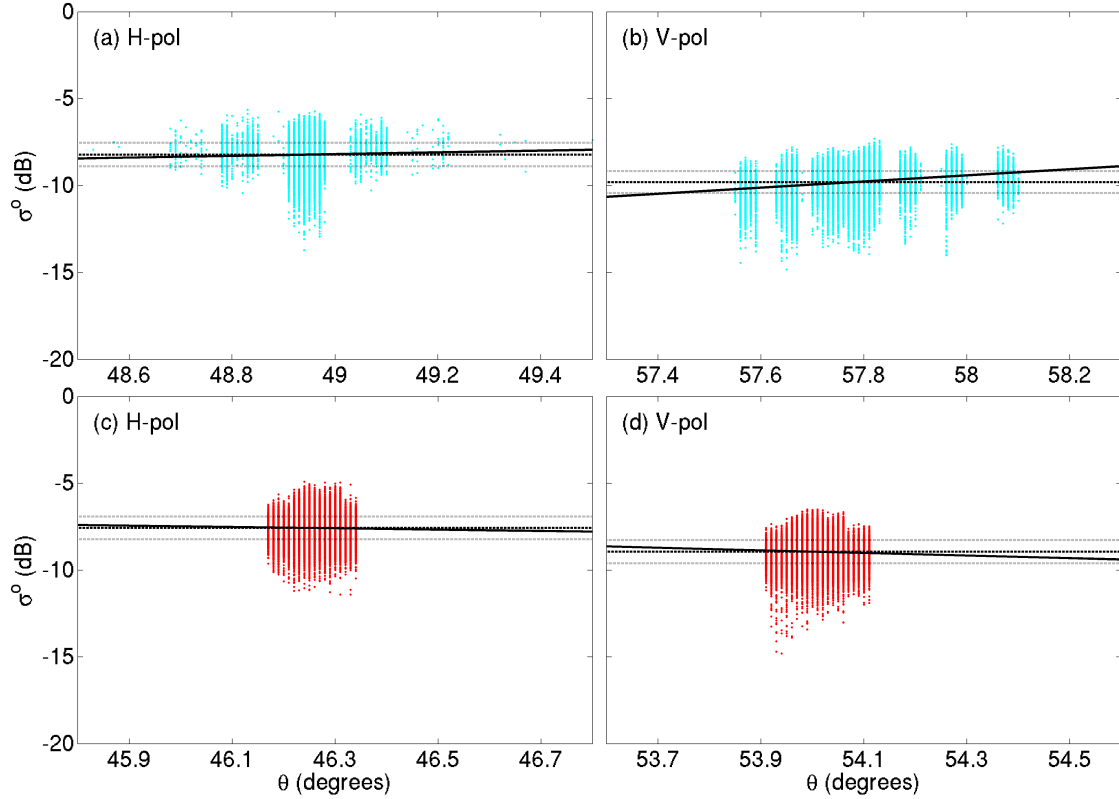


**Figure 4.6:** Scatterplots of egg  $\sigma^\circ$  versus  $\theta$  for combined pass data of OSCAT (a) H-pol and (b) V-pol, and QuikSCAT (c) H-pol and (d) V-pol.

shown that there is 0.3 dB bias in relative calibration factors obtained by processing the data collectively. The ascending and descending passes of OSCAT correspond to midnight and noon local time, respectively. The ascending and descending passes of QuikSCAT correspond to 6:00 a.m. and 6:00 p.m. local time, respectively.

#### 4.2.1 Incidence Response

The ascending and descending pass combined  $\sigma^\circ$  versus  $\theta$  response for the selected mask area is shown for eggs and slices in Figures 4.6 and 4.7, respectively. Plots of  $\sigma^\circ$  versus  $\theta$  show a linear least-squares fit to the data based on the model of Eq. 2.3 with a solid line, mean with a dashed line, and standard deviation with dotted lines. Because the range of  $\theta$  for egg measurements is less than a few tenths of a degree, no substantial relationship between  $\sigma^\circ$  and  $\theta$  is expected and estimates of the  $\sigma^\circ$  incidence response are considered unimportant. Thus, no incidence correction is applied to egg  $\sigma^\circ$  measurements.

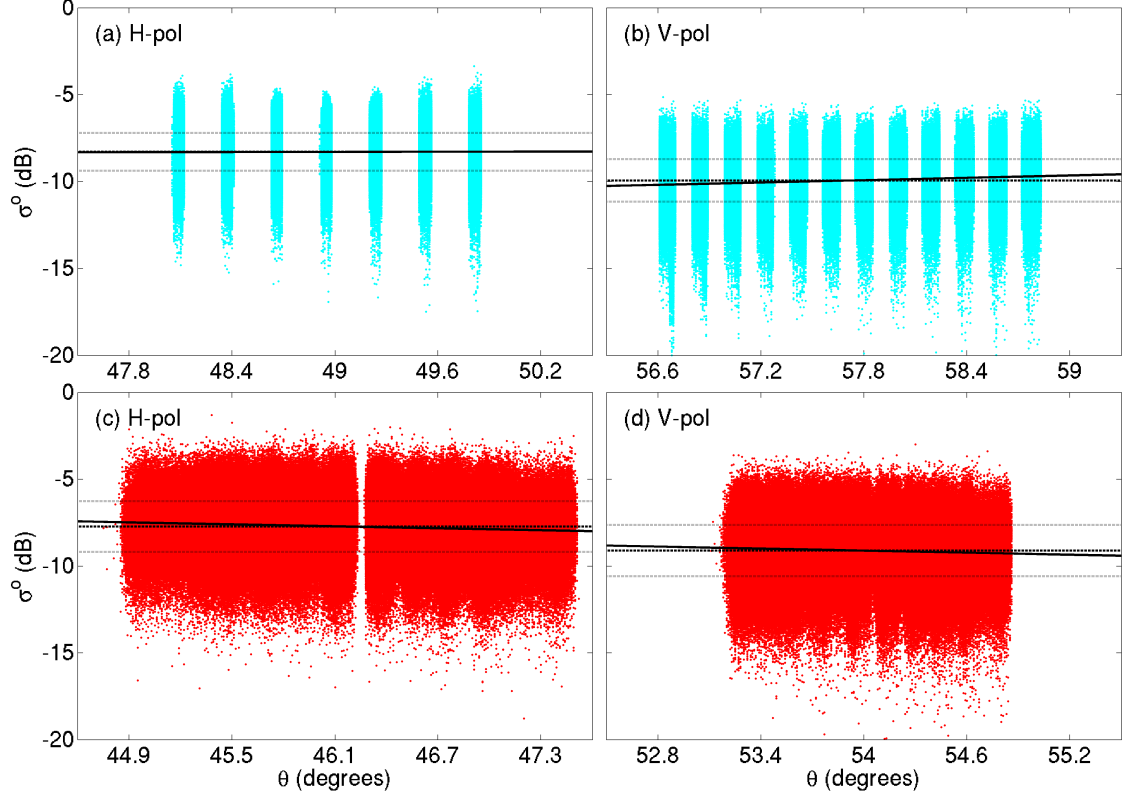


**Figure 4.7:** Scatterplots of slice  $\sigma^\circ$  versus  $\theta$  for combined pass data of OSCAT (a) H-pol and (b) V-pol, and QuikSCAT (c) H-pol and (d) V-pol.

Slice  $\sigma^\circ$  measurements, however, have a  $\theta$  range that extends up to  $1.5^\circ$ . Therefore, it is expected that the  $\theta$  dependence in slice  $\sigma^\circ$  measurements needs to be corrected. Upon estimation of the slice  $\sigma^\circ(\theta)$  incidence angle response by solving for  $\mathcal{A}$  and  $\mathcal{B}$  of the model in Eq. 2.3 using least-squares, the  $i^{\text{th}}$  incidence angle normalized measurement is obtained by

$$\sigma_i^\circ = z_i(\theta) - \mathcal{B}(\theta_i - \Theta), \quad (4.2)$$

where  $z_i(\theta)$  is the  $i^{\text{th}}$  measured valued of normalized radar backscatter. Figures 4.8 and 4.9 show plots of  $\sigma^\circ$  versus  $\theta$  for ascending and descending pass data, respectively. The linear relationship between QuikSCAT  $\sigma^\circ$  and  $\theta$  is negative, as expected, and invariant to ascending or descending pass. OSCAT  $\sigma^\circ$  measurements, however, exhibit a positive linear relationship with  $\theta$  that changes slightly from ascending to descending pass.

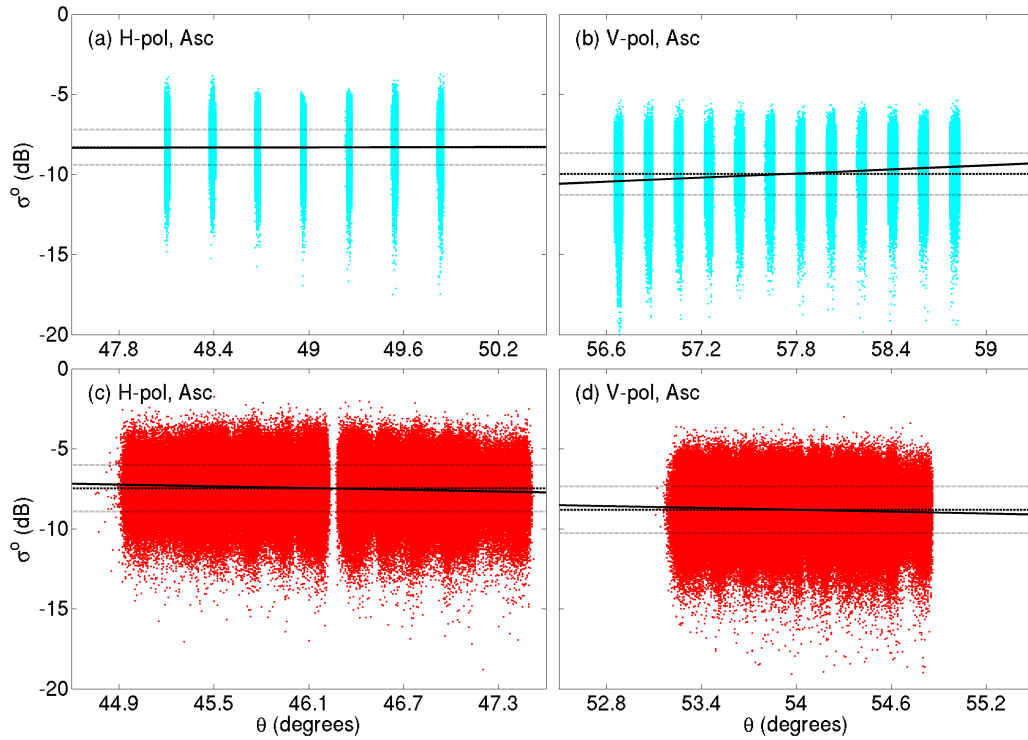


**Figure 4.8:** Scatterplots of slice  $\sigma^\circ$  versus  $\theta$  for ascending pass data of OSCAT (a) H-pol and (b) V-pol, and QuikSCAT (c) H-pol and (d) V-pol.

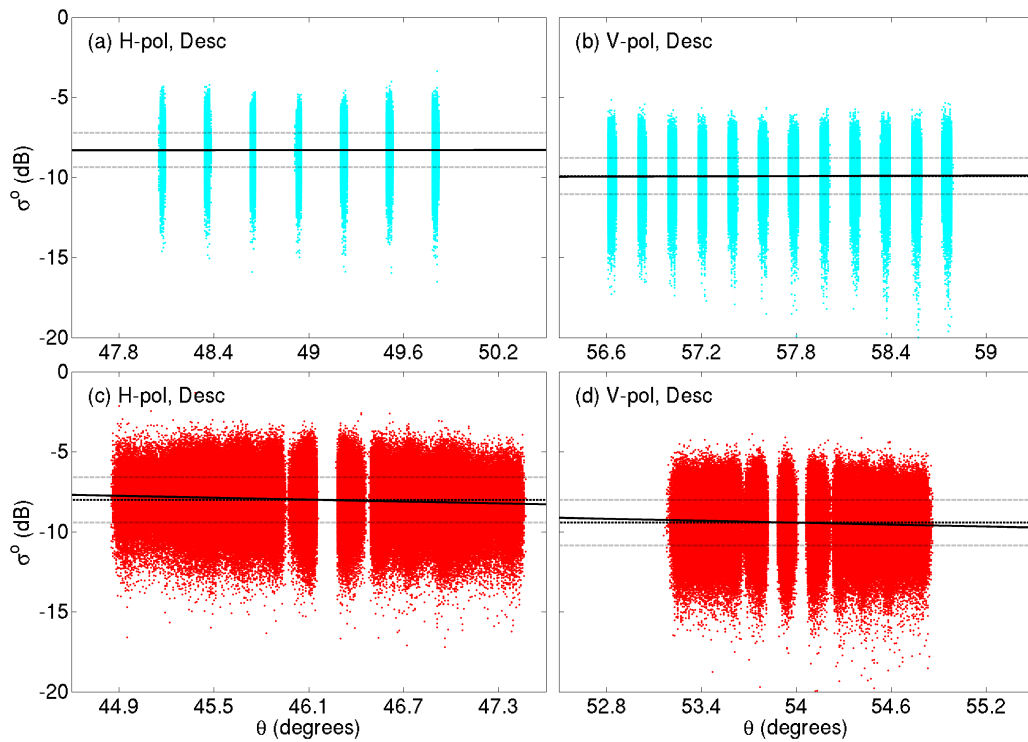


**Figure 4.9:** Scatterplots of slice  $\sigma^\circ$  versus  $\theta$  for descending pass data of OSCAT (a) H-pol and (b) V-pol, and QuikSCAT (c) H-pol and (d) V-pol.

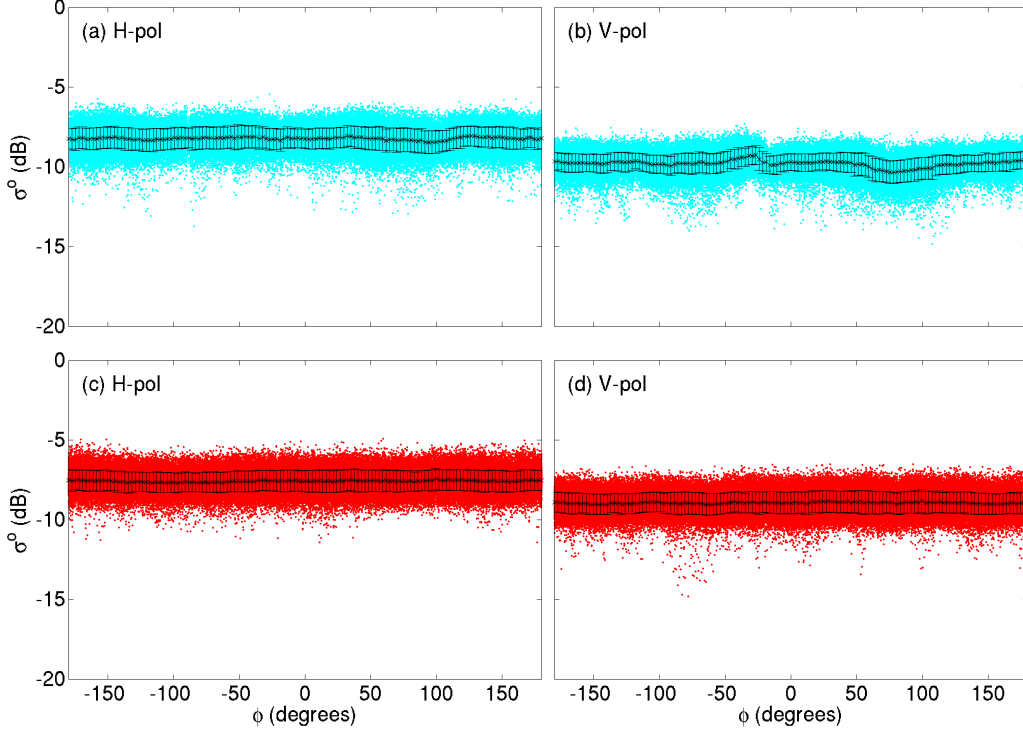


**Figure 4.10:** Scatterplots of egg  $\sigma^\circ$  versus  $\phi$  for combined pass data of OSCAT (a) H-pol and (b) V-pol, and QuikSCAT (c) H-pol and (d) V-pol.

### 4.2.2 Azimuth Response

The ascending and descending pass combined  $\sigma^\circ$  versus  $\phi$  response for the mask-selected area is shown for egg and  $\theta$  normalized slice measurements in Figures 4.10 and 4.11, respectively. Densely spaced mean and standard deviation bars are shown on plots of  $\sigma^\circ$  versus  $\phi$ . The H-pol and V-pol  $\sigma^\circ$  measurements of QuikSCAT appear to be independent of  $\phi$ , as expected over the Amazon basin. For OSCAT, the H-pol  $\sigma^\circ$  measurements are mostly independent of  $\phi$ , with slight azimuthal modulation in the V-pol  $\sigma^\circ$  response. Azimuth angle dependency in  $\sigma^\circ$  measurements needs to be corrected before relative cross-calibration. To do this, the relationship of  $\sigma^\circ$  with  $\phi$  is estimated and removed.

The relationship between  $\sigma^\circ(\phi)$  and  $\phi$  for the  $i^{\text{th}}$  measurement is modeled with a fourth-order ( $N = 4$ ) Fourier series of the form

$$\sigma^\circ(\phi_i) = C + \sum_{k=1}^N [D_k \cos(k\phi_i) + F_k \sin(k\phi_i)]. \quad (4.3)$$

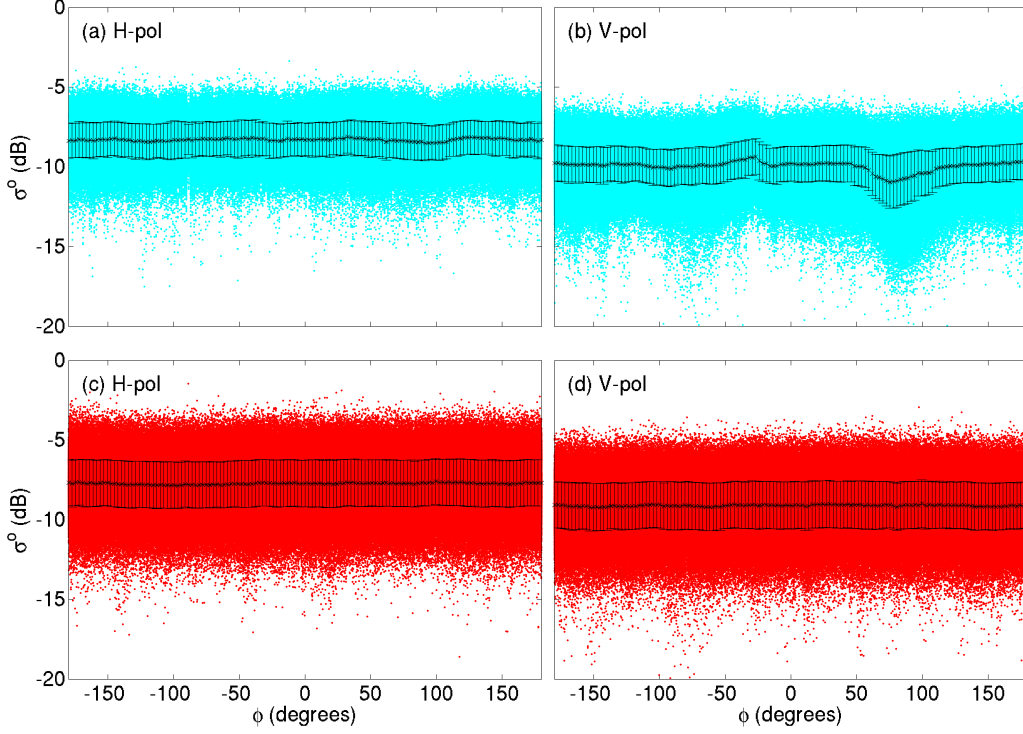


**Figure 4.11:** Scatterplots of  $\theta$  normalized slice  $\sigma^\circ$  versus  $\phi$  for combined pass data of OSCAT (a) H-pol and (b) V-pol, and QuikSCAT (c) H-pol and (d) V-pol.

The model can be represented in matrix multiplicative form as  $\mathbf{s} = P\mathbf{c}$ , where  $\mathbf{s} \in \mathbb{R}^{V \times 1}$ ,  $J \in \mathbb{R}^{V \times (2N+1)}$ , and  $\mathbf{c} \in \mathbb{R}^{(2N+1) \times 1}$  are

$$\mathbf{s} = \begin{bmatrix} \sigma^\circ(\phi_1) & \sigma^\circ(\phi_2) & \dots & \sigma^\circ(\phi_V) \end{bmatrix}^T,$$

$$J = \begin{bmatrix} 1 & \cos(\phi_1) & \sin(\phi_1) & \cos(2\phi_1) & \dots & \sin(4\phi_1) \\ 1 & \cos(\phi_2) & \sin(\phi_2) & \cos(2\phi_2) & \dots & \sin(4\phi_2) \\ \vdots & \vdots & \vdots & \vdots & \vdots & \vdots \\ 1 & \cos(\phi_V) & \sin(\phi_V) & \cos(2\phi_V) & \dots & \sin(4\phi_V) \end{bmatrix},$$

$$\mathbf{c} = \begin{bmatrix} C & D_1 & F_1 & D_2 & \dots & F_4 \end{bmatrix}^T.$$

The model coefficients  $\mathbf{c}$  can be obtained by using the Moore-Penrose pseudo inverse to yield the least-squares solution

$$\mathbf{c} = (J^H J)^{-1} J^H \mathbf{s}. \quad (4.4)$$

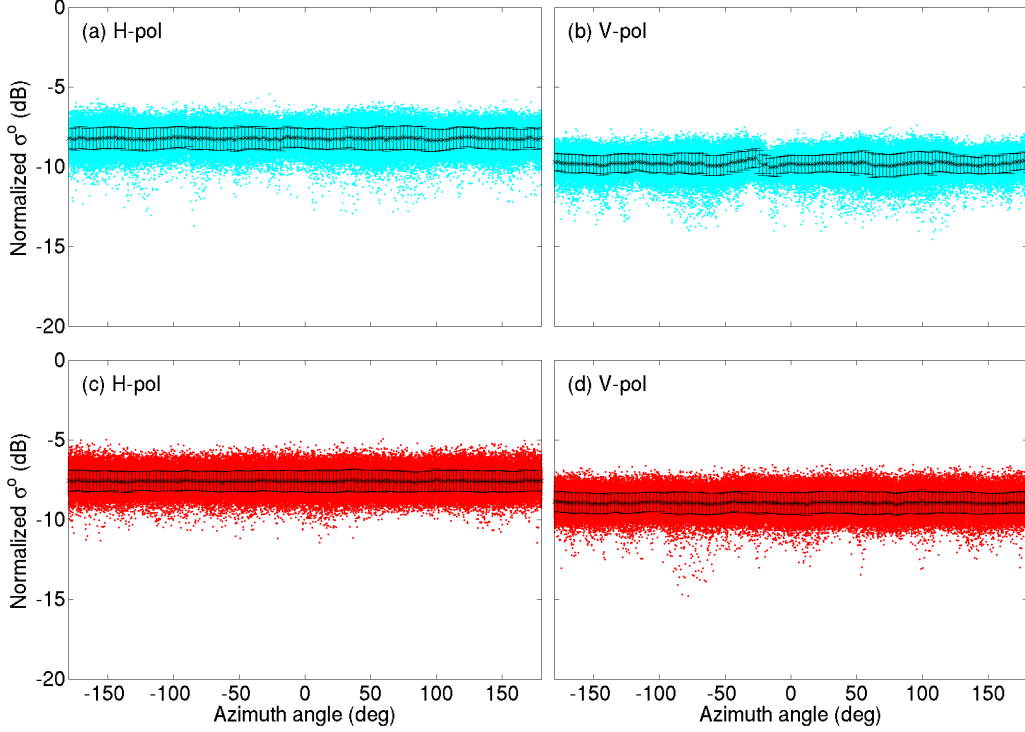


**Figure 4.12:** Scatterplots of  $\phi$  normalized egg  $\sigma^\circ$  versus  $\phi$  for combined pass data of OSCAT (a) H-pol and (b) V-pol, and QuikSCAT (c) H-pol and (d) V-pol.

The azimuthal modulation is then corrected for in the  $i^{\text{th}}$  measurement  $z_i(\phi)$  by normalizing with the model coefficients

$$\sigma_i^\circ = z_i(\phi) - \sum_{k=1}^N [D_k \cos(k\phi_i) + F_k \sin(k\phi_i)]. \quad (4.5)$$

Azimuth angle normalized measurements for ascending and descending combined passes are shown in plots of  $\sigma^\circ$  versus  $\phi$  for eggs and slices in Figures 4.12 and 4.13, respectively. Figures 4.14-4.17 show plots of  $\sigma^\circ$  versus  $\phi$  for ascending and descending egg measurements before and after  $\phi$  normalization. Figures 4.18-4.21 show plots of  $\sigma^\circ$  versus  $\phi$  for ascending and descending slice measurements before and after  $\phi$  normalization.

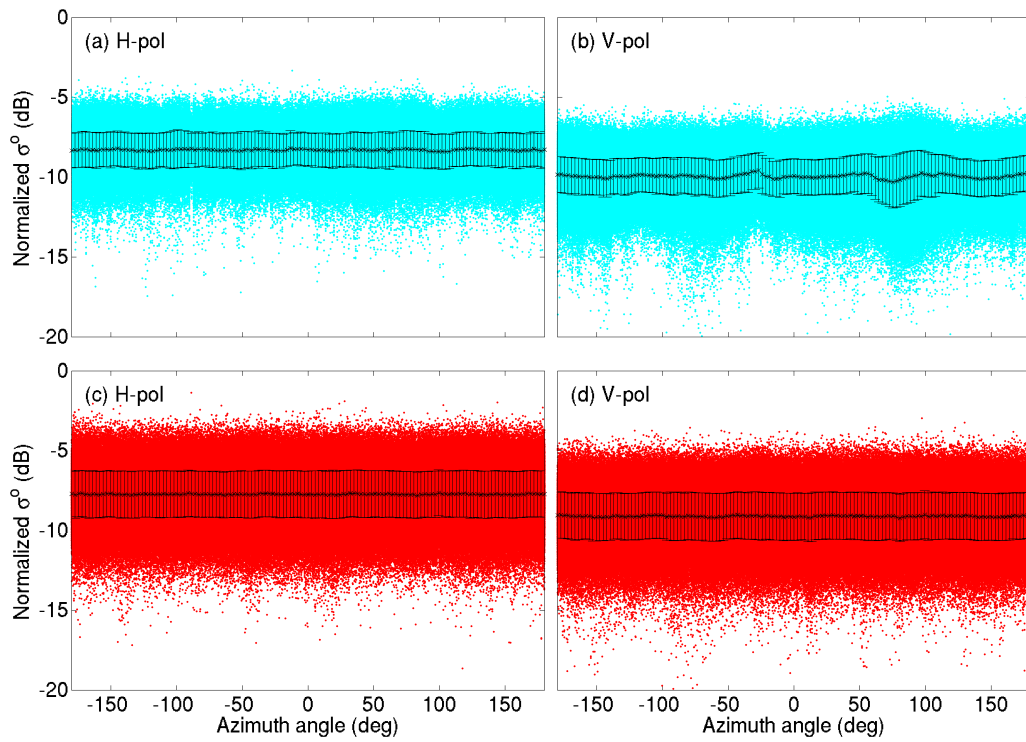


**Figure 4.13:** Scatterplots of  $\theta$  and  $\phi$  normalized slice  $\sigma^{\circ}$  versus  $\phi$  for combined pass data of OSCAT (a) H-pol and (b) V-pol, and QuikSCAT (c) H-pol and (d) V-pol.

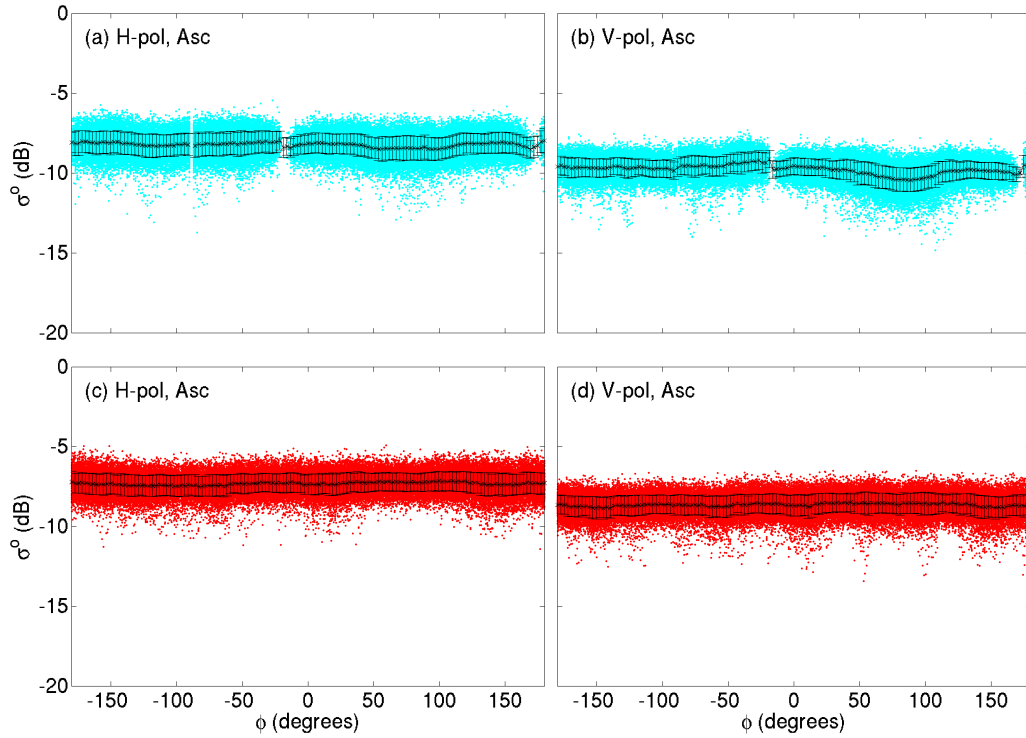


**Figure 4.14:** Scatterplots of egg  $\sigma^\circ$  versus  $\phi$  for ascending pass data of OSCAT (a) H-pol and (b) V-pol, and QuikSCAT (c) H-pol and (d) V-pol.

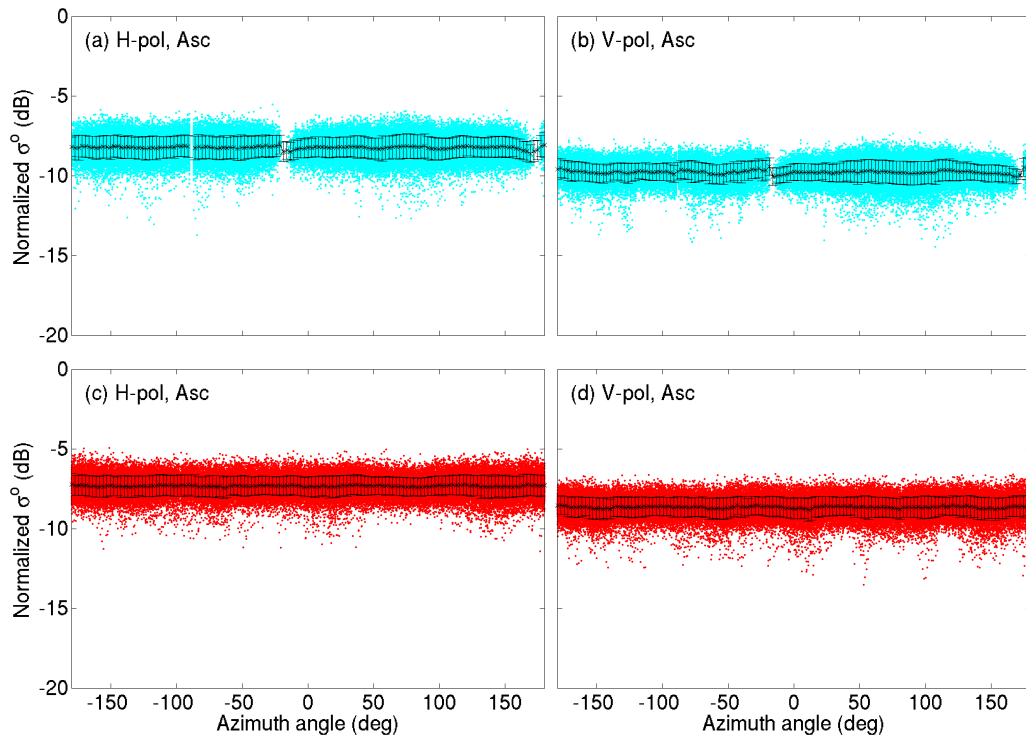


**Figure 4.15:** Scatterplots of  $\phi$  normalized egg  $\sigma^\circ$  versus  $\phi$  for ascending pass data of OSCAT (a) H-pol and (b) V-pol, and QuikSCAT (c) H-pol and (d) V-pol.

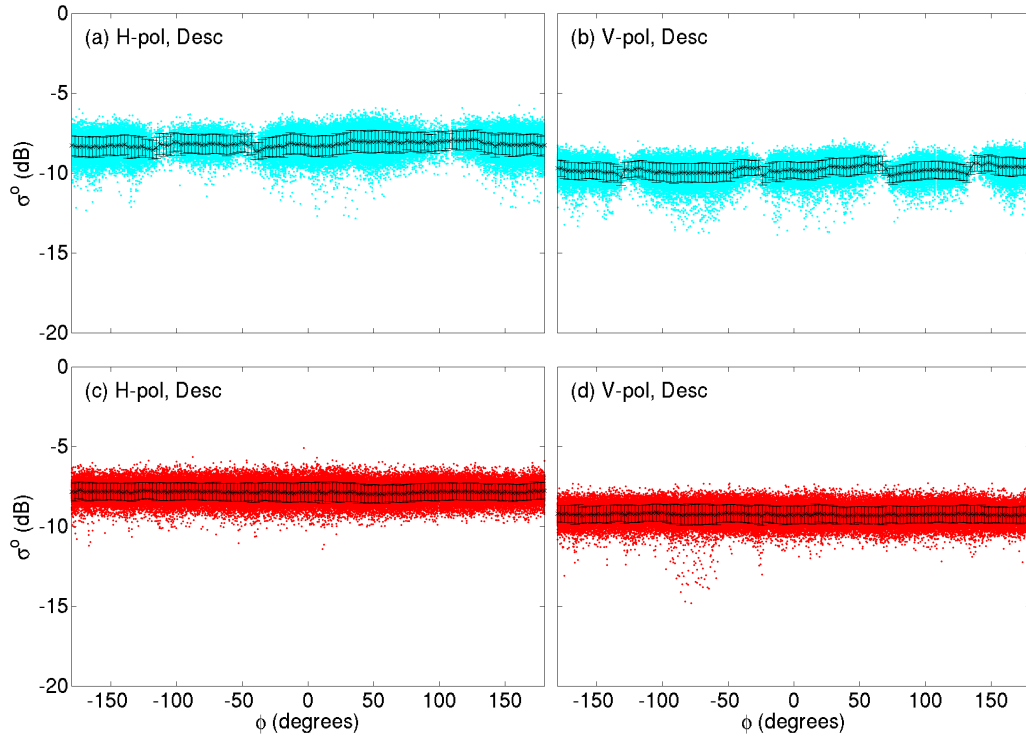


**Figure 4.16:** Scatterplots of egg  $\sigma^\circ$  versus  $\phi$  for descending pass data of OSCAT (a) H-pol and (b) V-pol, and QuikSCAT (c) H-pol and (d) V-pol.

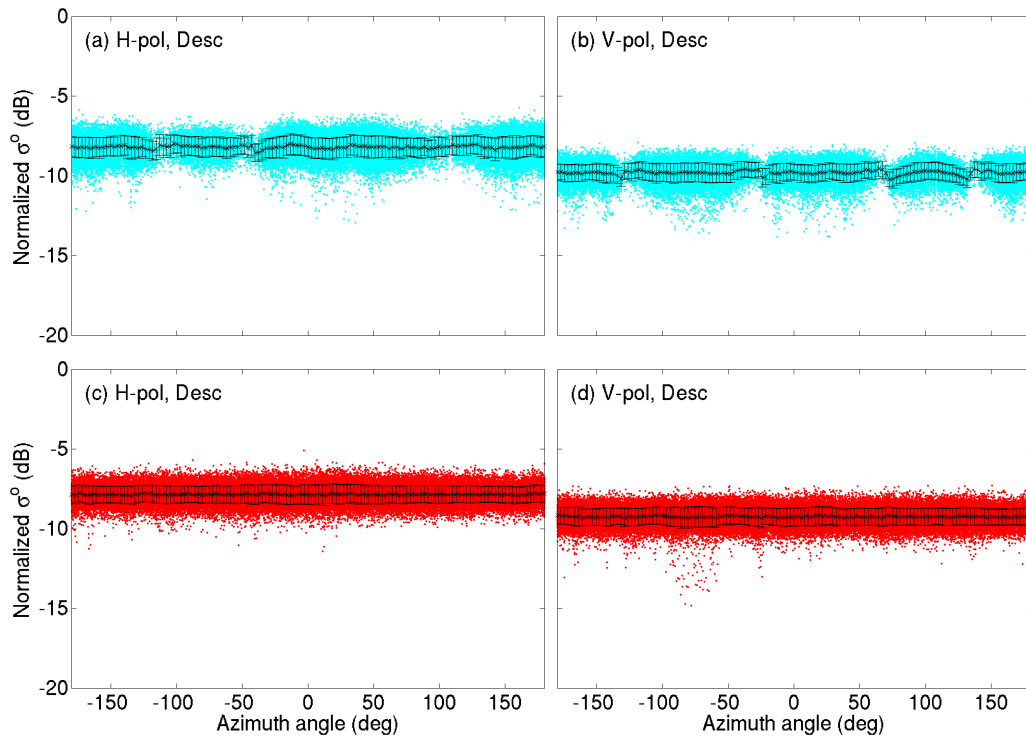


**Figure 4.17:** Scatterplots of  $\phi$  normalized egg  $\sigma^\circ$  versus  $\phi$  for descending pass data of OSCAT (a) H-pol and (b) V-pol, and QuikSCAT (c) H-pol and (d) V-pol.

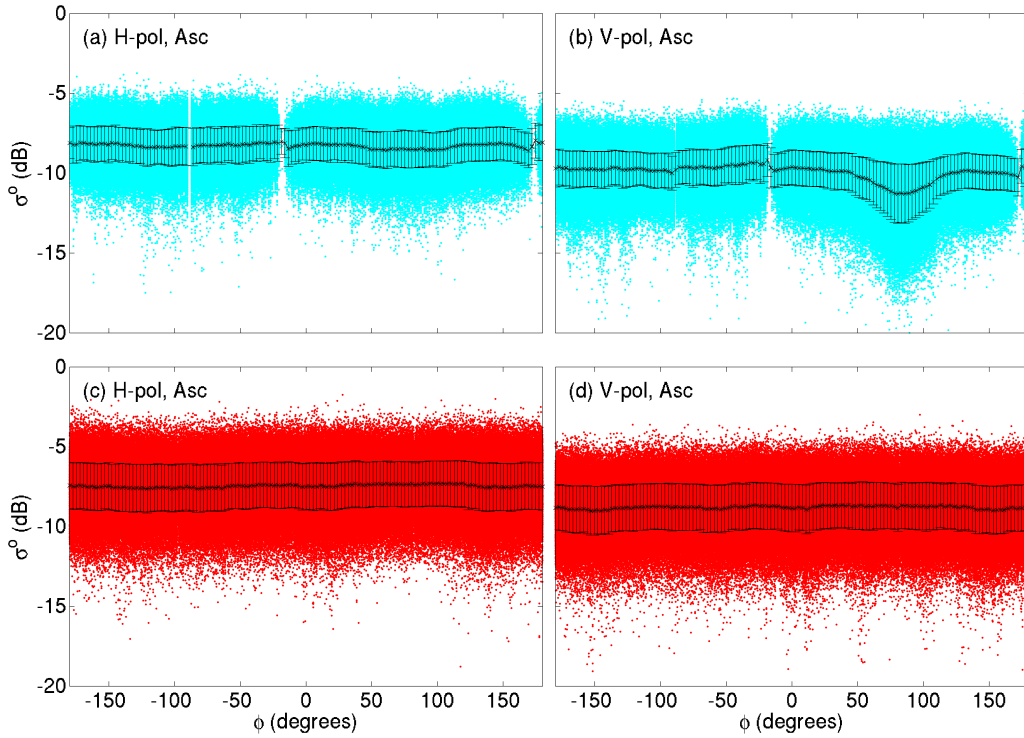


**Figure 4.18:** Scatterplots of  $\theta$  normalized slice  $\sigma^\circ$  versus  $\phi$  for ascending pass data of OSCAT (a) H-pol and (b) V-pol, and QuikSCAT (c) H-pol and (d) V-pol.

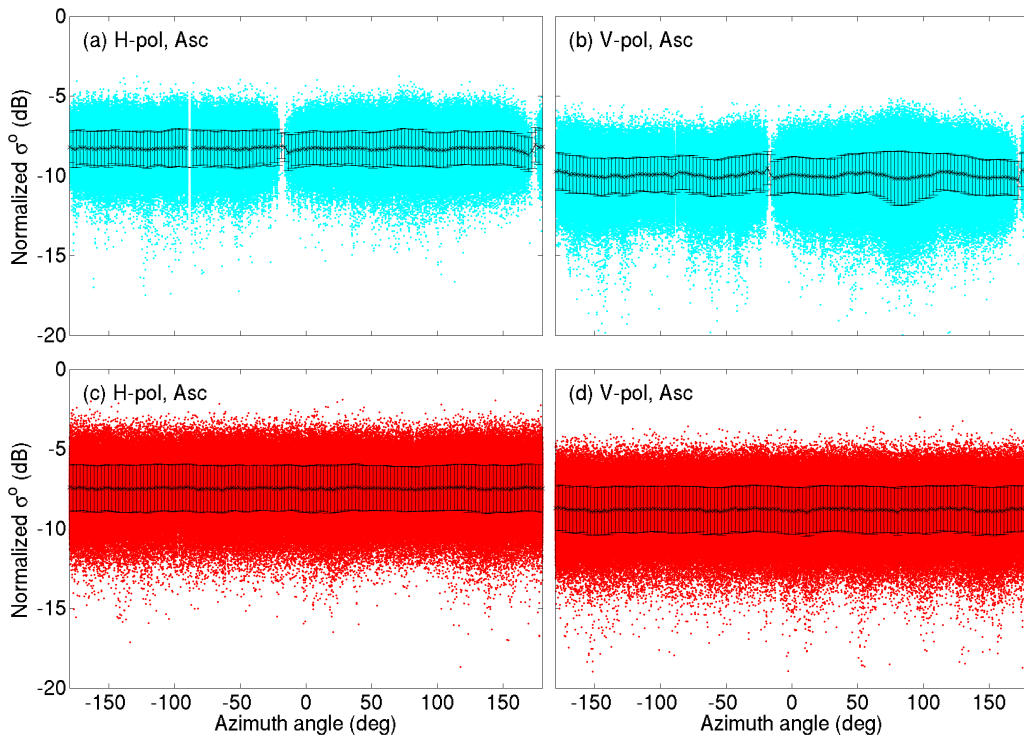


**Figure 4.19:** Scatterplots of  $\theta$  and  $\phi$  normalized slice  $\sigma^\circ$  versus  $\phi$  for ascending pass data of OSCAT (a) H-pol and (b) V-pol, and QuikSCAT (c) H-pol and (d) V-pol.

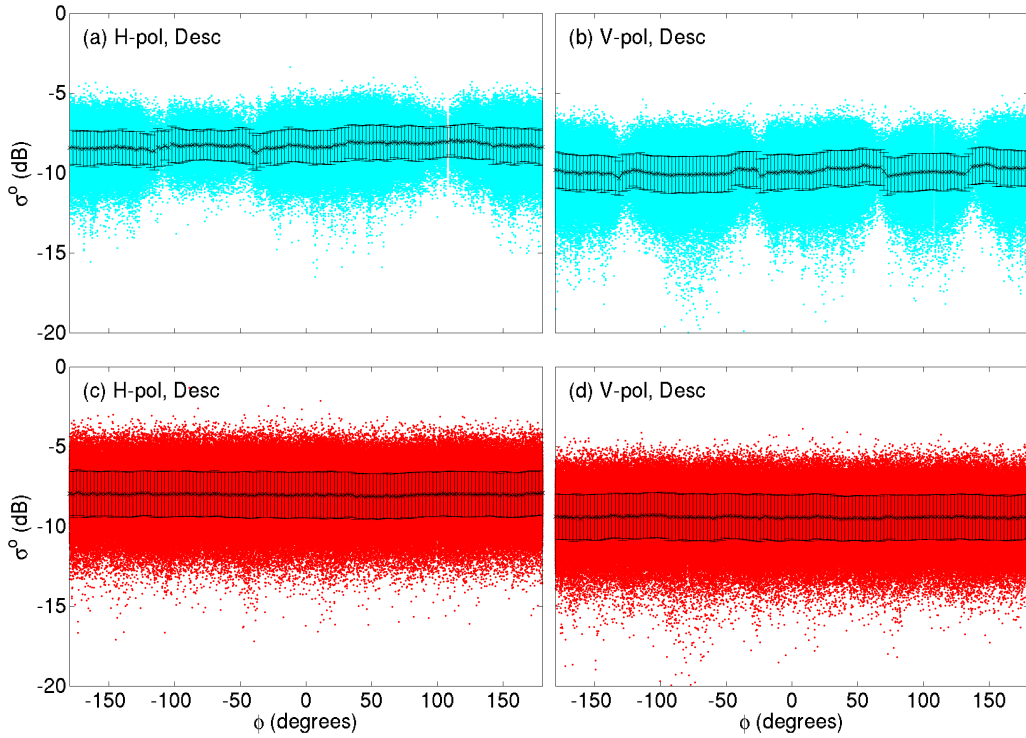


**Figure 4.20:** Scatterplots of  $\theta$  normalized slice  $\sigma^\circ$  versus  $\phi$  for descending pass data of OSCAT (a) H-pol and (b) V-pol, and QuikSCAT (c) H-pol and (d) V-pol.

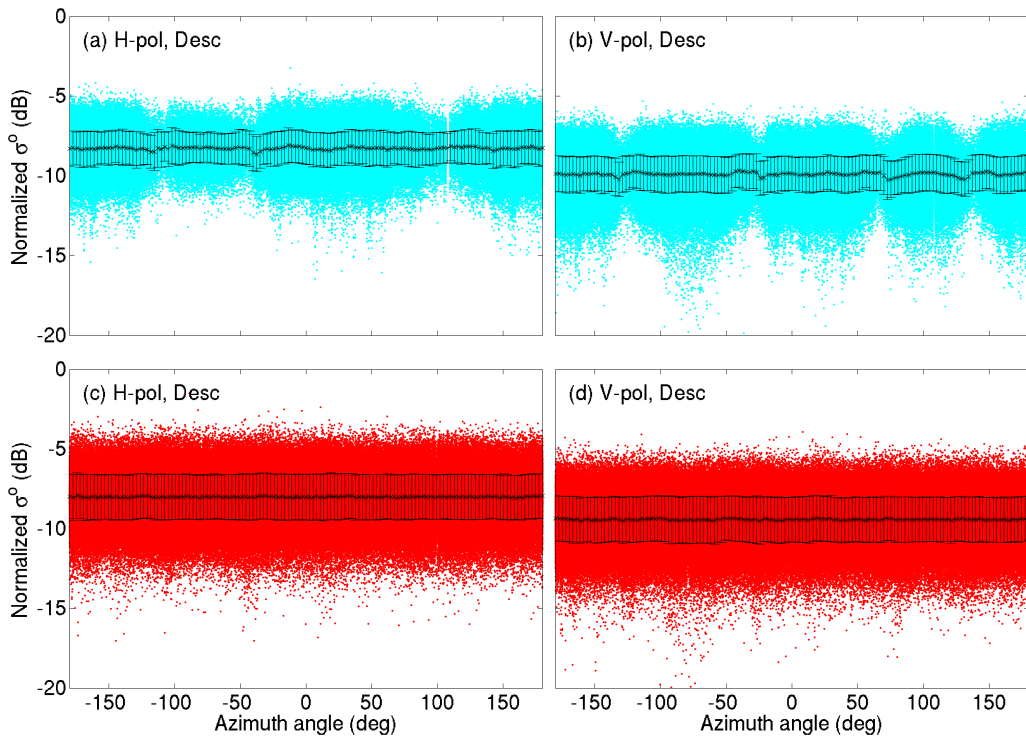


**Figure 4.21:** Scatterplots of  $\theta$  and  $\phi$  normalized slice  $\sigma^\circ$  versus  $\phi$  for descending pass data of OSCAT (a) H-pol and (b) V-pol, and QuikSCAT (c) H-pol and (d) V-pol.

**Table 4.1:** Relative calibration factors  $\beta_h$  and  $\beta_v$  in dB for  $\sigma^\circ$  of OSCAT egg and slice measurements for ascending, descending, and combined passes.

Type	Satellite Pass	$\beta_h$	$\beta_v$
Egg	Ascending	0.89	1.11
	Descending	0.34	0.55
	Combined	0.64	0.85
Slice	Ascending	0.81	1.16
	Descending	0.27	0.47
	Combined	0.57	0.84

### 4.2.3 Data Analysis

Having normalized the unwanted dependencies in the  $\sigma^\circ$  response, the measurement statistics are compared between instruments and relative calibration factors  $\beta_h$  and  $\beta_v$  are determined for the H- and V-pol measurements, respectively. First, the mean  $\mu_{\text{pol}}$  and standard deviation  $\varsigma_{\text{pol}}$  (where  $\text{pol} = h$  or  $v$  as appropriate) are calculated for each beam with ascending, descending, and combined pass measurements of each instrument. Then, the relative calibration factor  $\beta_{\text{pol}}$  is determined for each beam with ascending, descending, and combined pass measurements separately by

$$\beta_{\text{pol}} = \mu_{\text{pol,Q}} - \mu_{\text{pol,O}}, \quad (4.6)$$

where  $\mu_{\text{pol,Q}}$  and  $\mu_{\text{pol,O}}$  are the mean  $\sigma^\circ$  values of a given polarization of QuikSCAT and OSCAT, respectively. Measurement distributions  $f_{\sigma^\circ}(\sigma^\circ)$  are also generated from normalized histograms of the measurements. Figure 4.22 shows  $f_{\sigma^\circ}(\sigma^\circ)$  for egg measurements with corresponding values of  $\mu_{\text{pol}}$  and  $\varsigma_{\text{pol}}$ , and Figure 4.23 shows  $f_{\sigma^\circ}(\sigma^\circ)$  for slice measurements with corresponding values of  $\mu_{\text{pol}}$  and  $\varsigma_{\text{pol}}$ . By examination of the calculated values of  $\beta_h$  and  $\beta_v$  given in Table 4.1, it is evident that there is a strong dependency on LTD due to the ascending and descending node times of the scatterometer.

To investigate LTD effects further, mean values of normalized egg  $\sigma^\circ$  measurements are plotted as a function of LTD in Figure 4.24. At 6:00 a.m., corresponding to the ascending pass of QuikSCAT, there is increase in mean  $\sigma^\circ$  response of approximately 0.5 dB for H-

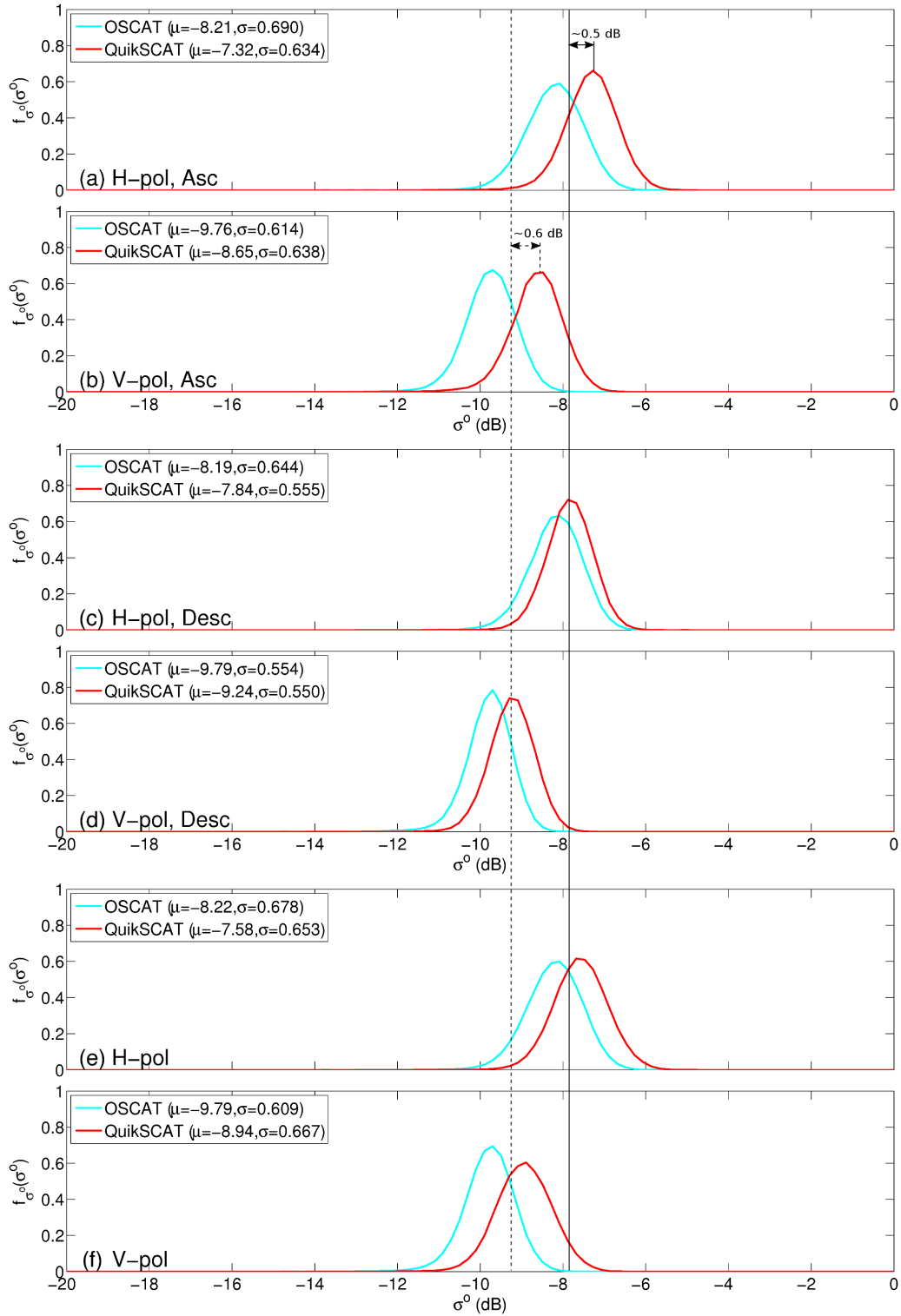


**Figure 4.22:** Plots of measurement distribution  $f_{\sigma^\circ}(\sigma^\circ)$  for normalized H- and V-pol egg measurements of the (a)-(b) ascending, (c)-(d) descending, and (e)-(f) combined passes.

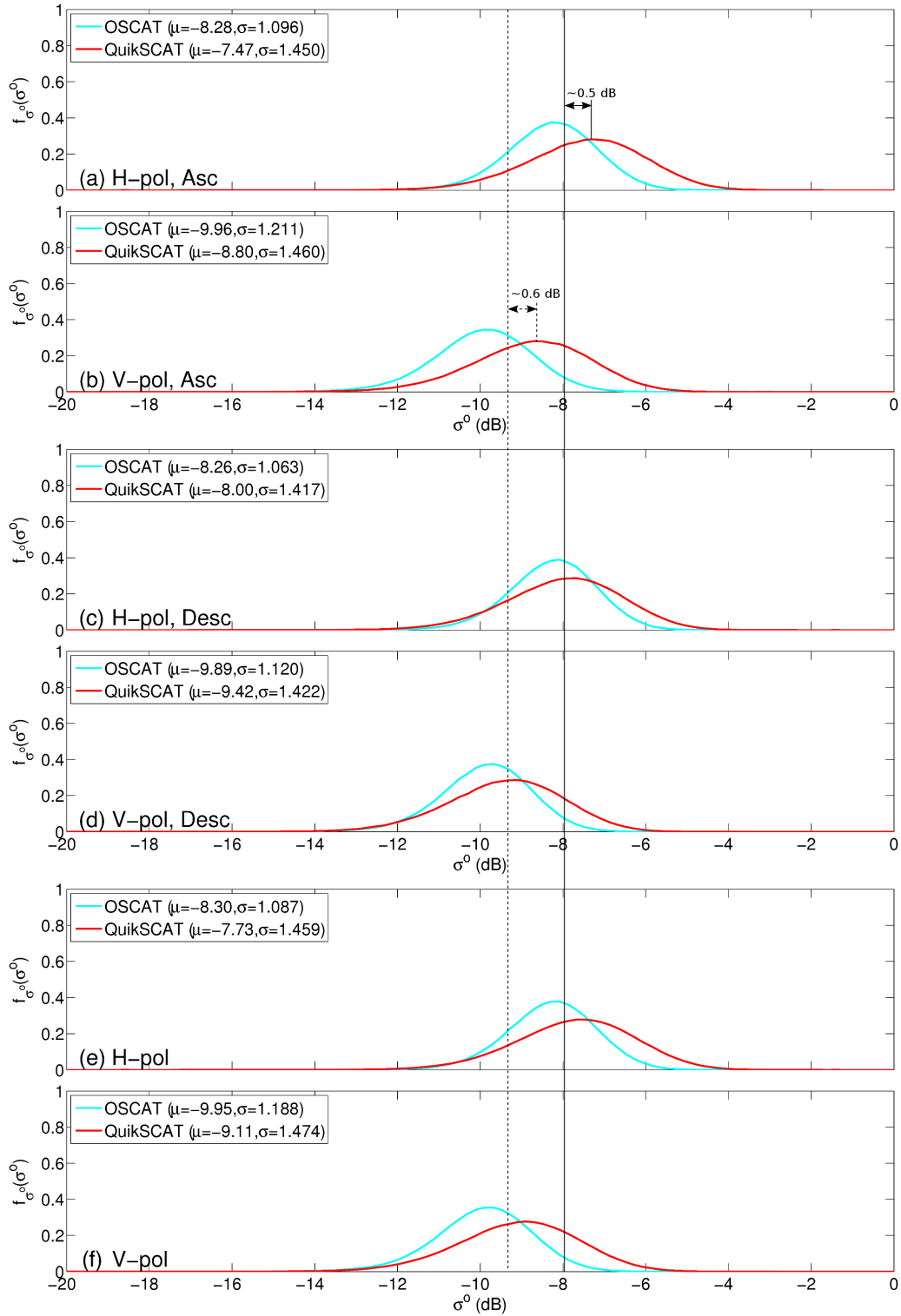


**Figure 4.23:** Measurement distributions  $f_{\sigma^\circ}(\sigma^\circ)$  for normalized H- and V-pol slice measurements of the (a)-(b) ascending, (c)-(d) descending, and (e)-(f) combined passes.

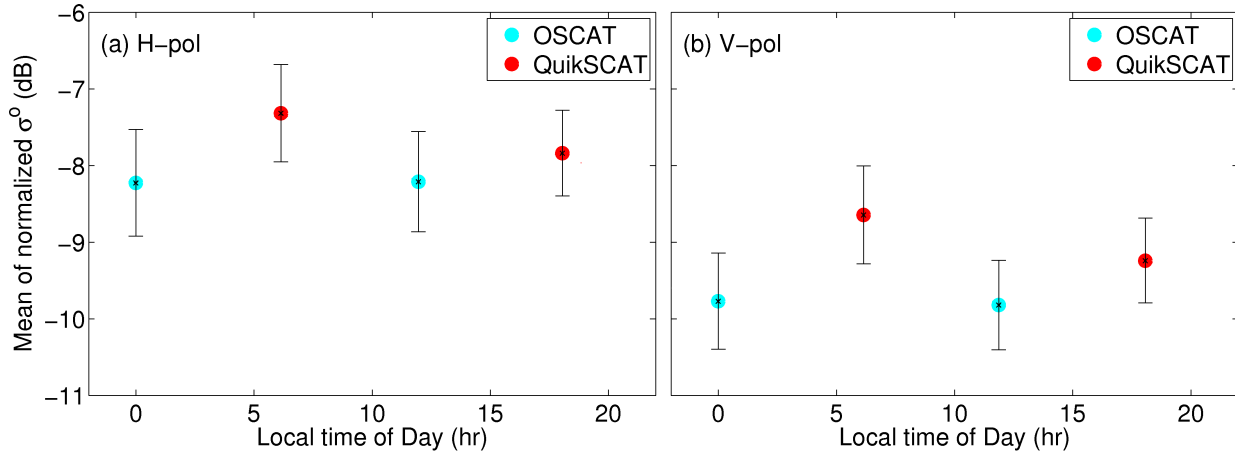


**Figure 4.24:** Mean values of normalized egg  $\sigma^\circ$  from OSCAT and QuikSCAT versus local time of day.

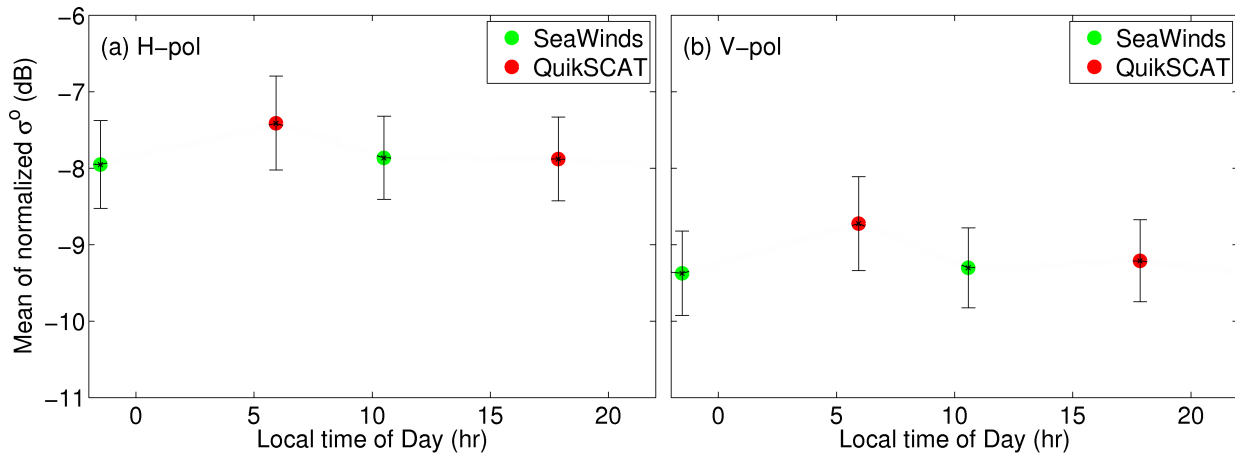


**Figure 4.25:** Mean values of normalized egg  $\sigma^\circ$  from SeaWinds and QuikSCAT versus local time of day.

pol measurements and 0.6 dB for V-pol measurements of QuikSCAT with respect to the descending pass values, as depicted in Figures 4.22 and 4.23. At either observation LTD of OSCAT there does not appear to be any significant difference in mean  $\sigma^\circ$  response in H-pol or V-pol measurements. The net difference in mean  $\sigma^\circ$  response for observation LTD of OSCAT and QuikSCAT appears to be due to observation incidence angle offsets between their corresponding beams, and not fluctuation in  $\sigma^\circ$  due to LTD.

To verify that the net difference in mean  $\sigma^\circ$  between OSCAT and QuikSCAT is caused by differences in respective observation incidence angle geometry, the mean response of nor-

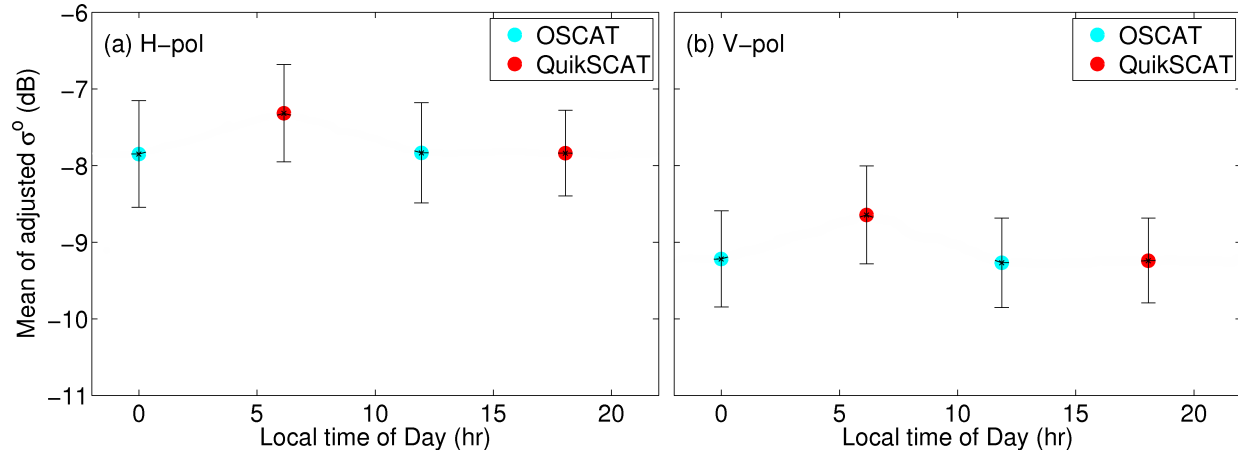


**Figure 4.26:** Mean values of normalized egg  $\sigma^\circ$  from OSCAT and QuikSCAT versus local time of day after adjustment of OSCAT data by the calibration factors.

malized egg  $\sigma^\circ$  measurements of SeaWinds over the selected area is plotted as a function of LTD along with QuikSCAT in Figure 4.25 for JD 280-297 of 2003. Ambiguities associated with observation incidence angle geometries are minimized because the observation incidence angle geometry of SeaWinds and QuikSCAT is identical and the two instruments are calibrated to within  $\sim \pm 0.05$  dB [27]. The mean  $\sigma^\circ$  response for observation LTD of SeaWinds is consistent with the descending pass of QuikSCAT at 6:00 p.m. This reinforces conclusions drawn in prior studies that there is diurnal fluctuation in  $\sigma^\circ$  over the Amazon in the early morning. To minimize biases, descending pass-based relative calibration factors  $\beta_h = 0.34$  and  $\beta_v = 0.55$  for egg measurements, and  $\beta_h = 0.27$  and  $\beta_v = 0.47$  for slice measurements from Table 4.1 are recommended. Figure 4.26 shows the  $\sigma^\circ$  versus LTD response for OSCAT and QuikSCAT egg measurements after adjusting OSCAT data by the calibration factors. Corresponding plots of slice measurements look similar.

As an insight into the possible calibration approach employed by ISRO, the response of normalized slice  $\sigma^\circ$  is analyzed collectively across all beams versus  $\theta$  for combined pass data in Figure 4.27 and descending pass data in Figure 4.28. The solid line in the plots represents the least-squares fit of the model in Eq. (2.3) about the nominal incidence angle  $\Theta = 46$  of the inner beam of QuikSCAT. Though there is a polarization difference between the inner and outer beams, because the  $\sigma^\circ$  response over Amazon is assumed to be mostly polarization independent, the plots provide a good sense of the combined incidence angle

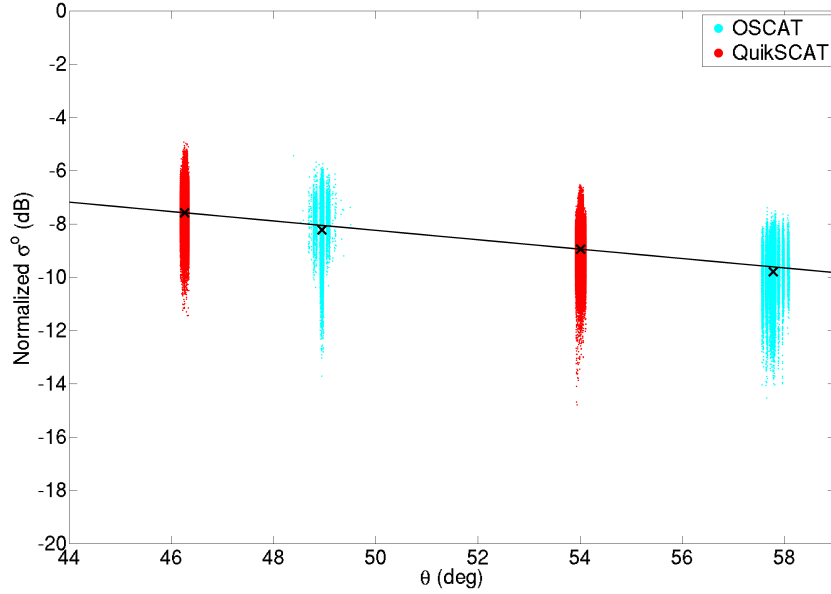


**Figure 4.27:** Scatterplot of OSCAT and QuikSCAT normalized slice  $\sigma^\circ$  versus  $\theta$  for combined pass data of both beams. “x” marks the mean response of each beam.

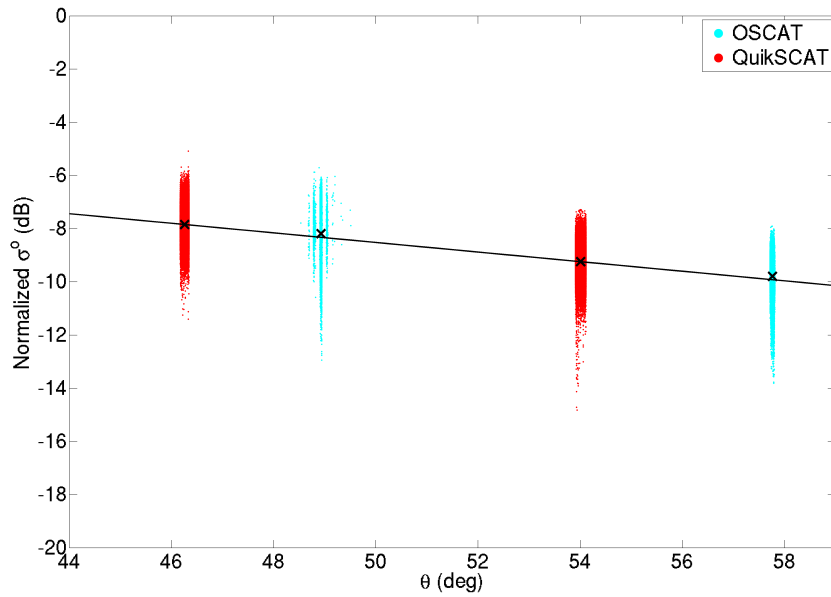


**Figure 4.28:** Scatterplot of OSCAT and QuikSCAT normalized slice  $\sigma^\circ$  versus  $\theta$  for descending pass data of both beams. “x” marks the mean response of each beam.

response of each instrument. The mean response of normalized OSCAT  $\sigma^\circ$  for descending pass data more closely matches the best fit line than combined pass data, suggesting an effective internal calibration procedure was performed by ISRO.

### 4.3 SIR Data Calibration Procedure

Combining overlapping measurements from multiple passes to solve for the true surface  $\sigma^\circ$  image, as is done in SIR processing, averages together effects of  $\phi$  and  $\theta$  in OSCAT and QuikSCAT  $\sigma^\circ$  response. As a result, the influence of  $\phi$  and  $\theta$  on  $\sigma^\circ$  cannot be estimated based on OSCAT and QuikSCAT SIR imagery. Therefore, the  $\sigma^\circ$  normalization procedure performed for raw  $\sigma^\circ$  data is not performed for SIR image  $\sigma^\circ$  data. This reduces relative cross-calibration of SIR image  $\sigma^\circ$  data to analysis of the measurement statistics to obtain relative calibration factors, as was done for the normalized raw  $\sigma^\circ$  data. Outcomes are verified by performing the procedure over the selected area of Greenland, shown in Figure 4.5, in addition to the selected area of the Amazon basin used in the previous section.

The analysis is performed using  $\mathcal{A}_h$ - and  $\mathcal{A}_v$ -SIR image data for eggs and slices of OSCAT for JD 355 of 2011 through JD 33 of 2012, and of QuikSCAT for JD 355 of 2008 through JD 33 of 2009, where  $\sigma^\circ$  measurements correspond to individual pixel values. A longer time series of data is necessary for SIR image  $\sigma^\circ$  data because of averaging effects of the SIR algorithm. Having shown in the previous section that consideration of diurnal fluctuation in  $\sigma^\circ$  is mandatory for achieving accurate results with relative calibration techniques using natural land targets, only SIR images processed based on LTD are used. From the discussion in Chapter 3, LTD SIR images of Greenland correspond to evening (Eve) and midday (Mid) for OSCAT, and evening (Eve) and morning (Morn) for QuikSCAT.

#### 4.3.1 Data Analysis

Calculating measurement mean  $\mu_{\text{pol}}$ , standard deviation  $\varsigma_{\text{pol}}$ , and distribution  $f_{\sigma^\circ}(\sigma^\circ)$  as was done in the previous section, SIR relative calibration factors  $\beta_h$  and  $\beta_v$  are determined for the H-pol and V-pol measurements, respectively. Realizations of egg measurement distribution, mean, and standard deviation are shown in Figure 4.29 for the Amazon and Figure 4.30 for Greenland. Realizations of slice measurement distribution, mean, and standard deviation are shown in Figure 4.31 for the Amazon and Figure 4.32 for Greenland. Computed values of  $\beta_h$  and  $\beta_v$  are given in Table 4.2.

The values of  $\beta_h$  and  $\beta_v$  given in Table 4.2 appear to be inconsistent with the  $\beta_h$  and  $\beta_v$  values calculated for raw measurements in the previous section. Only egg measurements

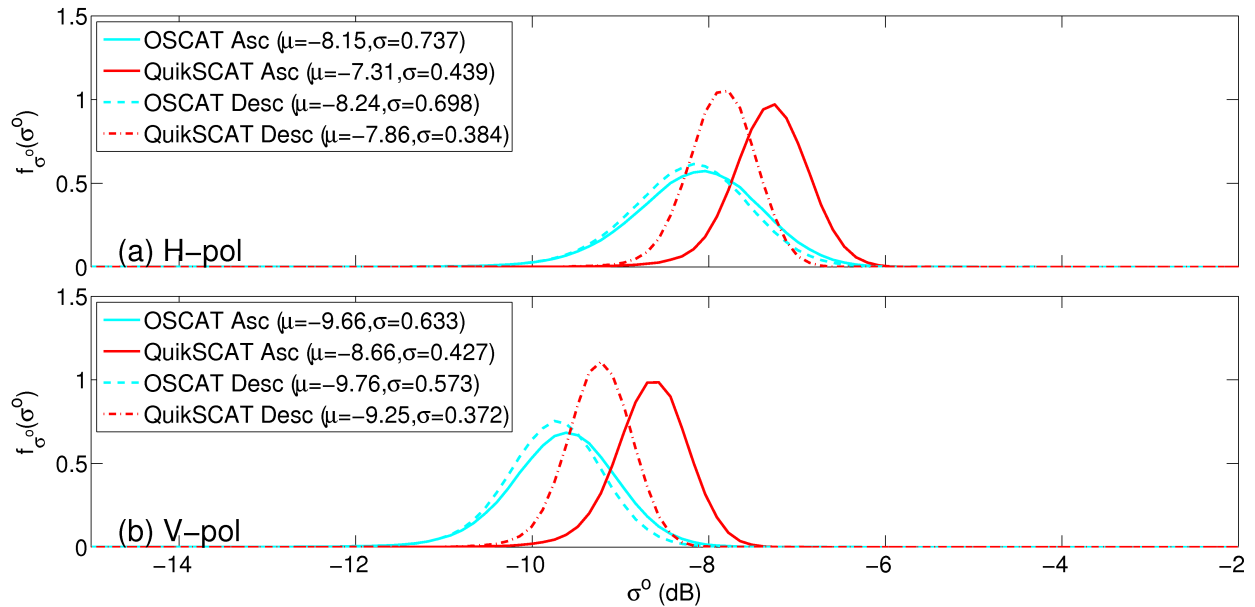


**Figure 4.29:** Measurement distributions  $f_{\sigma^\circ}(\sigma^\circ)$  for (a) H-pol and (b) V-pol egg SIR image  $\sigma^\circ$  measurements for corresponding passes of each instrument over the Amazon region.

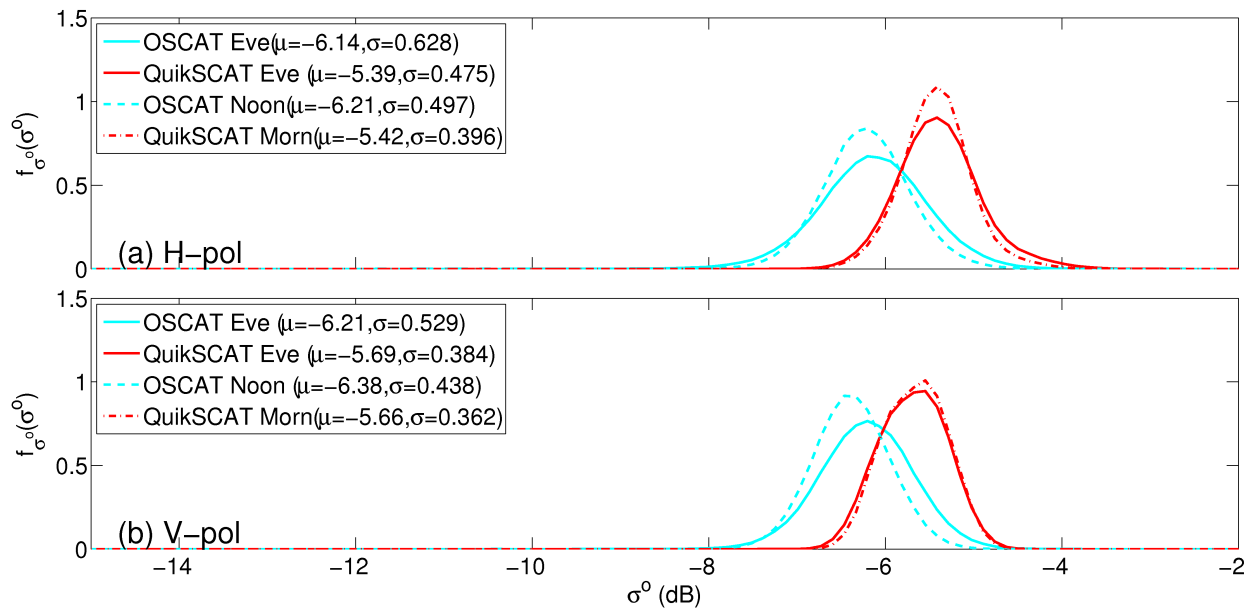


**Figure 4.30:** Measurement distributions  $f_{\sigma^\circ}(\sigma^\circ)$  for (a) H-pol and (b) V-pol egg SIR image  $\sigma^\circ$  measurements for the corresponding passes of each instrument over the Greenland region.

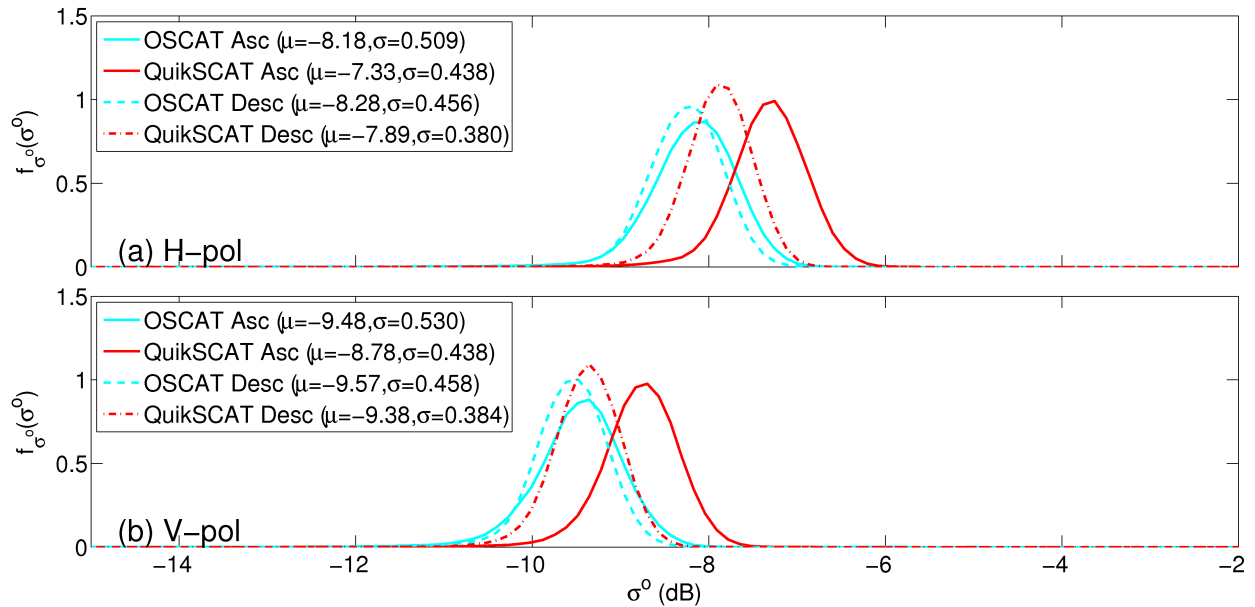


**Figure 4.31:** Measurement distributions  $f_{\sigma^\circ}(\sigma^\circ)$  for (a) H-pol and (b) V-pol slice SIR image  $\sigma^\circ$  measurements for corresponding passes of each instrument over the Amazon region.

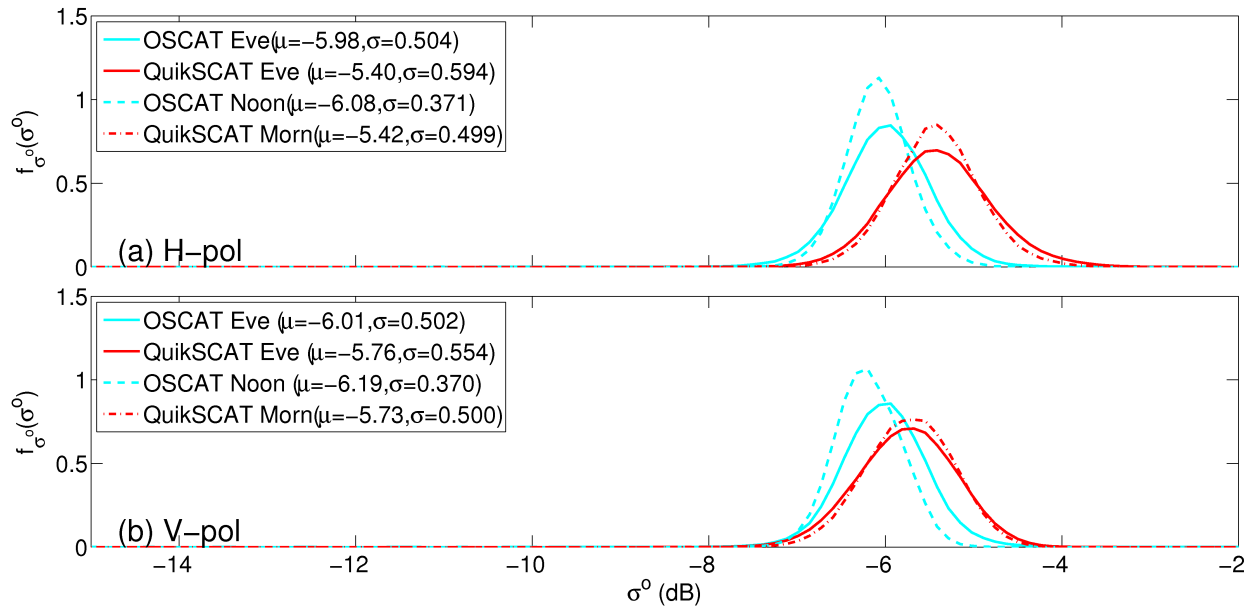


**Figure 4.32:** Measurement distributions  $f_{\sigma^\circ}(\sigma^\circ)$  for (a) H-pol and (b) V-pol slice SIR image  $\sigma^\circ$  measurements for the corresponding passes of each instrument over the Greenland region.

**Table 4.2:** Relative calibration factors  $\beta_h$  and  $\beta_v$  in dB for  $\sigma^\circ$  of OSCAT egg and slice SIR image data for the Amazon and Greenland.

Type	Region	Satellite Pass	$\beta_h$	$\beta_v$
Egg	Amazon	Ascending	0.84	1.00
		Descending	0.38	0.51
	Greenland	Eve	0.75	0.53
		Mid/Morn	0.79	0.72
Slice	Amazon	Ascending	0.85	0.71
		Descending	0.39	0.20
	Greenland	Eve	0.59	0.25
		Mid/Morn	0.66	0.46

over the Amazon produce results entirely consistent with raw measurements. Results for slice measurements over the Amazon are consistent for H-pol, but exhibit about  $\sim -0.3$  dB bias for V-pol, evident in the difference between  $\beta_v$  values for slice and egg measurements from Table 4.2. The V-pol slice bias is an artifact of SIR processing for OSCAT slices. Because there is a  $\theta$  dependence in slice measurements of scanning dual-pencil beam scatterometers, beginning with QuikSCAT, the  $\theta$  dependence of slice measurements have been traditionally corrected during SIR processing by normalizing about the nominal incidence angle  $\Theta$  per beam with  $\mathcal{B} = -0.14$  dB/deg. The value used for  $\mathcal{B}$  is empirically derived from NSCAT data as the nominal linear  $\theta$  dependence for Ku-band scatterometer measurements. For OSCAT SIR processing, raw  $\sigma^\circ$  measurements are currently normalized about  $\Theta = 56^\circ$ . Since the mean incidence angle of V-pol measurements is approximately  $\sim 57.7^\circ$ , correcting about  $\Theta = 56^\circ$  results in a net positive bias in  $\sigma^\circ$  of OSCAT SIR imagery of about  $\sim 0.24$  dB. By accounting for this bias, the results of  $\beta_v$  for slice SIR image data remains consistent with the results obtained with raw slice  $\sigma^\circ$  data in the previous section. In the future, perhaps  $\Theta = 57.7^\circ$  can be used in normalization of OSCAT V-pol slice  $\sigma^\circ$  measurements during SIR processing to eliminate this bias in future  $\mathcal{A}_v$ -SIR images of OSCAT.

Evening measurements over the Greenland region appear to give results consistent with V-pol descending measurements over the Amazon, while noon and morning SIR image data of OSCAT and QuikSCAT, respectively, tend to disagree by about  $\sim 0.2$  dB. From examination of Figures 4.30 and 4.32, the disagreement is caused by decrease in mean  $\sigma^\circ$

during the midday pass of OSCAT. This observed decrease in mean  $\sigma^\circ$  during the midday pass may suggest a diurnal cycle in  $\sigma^\circ$  over the Greenland region. It might be possible that the observed difference are due to observation geometry differences between the evening and midday passes of OSCAT over the region. The observed difference is worthy of further investigation by future researchers. For this analysis, it suffices to note that for this study only SIR images corresponding to evening passes of OSCAT and QuikSCAT are suitable for relative cross-calibration efforts between the two instruments.

As for the results of H-pol measurements over the Greenland region, there is no apparent consistency with results over the Amazon. This may be due to poor sampling in creation of the SIR images, as demonstrated in a time series of OSCAT evening  $\mathcal{A}_h$ -SIR images shown in Figure 4.33. The poor sampling results in missing pixel data in the SIR images, which correspond to black pixel values over the Greenland ice sheet. The huge gaps of missing data, exemplified in the SIR image for JD 5 from the time series, are due to data drop out during the data downlink over Svalbard for OSCAT. The missing data consistent around the perimeter of the Greenland ice-sheet is related to poor quality  $\sigma^\circ$  measurements. This means that the  $\sigma^\circ$  values in neighboring pixels may be significantly more noisy due to poor spatial averaging. The results obtained for H-pol over Greenland are therefore considered to be invalid. As a consequence, Greenland is considered to not be a good relative calibration site for OSCAT.

As relative calibration factors that can be universally applied to the current dataset of OSCAT egg and slice SIR images, values of  $\beta_{\text{pol}}$  computed for descending pass data over the Amazon region are recommended. Specifically, the values are  $\beta_h = 0.38$  and  $\beta_v = 0.51$  for egg SIR image data, and  $\beta_h = 0.39$  and  $\beta_v = 0.20$  for slice SIR image data.

#### 4.4 Summary

Relative cross-calibration of OSCAT and QuikSCAT is necessary to determine the suitability of the OSCAT instrument for extending the SCP data time series. Based on the calibration procedure performed in this chapter, the most recent OSCAT L1B data exhibits a  $\sigma^\circ$  response sufficiently stable for use in the SCP database. To maintain consistency in the SCP data time series, relative calibration factors empirically derived in this chapter can

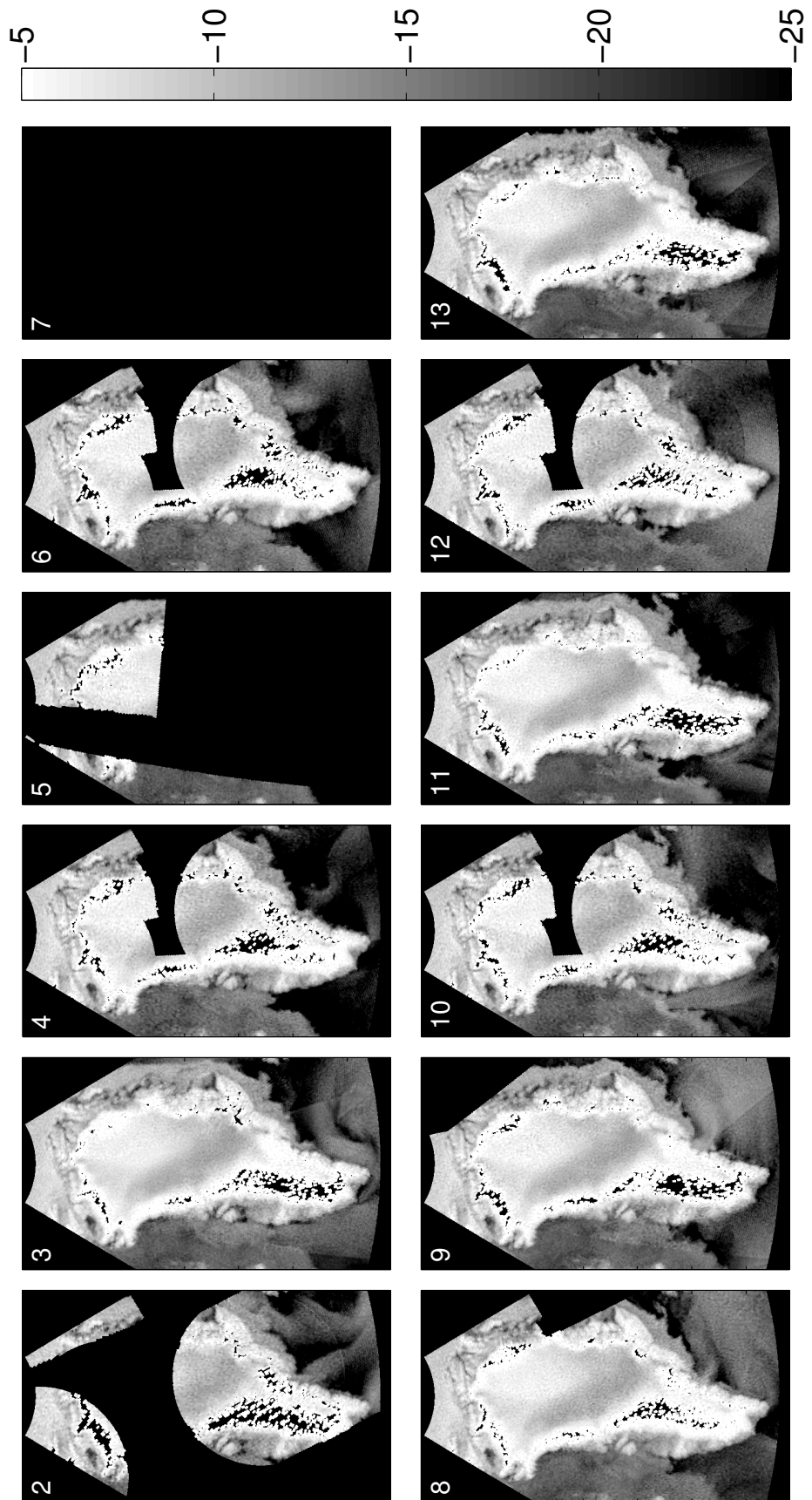


Figure 4.33: Time series of  $\mathcal{A}_h$ -SIR images of Greenland during the evening. The time series covers JD 2-13 of 2012.

be applied to OSCAT data to normalize its  $\sigma^\circ$  response to the nominal incidence angles of the inner and outer beams of QuikSCAT/SeaWinds. For simplification of SIR image creation, calibration factors applicable to SIR images created with unadjusted L1B data are available, in addition to calibration factors for raw measurements. For future calibration efforts with OSCAT, it has been determined that Greenland is not a suitable calibration site for techniques using homogeneous extended-area natural land targets.

## Chapter 5

### Estimating the OSCAT Spatial Response Function Using Island Targets

Many of the algorithms used in creation of SCP products have increased the utility of scatterometer data by using knowledge of the scatterometer spatial response function (SRF). Having limited knowledge of the OSCAT SRF, a method of estimating it for use in creating OSCAT SCP products is developed in this chapter. The estimation method uses scatterometer measurements over islands to invert the radar equation. A mathematical model is developed that reduces the solution to rank-reduced least-squares estimation. The procedure is facilitated by introducing a simplified model of the scattering characteristics of an island target. Because the method relies heavily upon the size of island and number of singular values used in rank-reduced least-squares, a simulation procedure is developed that verifies the efficacy of the method, while also providing optimum choice of island size and number of singular values. By applying the estimation method to OSCAT, estimates of the OSCAT SRF for egg and slice measurements of both beams are obtained. The utility of OSCAT SRF estimates is demonstrated through the construction of an egg  $\mathcal{A}_h$ -SIR image over the Amazon using an estimate of the OSCAT H-pol egg SRF.

The chapter begins with the derivation of the OSCAT SRF in Section 5.1. The estimation problem is set up in Section 5.2 and mathematical models are proposed to obtain a solution. The geographic sampling region is discussed in Section 5.3, including a description of the simplified model of the island scattering characteristics. A simulation process designed to test the efficacy of the proposed estimation method and optimize for island size and number of singular values is discussed in Section 5.4. Estimates of the OSCAT SRF are presented in Section 5.5, followed by a summary in Section 5.6.

## 5.1 The Spatial Response Function

The power  $P_r$  received by OSCAT can be decomposed into a component caused by backscattered signal  $P_b$  from the target and a noise component  $P_n$  so

$$P_r = P_b + P_n,$$

where  $P_r$  is the total received power and  $P_n$  encapsulates noise caused by instrument electronics and atmospheric effects. The power reflected from the surface of the Earth is

$$P_b = \frac{P_t \lambda^2}{(4\pi)^3} \int_A \frac{Q^2 \sigma^\circ}{r^4} dA, \quad (5.1)$$

where  $P_t$  is the transmit power,  $\lambda$  is the wavelength,  $Q$  is the antenna gain,  $\sigma^\circ$  is the true normalized radar backscatter of the Earth's surface,  $r$  is the slant range, and  $A$  denotes the area illuminated by the antenna [35]. Assuming that the radar backscatter is constant over the illuminated area of the target, a signal-only weighted spatial average of  $\sigma^\circ$  can be derived as [24]

$$\bar{\sigma}^\circ = \frac{P_b}{X},$$

where  $\bar{\sigma}^\circ$  denotes the signal-only weighted spatial average of  $\sigma^\circ$  and  $X$  is a radar calibration parameter defined as

$$X = \frac{P_t \lambda^2}{(4\pi)^3} \int_A \frac{Q^2}{r^4} dA. \quad (5.2)$$

The SRF is intuitively derived by combining Eq. (5.1) and Eq. (5.2) to express  $\bar{\sigma}^\circ$  as

$$\bar{\sigma}^\circ = \int_A h(\vec{\nu}) \sigma^\circ(\vec{\nu}) d\vec{\nu}, \quad (5.3)$$

where  $\vec{\nu}$  represents a suitably defined coordinate system and  $h$  is the SRF, defined to be

$$h = \frac{\frac{Q(\vec{\nu})^2}{r(\vec{\nu})^4}}{\int_A \frac{Q(\vec{\alpha})^2}{r(\vec{\alpha})^4} d\vec{\alpha}}. \quad (5.4)$$

The SRF can be thought of as a normalized weighting function of  $\sigma^\circ$  over the area  $A$  of Earth illuminate by the antenna, such that

$$\int_A h(\vec{\nu}) d\vec{\nu} = 1,$$

and  $h(\vec{\nu}) \geq 0$ .

Estimates  $\hat{P}_b$  of the signal-only power  $P_b$  are obtained by

$$\hat{P}_b = P_r - \hat{P}_n,$$

where  $\hat{P}_n$  is an estimate of the power in the noise. The estimate of  $\bar{\sigma}^\circ$  can be obtained by

$$z = \frac{\hat{P}_b}{X} = \frac{P_b + P_n - \hat{P}_n}{X} = \bar{\sigma}^\circ + N, \quad (5.5)$$

where  $z$  represents the estimate of  $\bar{\sigma}^\circ$  and  $N$  is the noise caused by the scaled error in the estimate of the noise power, defined as

$$N = \frac{P_n - \hat{P}_n}{X}.$$

The noise is characterized by the scatterometer noise model, ie.  $N \sim \mathcal{N}(0, K_p^2 \bar{\sigma}^{\circ 2})$ , where  $K_p$  is the normalized standard deviation of echo return energy, and is a function of instrument parameters and signal to noise ratio (SNR) [35]. In summary, Eq. (5.5) represents the measurement model for OSCAT, where measured values of normalized radar backscatter reported by the satellite are actually noisy estimates  $z$  of the  $\sigma^\circ$  weighted spatial average  $\bar{\sigma}^\circ$ .

## 5.2 Mathematical Formulation

The measurement model for OSCAT  $\sigma^\circ$  measurements  $z$  is effectively the convolution of  $\sigma^\circ$  with the SRF  $h$  plus additive noise  $N$ . Inverting the measurement model to solve for  $\sigma^\circ$  using observations  $z$  is an important research problem in image reconstruction and remote sensing fields of study. A similar, yet less commonly addressed problem is to invert the measurement model to solve for  $h$  instead. To solve for  $h$ , we use a least-squares estimation

approach that takes advantage of the dense irregular sampling characteristics of satellite-borne radar, while incorporating error in measurements  $z$ . An implicit assumption is made that the SRF is stationary over a local region, allowing measurements from multiple passes of the scatterometer to be combined.

### 5.2.1 Least-squares

To incorporate antenna rotation and orbit position into the  $m^{\text{th}}$  measurement  $z_m$ , Eq. (5.5) can be rewritten as

$$z_m = \int_A h(\phi_m, \vec{x}_m, \vec{\nu}) \sigma^\circ(\vec{\nu}) d\vec{\nu} + N_m, \quad (5.6)$$

where  $\phi_m$  and  $\vec{x}_m$  are the rotation and center location of  $h$  on the surface of the earth for the  $m^{\text{th}}$  measurement. Based on assumptions made in Section 2.2 that differential Doppler shift is negligible for slices, antenna rotation and measurement location only affect the orientation of  $h$  and not its overall shape. Accordingly, shifts and rotations associated with either egg or slice measurements can be performed on  $\sigma^\circ$  instead of  $h$ , allowing  $z_m$  to be written as

$$z_m = \int_A h(\vec{\nu}) \sigma^\circ(\phi_m, \vec{x}_m, \vec{\nu}) d\vec{\nu} + N_m.$$

Discretizing the inner-product into a finite summation over a  $K$  element sample grid tangential to the Earth's surface and centered about  $h$  gives

$$z_m \approx \sum_{k=1}^K h(\vec{\nu}_k) \sigma^\circ(\phi_m, \vec{x}_m, \vec{\nu}_k) \Delta\nu + N_m,$$

where  $\vec{\nu}_k$  represents the  $K$  sampling locations over the SRF,  $\vec{x}_m$  is the center location of  $\sigma^\circ$  for the  $m^{\text{th}}$  measurement in kilometers north and east of the center of  $h$ , and  $\Delta\nu$  is a constant denoting the area ( $\text{km}^2$ ) of each grid element. The summation can then be represented as

the Euclidean inner product of vectors  $\mathbf{S}$  and  $\mathbf{h}$  for the  $m_{\text{th}}$  measurement by

$$\begin{aligned}
 z_m &\approx \mathbf{S}_m^T \mathbf{h} + N_m, \\
 \mathbf{S}_m &= \begin{bmatrix} \sigma^\circ(\phi_m, \vec{x}_m, \vec{\nu}_1) \\ \sigma^\circ(\phi_m, \vec{x}_m, \vec{\nu}_2) \\ \dots \\ \sigma^\circ(\phi_m, \vec{x}_m, \vec{\nu}_K) \end{bmatrix} \Delta\nu, \\
 \mathbf{h} &= \begin{bmatrix} h(\vec{\nu}_1) \\ h(\vec{\nu}_2) \\ \vdots \\ h(\vec{\nu}_K) \end{bmatrix},
 \end{aligned} \tag{5.7}$$

where  $\mathbf{S}$  is the discretized  $\sigma^\circ$  over a localized region of the Earth's surface, and  $\mathbf{h}$  is the discretized SRF. For  $M$  samples of  $z$  at different locations, a length  $M$  vector  $\mathbf{z}$  is formed as

$$\mathbf{z} = \begin{bmatrix} z_1 \\ z_2 \\ \vdots \\ z_M \end{bmatrix} \approx \begin{bmatrix} \mathbf{S}_1^T \\ \mathbf{S}_2^T \\ \vdots \\ \mathbf{S}_M^T \end{bmatrix} \mathbf{h} + \begin{bmatrix} N_1 \\ N_2 \\ \vdots \\ N_M \end{bmatrix} = G\mathbf{h} + \mathbf{e}, \tag{5.8}$$

providing a matrix multiplicative form of the measurement model, where  $G \in \mathbb{R}^{M \times K}$ .

In order to invert the measurement model and recover  $h$ , the sampling criteria for  $z$  must be satisfied. The non-uniform sampling characteristics of the scatterometer complicate this. In general, the spectrum of  $\sigma^\circ$  is not necessarily band limited. However, since  $\sigma^\circ$  is sampled by the low-pass  $h$ , it is effectively pre-filtered, minimizing high frequencies. Thus, with sufficiently dense sampling, as can be obtained by combining multiple passes, aliasing in the spectrum of  $z$  can be minimized and  $h$  can be recovered from  $z$  through inversion of  $G$ .

To achieve sufficiently dense sampling of  $z$ , measurements are collected for multiple passes over the sampling grid, resulting in  $M \gg K$ , such that Eq. (5.8) is overdetermined. A least-squares estimate  $\hat{\mathbf{h}}$  can be found that minimizes the  $l_2$  norm of the error  $\|\mathbf{z} - G\mathbf{h}\|_2^2$ ,

such that  $\hat{\mathbf{h}}$  is the optimum solution with respect to the  $l_2$  norm. Estimates can also be found using a method known as total least-squares, but we focus our attention on minimum least-squares in this analysis. The least-squares solution is given by the Moore-Penrose pseudo inverse of  $G$

$$\hat{\mathbf{h}}_{\text{LS}} = G^\dagger \mathbf{z}, \quad (5.9)$$

where  $G^\dagger = (G^H G)^{-1} G^H$ .

Informative estimates of  $h$  require fine grid spacing and a sufficiently large region of support that provides for possible side-lobes of the SRF. However, there is a tradeoff associated with grid spacing and region of support. The first tradeoff is memory capabilities of the computing platform. Providing a sufficient region of support while trying to decrease grid spacing results in demands on system memory that may exceed capabilities. The second tradeoff pertains to potential aliasing in the spectrum of  $z$ . The grid spacing effectively acts as a low-pass filter by averaging components that fall in a similar bin. Smaller grid spacing allows for higher resolution estimates of the SRF, but may be noisier. Larger grid spacing suppresses aliasing in SRF estimates while being more computationally friendly, but has lower resolution. To balance this tradeoff, we have chosen a grid spacing that is approximately 2.225 km/pix. Since Eq. (5.8) may be poorly conditioned, a more robust solution can be obtained through rank reduction of  $G$ .

### 5.2.2 Rank Reduced Least-squares

To improve the condition of Eq. (5.8), singular value decomposition (SVD) is used to replace the ill-conditioned matrix  $G$  with a reduced rank approximation. This is done by identifying and removing the numerically sensitive portion of  $G$ . Factoring Eq. (5.8) using SVD yields

$$\mathbf{z} = U \Sigma V^H \mathbf{h} + \mathbf{e}, \quad (5.10)$$

where  $U \in \mathbb{R}^{M \times M}$  is unitary,  $V \in \mathbb{R}^{K \times K}$  is unitary, and  $\Sigma \in \mathbb{R}^{M \times K}$  is a diagonal matrix with the singular values  $\xi$  of  $G$  ordered down the diagonal so that

$$\xi_1 \geq \xi_2 \geq \dots \geq \xi_p \geq 0,$$

where  $p \leq \min(M, K)$  [42].

To quell amplification of noise in the estimate of  $\mathbf{h}$ , the small singular values of  $G$  are zeroed out to obtain an approximation  $\Sigma_1$  of the singular value matrix  $\Sigma$ . The rank-reduced approximation for  $G$  is obtained by

$$\tilde{G} = \begin{bmatrix} U_1 & U_2 \end{bmatrix} \begin{bmatrix} \Sigma_1 & 0 \\ 0 & \Sigma_2 \end{bmatrix} \begin{bmatrix} V_1^H \\ V_2^H \end{bmatrix} = U_1 \Sigma_1 V_1^H, \quad (5.11)$$

where  $U_1 \in \mathbb{R}^{M \times L}$ ,  $\Sigma_1 \in \mathbb{R}^{L \times L}$ , and  $V_1 \in \mathbb{R}^{K \times L}$  are the respective portions of  $U$ ,  $\Sigma$ , and  $V$  corresponding to the first  $L < p$  significant singular values of  $G$ , and  $U_2$ ,  $\Sigma_2$ , and  $V_2$  are zero-matrices corresponding to the small singular values. Solving for  $\mathbf{h}$  in Eq. (5.10) using rank-reduced approximation yields

$$\hat{\mathbf{h}}_{\text{SVD}} = \tilde{G}^\dagger \mathbf{z} = V_1 \Sigma_1^{-1} U_1^H \mathbf{z}, \quad (5.12)$$

where the inverse of  $\Sigma_1$  is trivial because it is a diagonal matrix.

The computational complexity of the SVD is reduced by using a small number of significant singular values. However, the accuracy of  $\hat{\mathbf{h}}_{\text{SVD}}$  varies greatly based on  $L$ . Increasing  $L$  reduces reconstruction error, but at the risk of amplifying noise in  $z$ , as well as introducing noise into the reconstruction process. The optimum choice of  $L$  to minimize reconstruction error can be determined through simulation, as is shown in Section 5.4.

While the rank reduced least-squares technique produces satisfactory results for visualization, the solution is large and burdensome for implementation in algorithms necessitating knowledge of the SRF. Additionally, since the SRF varies over the Earth's surface depending on location, an estimate found in a tangential plane needs to be projected into the antenna azimuth and elevation angle space for universal use. Accordingly, a parameterized estimate

of  $\mathbf{h}$  in antenna azimuth and elevation angle space is sought to provide for more universal, computationally friendly algorithms.

### 5.2.3 Parameterization

A parameterized estimate of  $\mathbf{h}$  for eggs can be obtained in antenna azimuth and elevation angle space using a spatially varying 2nd-order polynomial for robustness. The parameterized SRF is represented as

$$\mathbf{h} = R\mathbf{b},$$

where  $R = [\zeta^2, \zeta, \psi^2, \psi, \mathbf{1}] \in \mathbb{R}^{K \times 5}$ ,  $\mathbf{b} = [b_1, \dots, b_5] \in \mathbb{R}^{5 \times 1}$ , and  $\zeta$  and  $\psi$  are respectively the azimuth and elevation angles of the antenna beam about the center of  $\mathbf{h}$ . Inserting the parameterized definition of  $\mathbf{h}$  into Eq. (5.8) and solving for  $\mathbf{b}$  in the least-squares sense results in

$$\hat{\mathbf{b}} = (G_\Psi B_\Psi R_\Psi)^\dagger \mathbf{z}_\Psi, \quad (5.13)$$

where  $B_\Psi = \text{diag}(\Delta\nu_1, \Delta\nu_2, \dots, \Delta\nu_\Psi) / \Delta\nu \in \mathbb{R}^{\Psi \times \Psi}$  is a diagonal matrix composed of normalized scaling factors to account for the area of each grid element,  $\Delta\nu_k$  is the area ( $\text{km}^2$ ) projected on the Earth's surface by the  $k^{\text{th}}$  grid element defined in antenna azimuth and elevation angle space, and the  $\Psi$  denotes that the estimation is only performed over the main lobe of  $\mathbf{h}$ . Having estimated  $\mathbf{b}$ , the estimate of the SRF is then computed by

$$\hat{\mathbf{h}}_{\text{par}} = R\hat{\mathbf{b}}. \quad (5.14)$$

The next section discusses construction of  $G$ , the choice of sampling region, and methodology for approximating  $\sigma^\circ$ .

## 5.3 Geographic Sampling Region

Constructing the matrix  $G$  presented in Eq. (5.8) requires a model for  $\mathbf{S}$ . Even though the  $\sigma^\circ$  of the Earth's surface is not known exactly, good approximations can be made for regions with known geographical composition, like islands. By selecting isolated islands that

are elliptical in shape as homogeneous targets against a “dim” ocean background,  $\mathbf{S}$  can be modeled as an ellipsoid of constant  $\sigma^\circ$  over  $\vec{v}_i$  in an ocean background  $\vec{v}_o$ , where  $\vec{v}_i$  and  $\vec{v}_o$  represent island and ocean pixels, respectively. Important to maintaining accurate SRF estimation is selecting islands at high latitude locations to ensure high diversity in azimuthal and incidence geometries, as discussed in Section 2.2.

### 5.3.1 Island Targets

Advantages of island targets include simplicity and high signal to clutter ratio (SCR) in  $\sigma^\circ$  measurements, where signal refers to the island  $\sigma^\circ$  and clutter refers to the ocean  $\sigma^\circ$ . High SCR is required to potentially recover information contained in the sidelobes of the SRF. When using an island model an important consideration is the island size.

To achieve full reconstruction over the spatial main lobe of  $\mathbf{h}$ , we require that there be no nulls within the spectral region of support of the island  $\sigma^\circ$ . Typically,  $\mathbf{h}$  has low pass characteristics due to the antenna aperture, while the island  $\sigma^\circ$  model used in the construction of  $G_i$  exhibits a sinc-like spectrum. The wave number at which nulls in the island  $\sigma^\circ$  spectrum occur are inversely proportional to the size of the island. If nulls of the island  $\sigma^\circ$  spectrum lie within the spectral region of support of the main lobe of  $\mathbf{h}$ , irretrievable information is lost and full reconstruction of the main lobe of  $\mathbf{h}$  hindered. This suggests using smaller islands to push the spectral nulls outside the spectral region of support of the main lobe of  $\mathbf{h}$ . However, small islands exhibit lower SCR than do large islands, decreasing the effective SNR in reconstruction of  $\mathbf{h}$ . To achieve minimum error in estimates of  $\mathbf{h}$ , island size is determined through simulation in Section 5.4 to optimize the trade-off between the frequency response requirement on island  $\sigma^\circ$  and SCR.

### 5.3.2 Background $\sigma^\circ$

Depending on the location, the ocean background may be open ocean, sea ice, or a combination of both. Ocean  $\sigma^\circ$  is also highly variable temporally and spatially due to weather phenomena, ocean currents, and sea ice flows. While season and weather phenomena can cause changes in island  $\sigma^\circ$  as well, data is selected such that the island  $\sigma^\circ$  is approximately constant by avoiding days during the melt season or severe weather phenomena. Temporal

variability in the mean  $\sigma^\circ$  of the island can be mitigated by normalizing the  $\sigma^\circ$  measurements for each pass over the island. Ocean  $\sigma^\circ$ , however, is less predictable and is more difficult to model due to wind and random flows in the sea ice.

To minimize the complexity of the ocean  $\sigma^\circ$  model, it is necessary to modify the problem somewhat. The original problem set forth in Eq. (5.8) can be decomposed into individual island and ocean components as

$$G\mathbf{h} + \mathbf{e} = (G_i + G_o)\mathbf{h} + \mathbf{e} = \mathbf{z}_i + \mathbf{z}_o = \mathbf{z},$$

where  $i$  and  $o$  denote island and ocean components respectively, and  $G_i$  and  $G_o$  are disjoint matrices since  $\vec{\nu}_i \cap \vec{\nu}_o$ . By doing so, ocean  $\sigma^\circ$  can be disregarded completely by simplifying the problem to

$$G_i\mathbf{h} + \mathbf{e} = \mathbf{z} - \hat{\mathbf{z}}_o = \hat{\mathbf{z}}_i, \quad (5.15)$$

where  $\hat{\mathbf{z}}_i$  and  $\hat{\mathbf{z}}_o$  are estimates of the island contribution and ocean contribution, respectively, of measurements near the island. In this case, “near” means within about two times the 3 dB antenna elevation beamwidth from the island. Thus, measurements used in the estimation are restricted to being near the island to ensure a dominant land contribution. The ocean contribution  $\mathbf{z}_o$  is estimated separately for each pass using a least-squares, spatially varying quadratic fit over an extended area outside the 10 dB antenna footprint. After removal of the estimated ocean contribution  $\hat{\mathbf{z}}_o$  from measurements near the island, the estimation methods for  $\mathbf{h}$  can then be applied to the simplified model of Eq. (5.15).

## 5.4 Simulation

Simulations are performed to validate the efficacy of the method outlined above for eggs and slices. By comparing the reconstruction error due to simulated signal-only measurements and measurements of noise simulated using a typical  $K_p$  value for OSCAT, it is found that with sufficiently dense sampling, reconstruction error due to measurement noise is insignificant compared to reconstruction error due to signal-only measurements. The remainder of this section focuses on minimizing the reconstruction error from signal-only measurements. This is done through a simulation that provides a method to select opti-

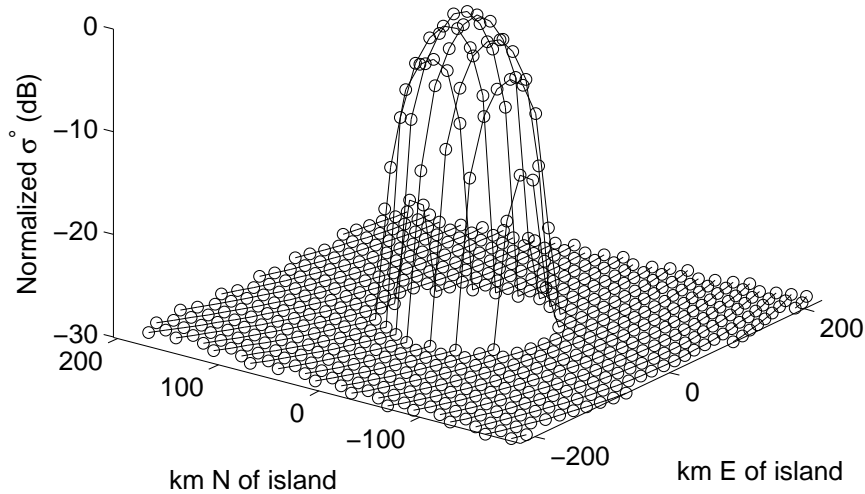


**Figure 5.1:** Signal-only simulated measurements  $z_s$  for eggs with island size corresponding to  $\gamma = 0.75$ . Measurements are shown for one pass of rev 1002 over the Peter I island. Each point represents the spatial average of  $\mathbf{S}_s$  weighted by  $\mathbf{h}_s$ , and locations corresponds to the center of  $\mathbf{h}_s$  upon sampling. The measurements are normalized in the plot.

mal island size and number of significant singular values  $L$  that results in the minimum reconstruction error.

#### 5.4.1 Simulation Procedure

Simulated signal-only measurements  $z_s$  used in the simulation procedure are constructed via the inner product of Eq. (5.7) without the noise term. The subscript  $s$  is used to denote a simulated quantity. A binary SRF  $\mathbf{h}_s$  is used with center locations  $\vec{x}$  and rotations  $\phi$  taken from reported OSCAT H-pol cell measurements over the Peter I island [68°50'50" S, 90°35'41" W], and various simulated  $\sigma^\circ$  scenes  $\mathbf{S}_s$ . The matrix multiplicative form of the simulation measurement model is

$$\mathbf{z}_s = G_s \mathbf{h}_s, \quad (5.16)$$

where  $\mathbf{z}_s$  is a length  $M$  vector of simulated signal-only measurements, and  $G_s$  is composed of the simulated  $\sigma^\circ$  scenes corresponding to the  $M$  measurements.

The synthetic  $\sigma^\circ$  scenes  $\mathbf{S}_s$  used for measurement simulation consist of circular islands characterized by homogeneous backscatter in a constant backscatter ocean background

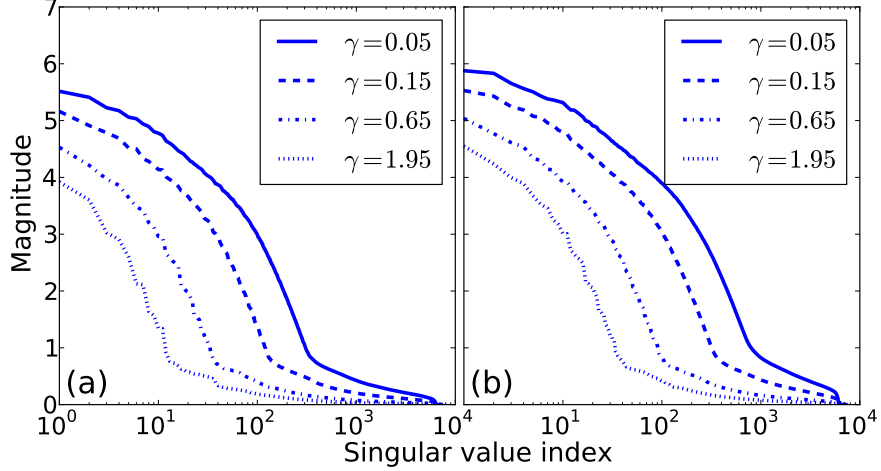


**Figure 5.2:** Singular value curves of  $G_s(\gamma)$  for (a) egg and (b) slice simulations. The x-axis is shown on a logarithmic scale. The singular values can be divided into two groups by the elbow in each respective curve. Generally, the upper part of the curve corresponds to the signal, while the lower part corresponds to the noise.

–30 dB down with respect to an island. The islands are constructed to be centered about the center location of the Peter I island and have an area given by  $A_I = \gamma A_h$ , where  $A_I$  is the area of a given island,  $A_h$  is the area of the earth illuminated by the 3 dB response of  $\mathbf{h}_s$ , and  $\gamma$  is the area ratio. For simulated egg measurements,  $\mathbf{h}_s$  is circular, while for slice measurements  $\mathbf{h}_s$  is rectangular. Figure 5.1 shows simulated signal-only egg measurements for  $\gamma = 0.75$  during one pass over the Peter I island on rev 1002.

Estimates  $\hat{\mathbf{h}}_s$  of simulated SRFs are computed using the rank-reduced least-squares method

$$\hat{\mathbf{h}}_s = \tilde{G}_s^\dagger \mathbf{z}_s. \quad (5.17)$$

The accuracy of  $\hat{\mathbf{h}}_s$  is determined through two metrics:  $\epsilon = |B_3(\mathbf{h}_s) - B_3(\hat{\mathbf{h}}_s)|$ , the absolute value of the difference in mean 3 dB beamwidths  $B_3$  of the  $\mathbf{h}_s$  and  $\hat{\mathbf{h}}_s$ , and  $\delta = \sqrt{\frac{1}{K}(\mathbf{h}_s - \hat{\mathbf{h}}_s)^\top (\mathbf{h}_s - \hat{\mathbf{h}}_s)}$ , the root-mean-squared (RMS) reconstruction error. The mean 3 dB beamwidth  $B_3$  is the average of 3 dB beamwidths calculated at different aspect angles about the center of an individual SRF. The reconstruction error is  $\mathbf{h}_s - \hat{\mathbf{h}}_s$ , where  $\hat{\mathbf{h}}_s$  is first normalized to one by dividing by its maximum value to eliminate biases in  $\delta$  as a result of relative magnitude differences between  $\mathbf{h}_s$  and  $\hat{\mathbf{h}}_s$ . The first metric  $\epsilon$  can give a good sense of error in the size of  $\hat{\mathbf{h}}_s$ , but it offers no sense of directional biases within the SRF window. The

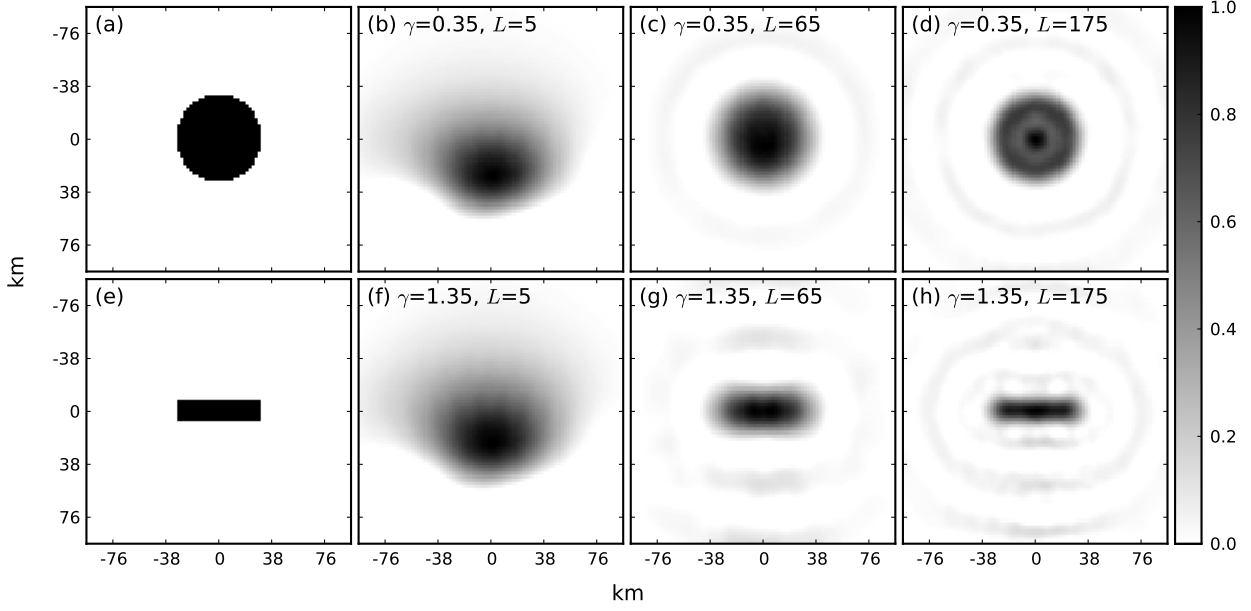


**Figure 5.3:** Images of (a) the egg  $\mathbf{h}_s$  and (b)-(d) its estimates  $\hat{\mathbf{h}}_s$  for  $\gamma = 0.15$ , and (e) the slice  $\mathbf{h}_s$  and (f)-(g) its estimates  $\hat{\mathbf{h}}_s$  for  $\gamma = 1.35$ . The x and y axis represent km in  $\zeta$  and  $\psi$ , respectively, in a tangent plane at the Earth's surface. The grid spacing is approximately 2.225 km per pixel. The egg  $\hat{\mathbf{h}}_s$  corresponding to (b)  $L = 5$ , (c)  $L = 65$ , and (d)  $L = 175$ , and slice  $\hat{\mathbf{h}}_s$  corresponding to (f)  $L = 5$ , (g)  $L = 65$ , and (h)  $L = 175$  are normalized to one by their respective maximum values.

second metric  $\delta$  helps provide a sense of directional biases in  $\hat{\mathbf{h}}_s$ , while also offering a sense of size accuracy. However, without  $\epsilon$  there is some ambiguity as to whether the increase in  $\delta$  is caused by error in the location or size of  $\hat{\mathbf{h}}_s$ . Therefore, the two metrics serve to compliment each other and minimize ambiguities.

For determining the optimum values of  $\gamma$  and  $L$  we use

$$\gamma, L = \arg \min_{\gamma, L} \delta(\gamma, L). \quad (5.18)$$

The metric  $\epsilon$  is used to verify that outcomes of  $\gamma$  and  $L$  do not lead to significant errors in the size of  $\hat{\mathbf{h}}_s$ . For egg and slice simulation, synthetic islands are created for  $\gamma = 0.05 - 1.95$ . The singular value curves of  $G_s(\gamma)$  for eggs and slices are shown in Figure 5.2 for multiple values of  $\gamma$ . The elbow in each curve divides singular values into the signal (upper portion) and the noise (lower portion). Since higher singular values correspond to higher frequency information in  $G_s(\gamma)$ , it is appropriate that  $L$  decreases as the nulls in the  $\sigma^\circ$  spectrum of

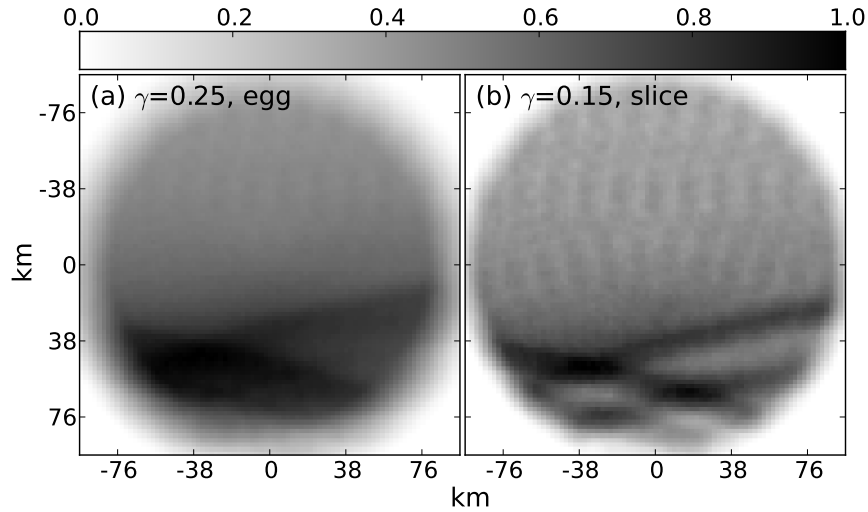


**Figure 5.4:** Images of the normalized distribution of island  $\sigma^\circ$  locations over the observation window for (a)  $\gamma = 0.25$  with respect to the egg  $\mathbf{h}_s$ , and (b)  $\gamma = 0.15$  with respect to the slice  $\mathbf{h}_s$ . The x and y axis represent km in  $\zeta$  and  $\psi$ , respectively, in a tangent plane at the Earth's surface. The grid spacing is approximately 2.225 km per pixel.

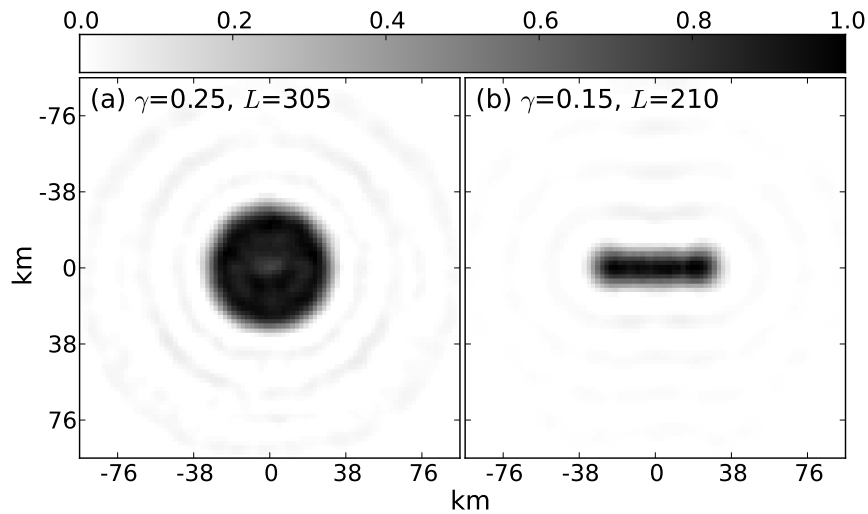


**Figure 5.5:** Images of  $\hat{\mathbf{h}}_s$  corresponding to the optimum values of  $\gamma$  and  $L$  for (a) egg and (b) slice  $\mathbf{h}_s$ . The optimum values of  $\gamma$  and  $L$  are  $\gamma = 0.25$  and  $L = 305$  singular values for eggs, and  $\gamma = 0.15$  and  $L = 210$  singular values for slices. The x and y axis represent km in  $\zeta$  and  $\psi$ , respectively, in a tangent plane at the Earth's surface. The grid spacing is approximately 2.225 km per pixel, and the responses have been normalized to one by their respective maximum values.

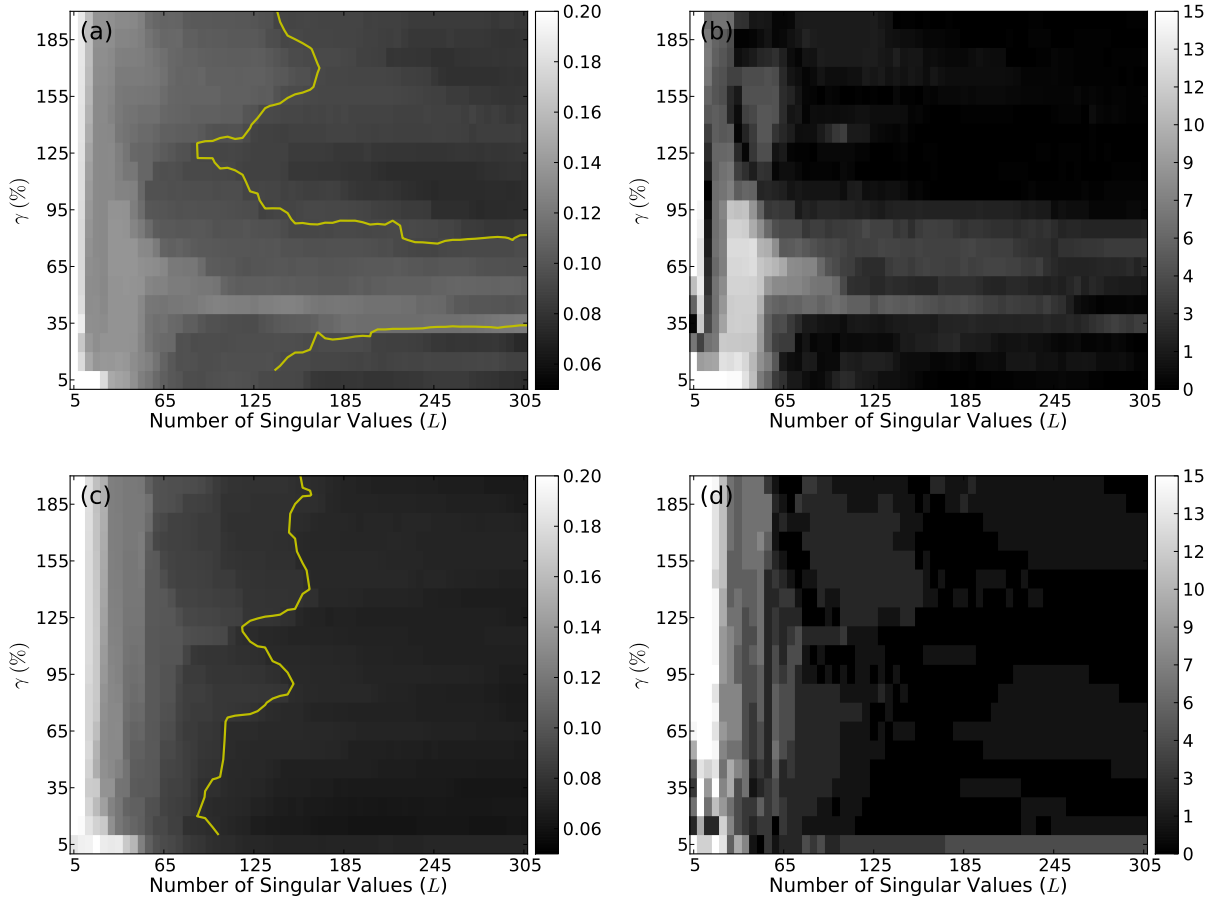


**Figure 5.6:** Gridded images of the RMS reconstruction error  $\delta$  for (a) eggs and (c) slices, and the absolute value of the difference  $\epsilon$  of mean 3 dB beamwidths  $B_3$  for (b) eggs and (d) slices. The grids represent  $\delta$  and  $\epsilon$  for  $\gamma$  versus  $L$ . A yellow contour line is shown on images of  $\delta$  at values 25% greater than the respective minimum of each image.

larger islands move towards lower wave numbers. A simulation range of  $L = 5 - 305$  singular values is set based on the singular value curve of  $G_s(\gamma = 0.15)$  for slices.

#### 5.4.2 Simulation Results

Based on actual sampling geometry from L1B data for JD 309 of 2009 through JD 284 of 2011, egg and slice measurements  $z_s$  are simulated and  $\hat{\mathbf{h}}_s$  is computed for the entire range of  $\gamma$  and  $L$ . Figure 5.3 shows  $\hat{\mathbf{h}}_s$  computed using several values of  $L$  for the simulated egg SRF with  $\gamma = 0.35$  and the simulated slice SRF with  $\gamma = 1.35$ , along with their respective  $\mathbf{h}_s$ . The location bias of the main lobe of egg and slice  $\hat{\mathbf{h}}_s$  for  $L = 5$  is an artifact of the

irregular OSCAT sampling geometry of H-pol measurements over the Peter I island. Due to the exact repeat of the Oceansat-2 satellite orbit and synchronicity of antenna scan rate with PRF, there are more measurements in the lower left-hand portion of the SRF window, as can be seen in the normalized distribution of simulated island  $\sigma^\circ$  locations over the observation window shown in Figure 5.4. This causes a relative location bias in SRF estimates for the first few singular values that can be seen in Figures 5.3b and 5.3f. The relative location bias of  $\hat{\mathbf{h}}_s$  is the primary cause of increased values of  $\delta$  for  $L \leq 5$ , visible in Figures 5.6a and 5.6c. However, the low values of  $\epsilon$  for  $L \leq 5$  and  $0.15 \leq \gamma \leq 0.55$  for eggs and slices shown in Figures 5.6b and 5.6d indicate that this has no impact on  $\epsilon$ .

The values of  $\gamma$  and  $L$  that optimize  $\hat{\mathbf{h}}_s$  with respect to Eq. (5.18) are  $\gamma = 0.25$  and  $L = 305$  for the simulated egg SRF, and  $\gamma = 0.15$  and  $L = 210$  for the simulated slice SRF, resulting in  $\delta(0.25, 305) = 0.075$  and  $\delta(0.15, 210) = 0.062$ , respectively. Realizations of the egg and slice  $\hat{\mathbf{h}}_s$  for the optimum  $\gamma$  and  $L$  are shown in Figure 5.5.

Because this simulation is performed using only the H-pol measurement geometry of OSCAT over the Peter I island, the results in Figure 5.6 can only serve as a guideline for island size selection. Estimates of the egg SRF tend to be more sensitive to island size choice than estimates of the slice SRF. The contour line on images of  $\delta$  represent values within 25% of the minimum. Reconstruction error can be minimized by estimating the SRF using islands and singular values corresponding to  $\gamma$  and  $L$  for values of  $\delta$  below the contours in Figure 5.6.

## 5.5 Spatial Response Function Estimates

Options for geographical sampling regions are very limited since island selection is restricted to high latitude or polar regions. Many viable options for islands corresponding to optimum  $\gamma$  with respect to egg and slice SRF are eliminated. Conveniently, there are two islands that fall within the lower bound on  $\gamma$  for the egg SRF: the Peter I Island and the Bear Island (Bjørnøya) [74°25'30" N, 19°2' E]. Peter I and Bear islands can be closely approximated with an ellipse of dimensions 11 km x 19 km and 12 km x 20 km, respectively. Corresponding egg and slice  $\gamma$  values for the Peter I and Bear islands are given in Table 5.1,

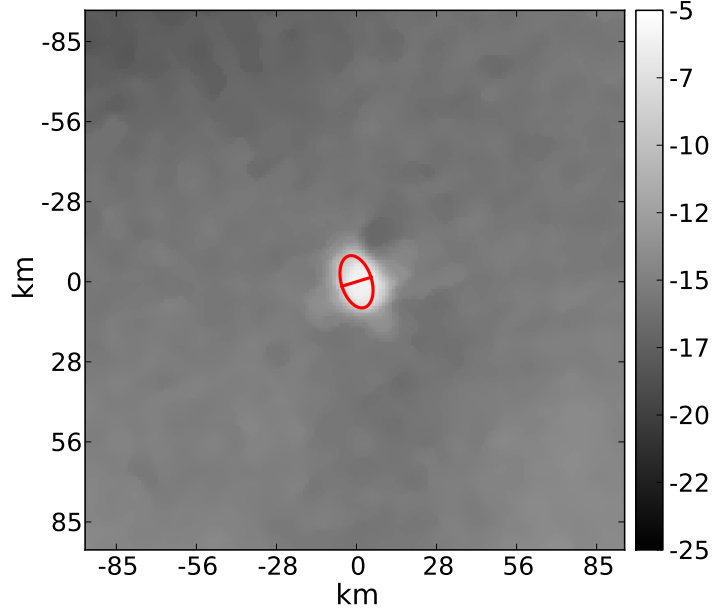


**Figure 5.7:** A QuikSCAT slice  $\mathcal{A}_h$ -SIR image of the Peter I Island for JD 180-210 of 2008. The image represents  $\sigma^\circ$  in dB over the island using a Lambert equal-area projection with a pixel resolution of about 1.113 km per pixel. The red line traces out the elliptical approximation used for the island in estimation.

**Table 5.1:** Approximate values of  $\gamma$  computed for Peter I and Bear islands.

Island (dimensions)	H-pol		V-pol	
	Egg	Slice	Egg	Slice
Peter I (11 x 19 km)	0.17	1.16	0.10	1.16
Bear (12 x 20 km)	0.19	1.32	0.11	1.32

where  $\gamma$  values are approximated by using the footprint dimensions from Table 2.1 and slice measurement separations of 6.6 km for H-pol and 5.9 km for V-pol.

Owing to the close proximity of the Peter I Island to the coast of Antarctica, during the majority of the year it is completely surrounded by sea ice. While sea ice generally exhibits consistently greater  $\sigma^\circ$  than does the ocean, thereby decreasing the SCR, it is also much more temporally and spatially uniform than open ocean. This is because sea ice  $\sigma^\circ$  doesn't change with wind, whereas changes in  $\sigma^\circ$  induced by wind over the open ocean results in high variability in the ocean background. Consequently, fewer measurements are needed with a sea ice background than with an open ocean background to obtain comparable

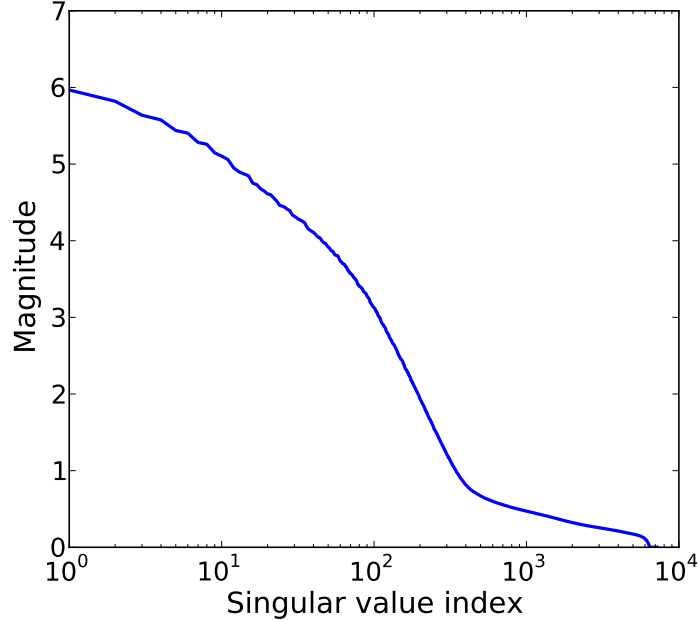


**Figure 5.8:** Singular value curve of  $G$  constructed for the Peter I island using H-pol egg measurements. The x-axis is shown on a logarithmic scale. The singular values are naturally divided by the elbow in the curve. Generally, the upper part of the curve corresponds to the signal, while the lower part corresponds to the noise.

estimates. Because the time series of available OSCAT data is very limited, we chose the Peter I Island as our focus in SRF estimation. Figure 5.7 shows a QuikSCAT SIR image of the Peter I Island for JD 180-210 of 2008.

The estimation procedure is performed for individual eggs and slices of the inner and outer beams of OSCAT using L1B measurements collected from  $67^{\circ}1'48''$  S,  $85^{\circ}19'48''$  W to  $70^{\circ}37'48''$  S,  $95^{\circ}49'48''$  W for JD 105-338 of 2011. Eq. (5.15) is used as the measurement model to simplify implementation with actual data. Figure 5.8 shows the Singular value curve of  $G_i$  constructed for the Peter I Island using H-pol egg measurement locations. The singular value curves for other H-pol and V-pol measurements are similar.

Both  $\hat{\mathbf{h}}_{\text{SVD}}$  and  $\hat{\mathbf{h}}_{\text{Par}}$  are computed for egg measurements, while only  $\hat{\mathbf{h}}_{\text{SVD}}$  is computed for slice measurements. Figure 5.9 shows  $\hat{\mathbf{h}}_{\text{SVD}}$  and  $\hat{\mathbf{h}}_{\text{Par}}$  for egg SRFs computed using  $L = 165$  for H-pol and  $L = 145$  for V-pol. Figures 5.10 and 5.11 show  $\hat{\mathbf{h}}_{\text{SVD}}$  for all H-pol and V-pol slice SRFs, respectively. All slice SRF estimates are computed using  $L = 225$

**Table 5.2:** Calculated 3 dB beamwidths for OSCAT H-pol SRF estimates.

Type	3 dB Beamwidth (Az x El) (km)
Egg	17.8 x 30.8
Slice 0	15.8 x 11.1
Slice 1	16.6 x 11.1
Slice 2	17.8 x 9.5
Slice 3	20.4 x 10.3
Slice 4	20.1 x 11.6
Slice 5	18.1 x 11.1
Slice 6	16.6 x 11.3

**Table 5.3:** Calculated 3 dB beamwidths for OSCAT V-pol SRF estimates.

Type	3 dB Beamwidth (Az x El) (km)
Egg	20.1 x 37.9
Slice 0	20.1 x 11.6
Slice 1	21.4 x 11.6
Slice 2	20.6 x 10.3
Slice 3	19.0 x 12.9
Slice 4	22.6 x 11.1
Slice 5	22.6 x 11.1
Slice 6	24.9 x 13.4
Slice 7	23.7 x 12.9
Slice 8	24.9 x 11.1
Slice 9	31.2 x 11.1
Slice 10	26.8 x 14.2
Slice 11	20.6 x 14.2

singular values. The azimuth and elevation 3 dB beamwidths of the estimates are given in Table 5.2 for H-pol and Table 5.3 for V-pol.

As a result of decreased SCR attributed to sea ice surrounding the Peter I Island, only limited information about the sidelobes is obtainable. The 3 dB beamwidths of the estimates are on the order of the reported 3 dB footprints in Table 2.1, verifying acceptable reconstruction of the SRF over the main lobe. Two factors limiting this SRF estimation method are a short time series of available OSCAT L1B data and limited measurement geometries. It is expected that with a longer time series of OSCAT L1B data, better estimates

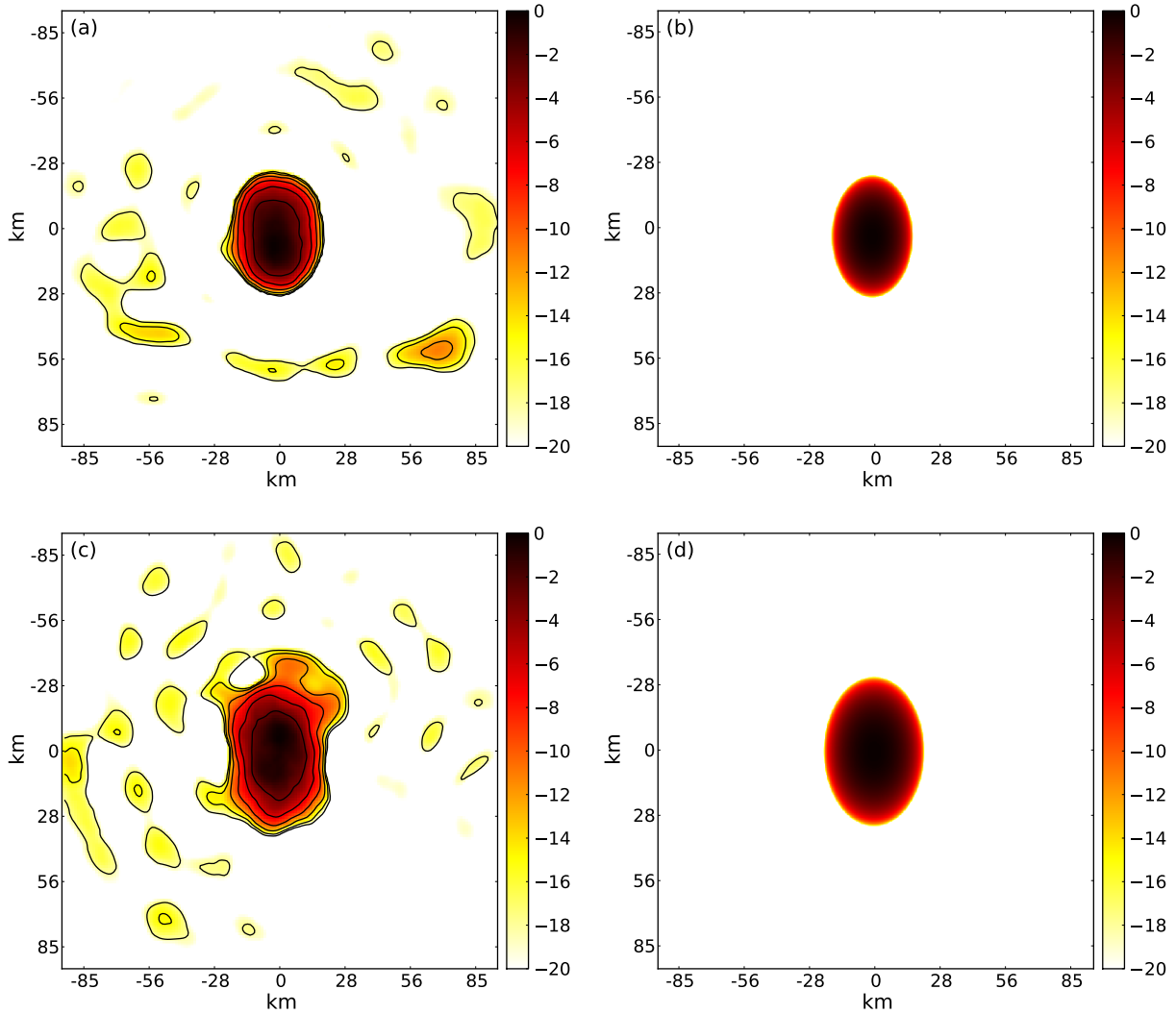


**Figure 5.9:** Images of egg (a) H-pol  $\hat{\mathbf{h}}_{\text{SVD}}$ , (b) H-pol  $\hat{\mathbf{h}}_{\text{Par}}$ , (c) V-pol  $\hat{\mathbf{h}}_{\text{SVD}}$ , and (d) V-pol  $\hat{\mathbf{h}}_{\text{Par}}$ . Estimates are computed over the Peter I Island using  $L = 165$  for H-pol and  $L = 145$  for V-pol. The x and y axis represent km in  $\zeta$  and  $\psi$ , respectively, in a tangent plane at the Earth's surface. The estimates have been interpolated to a grid spacing of approximately 1.113 km per pixel and normalized to one by their respective max values for visualization. The image scale is in dB.

are achievable using the proposed estimation procedure. A longer time series allows us to be more meticulous in maintaining uniformity in the ocean background while ensuring a sufficiently large number of measurements for noise suppression. ISRO allowing the orbit to drift in longitude could increase the diversity of measurement geometries, thereby decreasing the possibility of directional biases in SRF estimates.

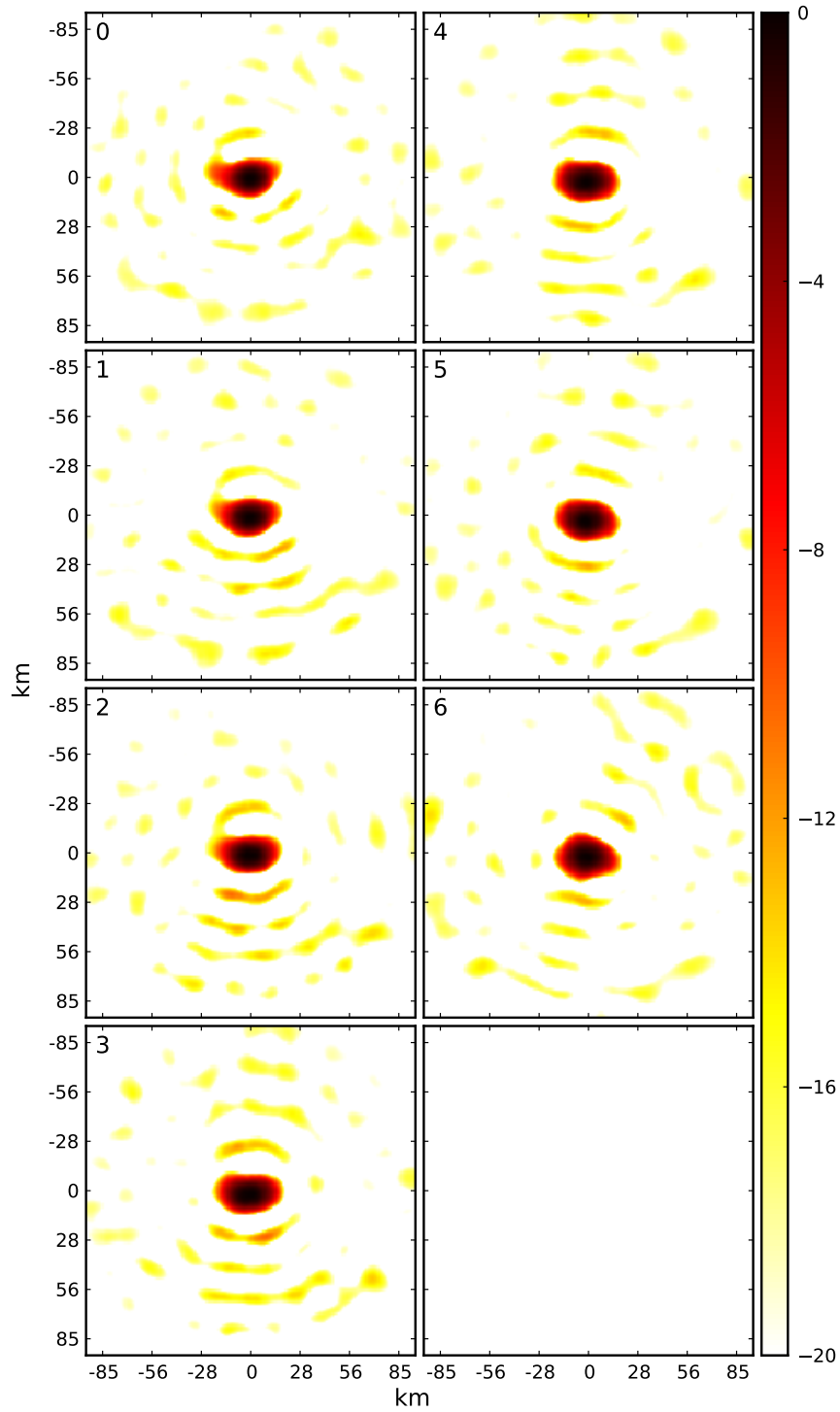


**Figure 5.10:** Images of  $\hat{\mathbf{h}}_{\text{SVD}}$  for all H-pol slices computed over the Peter I Island using  $L = 225$ . The slice number is indicated in the image. The x and y axis represent km in  $\zeta$  and  $\psi$ , respectively, in a tangent plane at the Earth's surface. The estimates have been interpolated to grid spacing of approximately 1.113 km per pixel and normalized to one by their respective max values for visualization. The image scale is in dB.

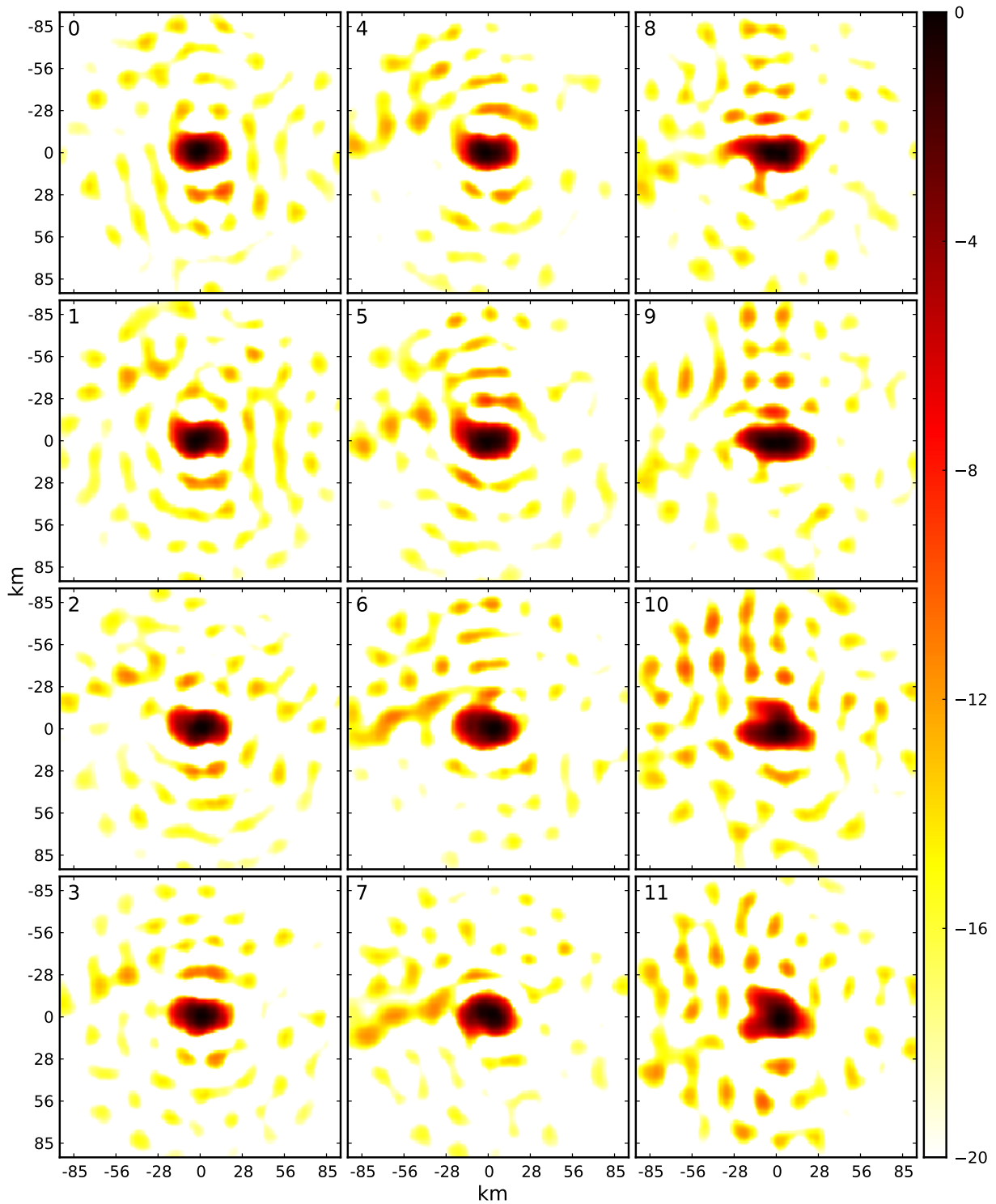


**Figure 5.11:** Images of  $\hat{h}_{\text{SVD}}$  for all V-pol slices computed over the Peter I Island using  $L = 225$ . The slice number is indicated in the image. The x and y axis represent km in  $\zeta$  and  $\psi$ , respectively, in a tangent plane at the Earth’s surface. The estimates have been interpolated to grid spacing of approximately 1.113 km per pixel and normalized to one by their respective max values for visualization. The image scale is in dB.

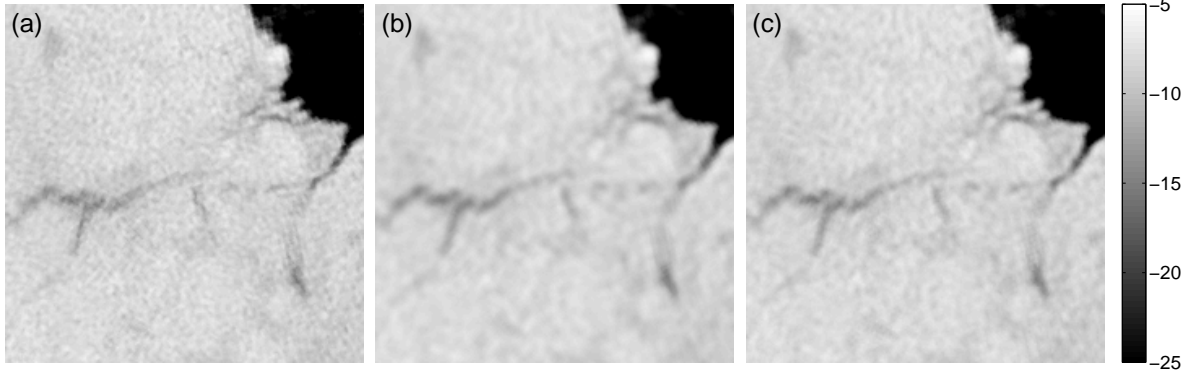


**Figure 5.12:** OSCAT egg  $\mathcal{A}_h$ -SIR images of the Amazon basin for JD 25-26 of 2012 created using (a) the current simple approximation, (b) an improved approximation, and (c) the H-pol egg  $\hat{\mathbf{h}}_{\text{Par}}$ . The region shown corresponds to a box defined by  $[48^\circ 22' \text{ W to } 57^\circ 32' \text{ W}, 6^\circ 20' \text{ S to } 2^\circ 50' \text{ N}]$ . The pixel resolution is approximately 4.45 km per pixel and the grayscale is in dB.

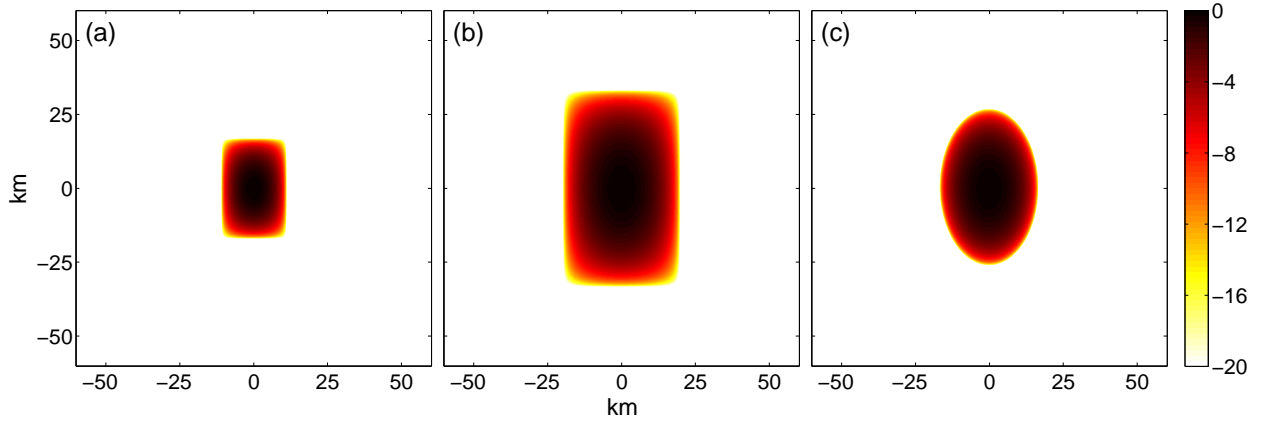


**Figure 5.13:** Images of (a) the simple approximation, (b) the improved approximation, and (c) the parameterized estimate  $\hat{\mathbf{h}}_{\text{Par}}$  of H-pol egg SRF used in creating the  $\mathcal{A}_h$ -SIR images of the Amazon basin for JD 25-26 of 2012. The grid spacing is approximately 1.113 km per pixel and the responses have been normalized to one by their respective max values for visualization. The image scale is in dB.

To demonstrate the utility of SRF estimation, the H- and V-pol egg  $\hat{\mathbf{h}}_{\text{Par}}$  are used to create egg SIR images of the Amazon basin for JD 25-26 of 2012. They are compared with SIR images made using simple approximations currently employed, and SIR images made using improved approximations that match more closely the reported footprint dimensions of OSCAT. The egg  $\mathcal{A}_h$ -SIR images are shown in Figure 5.12 with respective SRFs shown in Figure 5.13, and the egg  $\mathcal{A}_v$ -SIR images are shown in Figure 5.14 with respective SRFs

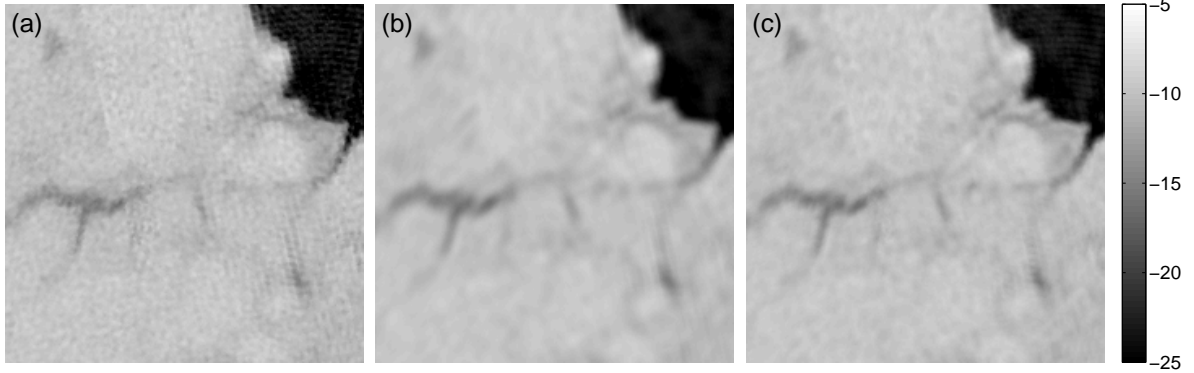


**Figure 5.14:** OSCAT egg  $\mathcal{A}_v$ -SIR images of the Amazon basin for JD 25-26 of 2012 created using (a) the current simple approximation, (b) an improved approximation, and (c) the V-pol egg  $\hat{\mathbf{h}}_{\text{Par}}$ . The region shown corresponds to a box defined by  $[48^\circ 22' \text{ W to } 57^\circ 32' \text{ W}, 6^\circ 20' \text{ S to } 2^\circ 50' \text{ N}]$ . The pixel resolution is approximately 4.45 km per pixel and the grayscale is in dB.

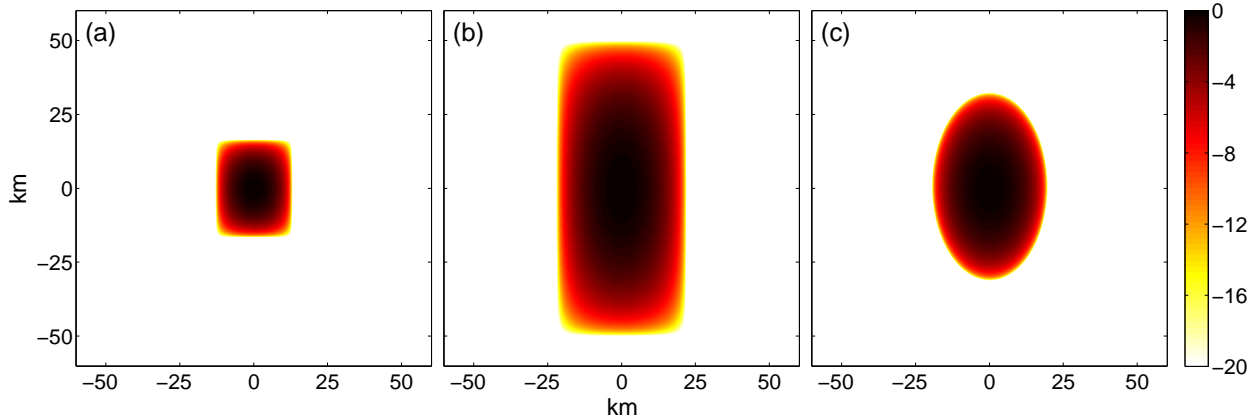


**Figure 5.15:** Images of (a) the simple approximation, (b) the improved approximation, and (c) the parameterized estimate  $\hat{\mathbf{h}}_{\text{Par}}$  of V-pol egg SRF used in creating the  $\mathcal{A}_v$ -SIR images of the Amazon basin for JD 25-26 of 2012. The grid spacing is approximately 1.113 km per pixel and the responses have been normalized to one by their respective max values for visualization. The image scale is in dB.

shown in Figure 5.15. QuikSCAT egg  $\mathcal{A}_h$ - and  $\mathcal{A}_v$ -SIR images of the same region for JD 25-28 of 2009 are also shown in Figure 5.16.

Both the parameterized estimate  $\hat{\mathbf{h}}_{\text{Par}}$  and the improved approximation of the SRF significantly decrease the amount of noise present in the SIR images. Since the SRF estimates tend to be slightly smaller than the reported footprint dimensions of OSCAT, there is less spatial averaging than with the improved approximation. The increase in spatial averaging

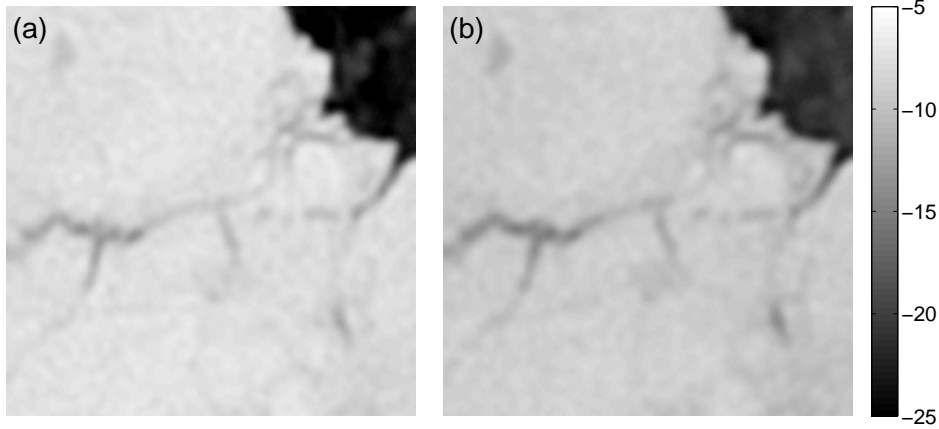


**Figure 5.16:** A QuikSCAT egg (a)  $\mathcal{A}_h$ -SIR image and (b)  $\mathcal{A}_v$ -SIR image of the Amazon basin for JD 25-28 of 2009. The region shown corresponds to a box defined by  $[48^\circ 22' \text{ W to } 57^\circ 32' \text{ W}, 6^\circ 20' \text{ S to } 2^\circ 50' \text{ N}]$ . The pixel resolution is approximately 4.45 km per pixel and the grayscale is in dB.

with the improved approximation leads to decreased noise in SIR images, but at the loss of resolving capabilities. The loss of resolution is especially noticeable along the coast of South America visible in the top-right corner of the images, and along portions of the Amazon River. For  $\mathcal{A}_h$ -SIR images, the improved approximation seems to be superior because of its ability to suppress noise. However, the improved approximation causes an excessive amount of smearing and blurring in the  $\mathcal{A}_v$ -SIR images, making the parameterized estimate superior for  $\mathcal{A}_v$ -SIR images. In summary, while there is improved resolution capability with the parameterized estimate, there is also a potential for increased noise in the SIR images.

## 5.6 Summary

I have demonstrated that it is possible to understand the SRF of OSCAT without knowing specifics of the onboard processing. Estimates of the SRF can be obtained by inverting the integral form of the mono-static radar equation using  $\sigma^\circ$  measurements taken over islands. The methodology for doing so has been presented, including using rank reduced least-squares for conditioning of the inversion problem and increasing computational efficiency. However, this estimation method leaves estimates strongly dependent on both the size of the islands and the number of singular values used. A simulation was performed not

only to validate the efficacy of the procedure, but also to reveal optimal choice of island size and number of singular values. Finally, results for actual data showed that the procedure works well in practice. While developed for a pencil-beam scatterometer, the basic method can be applied to radiometers [43].

## Chapter 6

### Conclusion

The relative cross-calibration procedure and spatial response function estimation method developed in this thesis may be useful in enabling OSCAT  $\sigma^\circ$  data to extend the SCP data time series. To help maintain consistency among datasets of the SCP, a method of adjusting the  $\sigma^\circ$  response of future conically scanning pencil-beam scatterometers to the nominal incidence angles of QuikSCAT and SeaWinds is presented. The relative cross-calibration procedure provides adjustments to raw  $\sigma^\circ$  data prior to creation of SCP products, or adjustments to apply to SIR image  $\sigma^\circ$  data to simplify SCP product creation. For SCP products requiring knowledge of the spatial response function, estimates of the OSCAT SRF can be obtained by using  $\sigma^\circ$  measurements from multiple passes over an island to invert the scatterometer measurements. Through a simplified model of the true scattering characteristics of an island target, the estimation method is reduced to rank-reduced least-squares. Through simulation, the estimation method is validated, and parameters effecting the accuracy of the method are optimally chosen. A parameterized SRF model is also introduced to improve the utility of SRF estimates in SCP product creation. Application of the parameterized SRF in OSCAT egg SIR image processing results in less noise than the simple approximation currently being used. Finally, LTD processing of OSCAT SIR images is developed to allow better temporal resolution of diurnal variability of the  $\sigma^\circ$  response in polar regions.

#### 6.1 Contributions

The research presented in this thesis makes several contributions in the field of remote sensing. These contributions are summarized in the following sections.

### 6.1.1 Temporal Enhancement of OSCAT SIR Imagery

To facilitate studies of diurnal characteristics of the polar regions, a method of processing SIR images based local time of day is applied to OSCAT. The following contributions are made as a part of this process.

1. The local time of day sampling characteristics of QuikSCAT, SeaWinds, and OSCAT are analyzed in depth to provide for better understanding of LTD SIR image processing.
2. A methodical approach for applying LTD SIR processing to future remote sensing instruments is established. This includes examination of temporal data windows to determine data allocation for LTD SIR images of an instrument based on data coverage, convenience, and relation to other instruments.

### 6.1.2 Relative Cross-calibration Procedure

As an integral part of adaptation of OSCAT for the SCP data time series, a new relative cross-calibration procedure is presented. Contributions resulting from the procedure are as follows.

1. A method for relative calibration of raw  $\sigma^\circ$  data for conically scanning pencil-beam scatterometers over extended-area natural land targets is presented. The method examines the azimuth angle response of  $\sigma^\circ$  over a region that is homogeneous, isotropic, and temporally stable. Doing so allows for evaluation of the stability of the instrument and computation of relative calibration factors to adjust the  $\sigma^\circ$  response of an instrument to the nominal incidence angles of the inner and outer beams of QuikSCAT. A 4th-order Fourier series is used in modeling the azimuth angle response of  $\sigma^\circ$  and correcting measurements.
2. As a part of the relative calibration procedure, further evidence of the diurnal cycle in the Amazon is documented. Relative calibration biases that can result from ignoring diurnal fluctuation are shown to exceed 0.3 dB for Ku-band  $\sigma^\circ$  measurements.
3. A method of extended-area selection is introduced that employs LTD SIR images to account for possible diurnal fluctuation in  $\sigma^\circ$ .

4. A method is presented for adjusting SIR image  $\sigma^\circ$  data of conically scanning pencil-beam scatterometers to the nominal incidence angles of the inner and outer beams of QuikSCAT.
5. Through the use of LTD SIR images in the calibration procedure, a possible diurnal cycle in the interior of Greenland during the boreal winter is observed. Because of poor spatial sampling of OSCAT H-pol data over Greenland, the interior of Greenland is found not to be a suitable calibration site for OSCAT.

### **6.1.3 Scatterometer Spatial Response Function Estimation**

A method of estimating the spatial response function of OSCAT is developed. The following contributions are the result of research in this area.

1. A method for estimating the spatial response function of a pencil-beam scatterometer is developed based on rank-reduced least-squares. The same basic method can be applied to radiometers.
2. The method is applied to OSCAT to obtain estimates of the OSCAT spatial response function for enhancing the utility of the data.
3. A simplified model of the scattering characteristics of island targets is presented.
4. A simulation method is developed that allows for optimum choice of island size and number of significant singular values to minimize error in reconstruction of the spatial response function. Two metrics are introduced for evaluating the performance of the estimation method.
5. Results from performing the simulation with OSCAT provide guidelines for future researchers in selection of island size and significant singular values when implementing this estimation method.

## **6.2 Future Work**

There are several areas for future research in connection with the work presented herein. These are discussed in the following sections.

### 6.2.1 Validation of Calibration Factors

The relative cross-calibration method for raw  $\sigma^\circ$  data was only performed over the Amazon basin. Possible annual fluctuation in the  $\sigma^\circ$  response over the Amazon warrants further validation of the relative calibration factors obtained for raw  $\sigma^\circ$  measurements. Extended-area targets that exhibit minimal annual variation in  $\sigma^\circ$  response are recommended.

Since the interior of Greenland was observed to be an inadequate calibration site for OSCAT, further validation is appropriate for SIR image  $\sigma^\circ$  calibration factors as well. To verify that the calibration factors minimize variability in the SCP data time series, comparison of QuikSCAT and adjusted OSCAT SIR image data should be performed.

### 6.2.2 Diurnal Fluctuation in Greenland

The diurnal fluctuation observed over the interior of Greenland can be investigated further. The particular area over Greenland for which the fluctuation is observed may exhibit azimuthal modulation due to the terrain and snow accumulation. It would be useful to determine whether the fluctuation observed between the different LTD SIR images of OSCAT are due to a diurnal cycle, or azimuth modulation in  $\sigma^\circ$  as a result of limited sampling geometries of OSCAT. This could be approached by analyzing the response of raw  $\sigma^\circ$  data versus azimuth angle over the area.

### 6.2.3 Spatial Response Function Estimation Method Improvement

Improving the robustness of the spatial response function estimation method requires additional research. An example of further research might be applying total least-squares to invert the measurement model instead of least-squares.

### 6.2.4 Further Validation of OSCAT Spatial Response Function Estimates

Though the efficacy of the estimation method was validated for OSCAT through simulation, further validation of the method could be done by applying it to other islands. The OSCAT sampling geometry presents specific limitations in the estimation method that

might not affect other instruments. Attempting the estimation method over additional islands might provide better estimates of the V-pol spatial response function.

### **6.2.5 Validation of Spatial Response Function Estimation Method**

As additional validation of the efficacy of the estimation method, the method could be applied to other remote sensing instruments. Since the spatial response function of QuikSCAT is known, applying the estimation method to QuikSCAT would be especially useful. It would facilitate comparison of the known spatial response function and estimates obtained by the estimation method.

### **6.2.6 Implementation of OSCAT Spatial Response Function Estimates**

The purpose of estimating the spatial response function of OSCAT was to implement in algorithms used in creating products for the SCP database. The scope of this thesis limited implementation of estimates to parameterized estimates of the H-pol spatial response function of OSCAT. Further research could include implementation of the estimated V-pol spatial response function of eggs, and all spatial response function estimates for slices. For slices, this might involve tabulation of the approximate response of the estimates for use in algorithms, as was done for QuikSCAT.



## Bibliography

- [1] W. Wagner, G. Lemoine, and H. Rott, "A method for estimating soil moisture from ERS scatterometer and soil data," *Remote Sensing of Environment*, vol. 70, no. 2, pp. 191–207, 1999. 1
- [2] Z. Bartalis, W. Wagner, V. Naeimi, S. Hasenauer, K. Scipal, H. Bonekamp, J. Figa, and C. Anderson, "Initial soil moisture retrievals from the METOP-A Advanced Scatterometer (ASCAT)," *Geophysical Research Letters*, vol. 34, no. 20, p. L20401, 2007. 1
- [3] V. Naeimi, K. Scipal, Z. Bartalis, S. Hasenauer, and W. Wagner, "An improved soil moisture retrieval algorithm for ERS and METOP scatterometer observations," *IEEE Trans. Geosci. Remote Sens.*, vol. 47, no. 7, pp. 1999–2013, 2009. 1
- [4] F. Gohin and A. Cavanie, "A first try at identification of sea ice using the three beam scatterometer of ERS-1," *REMOTE SENSING*, vol. 15, no. 6, pp. 1221–1228, 1994. 1
- [5] Q. Remund and D. Long, "Sea ice extent mapping using Ku band scatterometer data," *Journal of Geophysical Research*, vol. 104, no. 11, pp. 515–11, 1999. 1
- [6] J. Haarpaintner, R. Tonboe, D. Long, and M. Van Woert, "Automatic detection and validity of the sea-ice edge: an application of enhanced-resolution QuikScat/SeaWinds data," *IEEE Trans. Geosci. Remote Sens.*, vol. 42, no. 7, pp. 1433–1443, 2004. 1
- [7] H. Anderson and D. Long, "Sea ice mapping method for SeaWinds," *IEEE Trans. Geosci. Remote Sens.*, vol. 43, no. 3, pp. 647–657, 2005. 1
- [8] M. Belmonte Rivas and A. Stoffelen, "New Bayesian algorithm for sea ice detection with QuikSCAT," *IEEE Trans. Geosci. Remote Sens.*, no. 99, pp. 1–8, 2011. 1
- [9] K. Stuart and D. Long, "Tracking large tabular icebergs using the SeaWinds Ku-band microwave scatterometer," *Deep Sea Research Part II: Topical Studies in Oceanography*, 2011. 1
- [10] V. Wismann, K. Boehnke, and C. Schmullius, "Global land surface monitoring using the ERS-1 scatterometer," in *IEEE Interna. Geosci. Remote Sens. Symp. (IGARSS)*, vol. 3, 1994, pp. 1488–1490. 1
- [11] D. Long and P. Hardin, "Vegetation studies of the Amazon Basin using enhanced resolution Seasat scatterometer data," *IEEE Trans. Geosci. Remote Sens.*, vol. 32, no. 2, pp. 449–460, 1994. 1, 3, 29

- [12] I. Woodhouse and D. Hoekman, “Tropical forest monitoring using data from the ERS-1 Wind Scatterometer,” in *IEEE Interna. Geosci. Remote Sens. Symp. (IGARSS)*, vol. 2, 1996, pp. 845–847. 1
- [13] C. Emmett, R. Jensen, P. Hardin, and D. Long, “Detecting change in equatorial regions of Brazil using medium resolution satellite imagery,” in *IEEE Interna. Geosci. Remote Sens. Symp. (IGARSS)*, vol. 4, 1997, pp. 1557–1559. 1
- [14] H. Stephen and D. Long, “Multi-spectral analysis of the Amazon Basin using SeaWinds, ERS, Seasat scatterometers, TRMM-PR and SSM/I,” in *IEEE Interna. Geosci. Remote Sens. Symp. (IGARSS)*, vol. 3, 2002, pp. 1780–1782. 1
- [15] R. Lindsley and D. Long, “Estimating Surface Oil Extent from the Deepwater Horizon Oil Spill using ASCAT Backscatter,” in *IEEE Radar Con.*, 2011, pp. 559–563. 1
- [16] W. Liu, “Progress in scatterometer application,” *Journal of Oceanography*, vol. 58, no. 1, pp. 121–136, 2002. 1
- [17] M. Bourassa, H. Bonekamp, P. Chang, D. Chelton, J. Courtney, R. Edson, J. Figa, Y. He, H. Hersbach, K. Hilburn *et al.*, “Remotely sensed winds and wind stresses for marine forecasting and ocean modeling,” *Proceeding, OceanObs’ 09: Sustained Ocean Observations and Information for Society, Venice, Italy*, 2010. 1, 2
- [18] D. Long and B. Hicks, “Standard BYU QuikScat/SeaWinds land/ice image products,” *Internal report, Brigham Young Univ., Provo, UT*, 2000. 2, 115
- [19] D. Long, J. Luke, and W. Plant, “Ultra high resolution wind retrieval for SeaWinds,” in *IEEE Interna. Geosci. Remote Sens. Symp. (IGARSS)*, vol. 2, 2003, pp. 1264–1266. 2
- [20] D. Long, P. Hardin, and P. Whiting, “Resolution enhancement of spaceborne scatterometer data,” *IEEE Trans. Geosci. Remote Sens.*, vol. 31, no. 3, pp. 700–715, 1993. 2
- [21] M. Owen and D. Long, “Land-Contamination Compensation for QuikSCAT Near-Coastal Wind Retrieval,” *IEEE Trans. Geosci. Remote Sens.*, vol. 47, no. 3, pp. 839–850, 2009. 2
- [22] M. Owen, K. Stuart, and D. Long, “Ultra-high-resolution near-coastal wind retrieval for QuikSCAT,” *Proc. SPIE (Coast. Ocean Remote Sens.)*, vol. 6680, 2007. 2
- [23] K. Stuart and D. Long, “Iceberg size and orientation estimation using SeaWinds,” in *IEEE Interna. Geosci. Remote Sens. Symp. (IGARSS)*, 2010, pp. 2394–2397. 2
- [24] I. Ashcraft and D. Long, “The spatial response function of SeaWinds backscatter measurements,” in *Proceedings of SPIE*, vol. 5151, 2003, pp. 609–618. 2, 9, 60
- [25] R. Kennett and F. Li, “Seasat over-land scatterometer data. II. Selection of extended area and land-target sites for the calibration of spaceborne scatterometers,” *IEEE Trans. Geosci. Remote Sens.*, vol. 27, no. 6, pp. 779–788, 1989. 2, 3, 6

- [26] I. Birrer, E. Bracalente, G. Dome, J. Sweet, and G. Berthold, “ $\sigma^0$  Signature of the Amazon Rain Forest Obtained from the Seasat Scatterometer,” *IEEE Trans. Geosci. Remote Sens.*, vol. 20, no. 1, pp. 11–17, 1982. 2, 3, 6, 29
- [27] L. Kunz and D. Long, “Calibrating SeaWinds and QuikSCAT scatterometers using natural land targets,” *IEEE Geosci. Remote Sens. Letters*, vol. 2, no. 2, pp. 182–186, 2005. 2, 3, 6, 7, 8, 30, 50
- [28] D. Long and G. Skouson, “Calibration of spaceborne scatterometers using tropical rain forests,” *IEEE Trans. Geosci. Remote Sens.*, vol. 34, no. 2, pp. 413–424, 2002. 2, 3, 6, 30
- [29] W. Tsai, J. Graf, C. Winn, J. Huddleston, S. Dunbar, M. Freilich, F. Wentz, D. Long, and W. Jones, “Postlaunch sensor verification and calibration of the NASA Scatterometer,” *IEEE Trans. Geosci. Remote Sens.*, vol. 37, no. 3, pp. 1517–1542, 1999. 3, 6, 7
- [30] E. Bracalente and J. Sweet, *Analysis of normalized radar cross section signature of Amazon rain forest using Seasat scatterometer data*. National Aeronautics and Space Administration, Scientific and Technical Information Branch, 1984, vol. 85779. 3, 7, 29
- [31] B. Hicks and D. Long, “Improving Temporal Resolution of SIR Images Tandem Mission Data in the Polar Regions,” *Internal report, Brigham Young Univ., Provo, UT*, 2005. 3, 15, 16, 29
- [32] P. Yoho, A. Anderson, D. Long, J. Lux, J. Adams, and F. Cheng, “SeaWinds on QuikSCAT calibration using a calibration ground station,” in *IEEE Interna. Geosci. Remote Sens. Symp. (IGARSS)*, vol. 3, 2000, pp. 1039–1041. 6
- [33] J. Zec, W. Jones, and D. Long, “SeaWinds beam and slice balance using data over Amazonian rainforest,” in *IEEE Interna. Geosci. Remote Sens. Symp. (IGARSS)*, vol. 5, 2000, pp. 2215–2217. 6, 8
- [34] R. Kennett and F. Li, “Seasat over-land scatterometer data. I. Global overview of the Ku-band backscatterer coefficients,” *IEEE Trans. Geosci. Remote Sens.*, vol. 27, no. 5, pp. 592–605, 1989. 7
- [35] K. Padia and S. D. Team, “Oceansat-2 Scatterometer algorithms for sigma-0, processing and products format,” *Advanced Image Processing Group, Signal and Image Processing Area, Space Applications Centre, Gujarat, India*, 2010. 8, 9, 10, 60, 61
- [36] D. Long, M. Drinkwater, B. Holt, S. Saatchi, and C. Bertoia, “Global ice and land climate studies using scatterometer image data,” *EOS, Transaction of the American Geophysical Union*, vol. 82, pp. 503–503, 2001. 11
- [37] E. S. A. BYU Center for Remote Sensing, NASA Jet Propulsion Laboratory, “Scatterometer Climate Record Pathfinder,” <http://www.scp.byu.edu>, September 2011. 12

- [38] D. Early and D. Long, "Image reconstruction and enhanced resolution imaging from irregular samples," *IEEE Trans. Geosci. Remote Sens.*, vol. 39, no. 2, pp. 291–302, 2001. 13
- [39] B. Gunn, "Temporal Resolution Enhancement for AMSR Images," *Internal report, Brigham Young Univ., Provo, UT*, 2007. 15
- [40] R. Lindsley and D. Long, "Local Time of Day Processing with ASCAT," *Internal report, Brigham Young Univ., Provo, UT*, 2010. 15
- [41] B. Hicks, "Melt detection and estimation in greenland using tandem quikscat and sea-winds scatterometers," *Masters Thesis, Brigham Young Univ., Provo, UT*, 2006. 29
- [42] T. Moon and W. Stirling, *Mathematical methods and algorithms for signal processing*. Prentice Hall, New York, 2000, vol. 13. 65
- [43] B. Gunn, "Scatterometer Image Reconstruction Tuning and Aperture Function Estimation for the Advanced Microwave Scanning Radiometer Aboard the Earth Observing System," *Masters Thesis, Brigham Young Univ., Provo, UT*, 2010. 84
- [44] I. Ashcraft, "Projecting an Arbitrary Latitude and Longitude onto a Tangent Plane," *Internal report, Brigham Young Univ., Provo, UT*, 1999. 116

## Appendix A

### Acronyms, Nomenclature, and Indicators

#### Acronymns

QuikSCAT	Quick Scatterometer
OSCAT	Oceansat-2 Scatterometer
JPL	Jet Propulsion Laboratory
ISRO	Indian Science Research Organisation
SCP	Scatterometer Climate Record Pathfinder
SIR	Scatterometer image reconstruction
SRF	Spatial response function
L1B	JPL and ISRO raw $\sigma^\circ$ data
UHR Winds	Ultra-high resolution wind retrieval
LFM	Linear frequency modulation
PRF	Pulse repetition frequency
SASS	Seasat Scatterometer
ESA	European Space Agency
ERS	Earth Remote Sensing
NSCAT	NASA Scatterometer
ASCAT	Advanced Scatterometer
AMSR	Something
ERI	Enhanced resolution imaging
UTC	Coordinated Universal Time
LTD	Local time of day
NHe	Northern hemisphere
SHe	Southern hemisphere
JD	Julian day
RMS	Root mean square
SNR	Signal-to-noise ratio
SCR	Signal-to-clutter ratio
SVD	Singular value decomposition

#### Nomenclature

$\sigma$	Radar cross-section
$\sigma^\circ$	Normalized radar backscatter (cross-section)
$\bar{\sigma}^\circ$	Spatially averaged normalized radar backscatter (cross-section)
$z$	Measured value of spatially averaged normalized radar backscatter
$P_r$	Received signal power

$P_b$	Signal power component due to backscatter
$P_n$	Signal power component due to noise
$P_t$	Transmit signal power
$\lambda$	Wavelength of transmit signal
$Q$	Antenna gain
$r$	Range to target (km)
$A$	Area of the Earth's surface illuminated by the antenna
$X$	Radar calibration parameter
$\phi$	Measurement azimuth angle – angle referenced clockwise from North to the vector pointing from the satellite to the measurement center location in the ground plane (also equivalent to the rotation of the SRF on the Earth's surface)
$\theta$	Measurement incidence angle
$\Theta$	Nominal incidence angle (or reference incidence angle) of the spatial response function on the surface of the Earth)
$\mathcal{A}$	Coefficient of linear regression model for incidence angle dependence of $\sigma^\circ$ that represents the DC component
$\mathcal{B}$	Coefficient of linear regression model for incidence angle dependence of $\sigma^\circ$ that represents the slope of $\sigma^\circ$ versus incidence angle
$f_{\sigma^\circ}(\sigma^\circ)$	Distribution of $\sigma^\circ$ measurements
$\alpha$	Typical value of $\sigma^\circ$ over a local region of the Earth
$\mathbf{s}$	Vector of azimuthally modulated $\sigma^\circ$ measurements
$J$	A matrix used in $\sigma^\circ$ azimuth modulation estimation
$\mathbf{c}$	Vector of Fourier series coefficients that describe the azimuth modulation of $\sigma^\circ$
$\mu$	Sample mean of $\sigma^\circ$ measurements
$\varsigma$	Sample standard deviation of $\sigma^\circ$ measurements
$\beta$	Relative calibration factor for $\sigma^\circ$ measurements
$\vec{\nu}$	Represents a suitably defined coordinate system
$N$	Measurement noise
$\eta$	Unit variance, zero-mean gaussian random variable
$K_p$	Normalized standard deviation of echo return energy
$h$	Spatial response function
$\mathbf{h}$	Discretized spatial response function
$\hat{\mathbf{h}}_{\text{LS}}$	Least-squares estimate of the SRF
$\hat{\mathbf{h}}_{\text{SVD}}$	Rank-reduced least-squares estimate of the SRF
$\hat{\mathbf{h}}_{\text{Par}}$	Parameterized least-squares estimate of the SRF
$\vec{x}$	Center location of the SRF on the surface of the Earth
$\Delta\nu$	Discrete area of a grid element
$S$	Discretized $\sigma^\circ$ over a localized region of the Earth's surface
$G$	A matrix used in SRF estimation with rows consisting of discretized samples of the $\sigma^\circ$ over a localized region of the Earth's surface
$\mathbf{e}$	Vector of measurement noise – referred to as error in $z$
$\mathbb{R}$	Real space

$\xi$	Singular values of $G$
$U$	Unitary matrix used in the SVD
$\Sigma$	Diagonal matrix with singular values of $G$ down the diagonal – used in the SVD
$V$	Unitary matrix used in the SVD
$\zeta$	Azimuth angle of the antenna beam dimensions
$\psi$	Elevation angle of the antenna beam dimensions
$\Psi$	Number of grid elements contained within the main lobe of the SRF
$R$	A matrix used in parameterized SRF estimation
$\mathbf{b}$	Vector of spatially varying 2nd-order polynomial coefficients that describe the SRF
$B_\Psi$	A diagonal matrix of normalized scaling factors to account for the area of each grid element – used in parameterized estimation of the SRF
$\gamma$	Island area to SRF area ratio
$L$	Number of significant singular values
$B_3$	Mean 3 dB beamwidth
$\epsilon$	The absolute difference in mean 3 dB beamwidth of the simulated SRF and its estimates
$\delta$	RMS reconstruction error

### Subscripts, superscripts, and other indicators

$\hat{[ ]}$	indicates $[ ]$ is an estimated quantity
$\vec{[ ]}$	indicates $[ ]$ is a position vector
$[ ]^\dagger$	indicates the pseudo inverse of $[ ]$
$\tilde{[ ]}$	indicates the rank-reduced approximation of $[ ]$
$[ ]_\Psi$	indicates $[ ]$ is restricted to elements spatially contained within the main lobe of the spatial response function
$[ ]_i$	indicates the island components of $[ ]$ when $[ ]$ is a matrix
$[ ]_o$	indicates the ocean components of $[ ]$ when $[ ]$ is a matrix
$[ ]$	indicates $[ ]$ is a vector quantity



## Appendix B

### Relative Cross-calibration of 2009 Raw Data

The relative cross-calibration of raw  $\sigma^\circ$  measurements for the overlapping days of QuikSCAT and OSCAT is documented in this appendix. The calibration procedure is performed as outlined in Chapter 4 except that raw  $\sigma^\circ$  measurements are taken from L1B data corresponding to JD 309-327 of 2009 for both QuikSCAT and OSCAT. The OSCAT L1B data of this time period is from the initial data processing algorithms employed by ISRO. Many inconsistencies exist in the data, including anisotropic azimuth angle response, incorrect overall incidence angle response, and poor quality  $\sigma^\circ$ . All figures shown herein have the same format as in Chapter 4. The incidence angle response of the data is discussed in Section B.1, while the azimuth angle response is discussed in Section B.2. The  $\sigma^\circ$  measurement statistics are analyzed in Section B.3, and a summary is given in Section B.4.

#### B.1 Incidence Resonse

The combined pass  $\sigma^\circ$  versus  $\theta$  response for the selected mask area of Figure 4.4 is shown for eggs and slices in Figures B.1 and B.2, respectively. Compared with the most recent OSCAT data, this data has a much narrower incidence angle range for egg measurements. There is also a larger volume of low  $\sigma^\circ$  values that are indicative of poor quality in the  $\sigma^\circ$  measurements. The incidence angle response of slice  $\sigma^\circ$  measurements is estimated and removed before further processing.

Similar plots for the ascending and descending pass data are found in Figures B.3 and B.4, respectively. By examining the plots, both the initial version and the most recent version of the OSCAT data exhibit a positive linear relationship between  $\sigma^\circ$  and  $\theta$  in slice measurements. This remains to be an area of potential improvement.

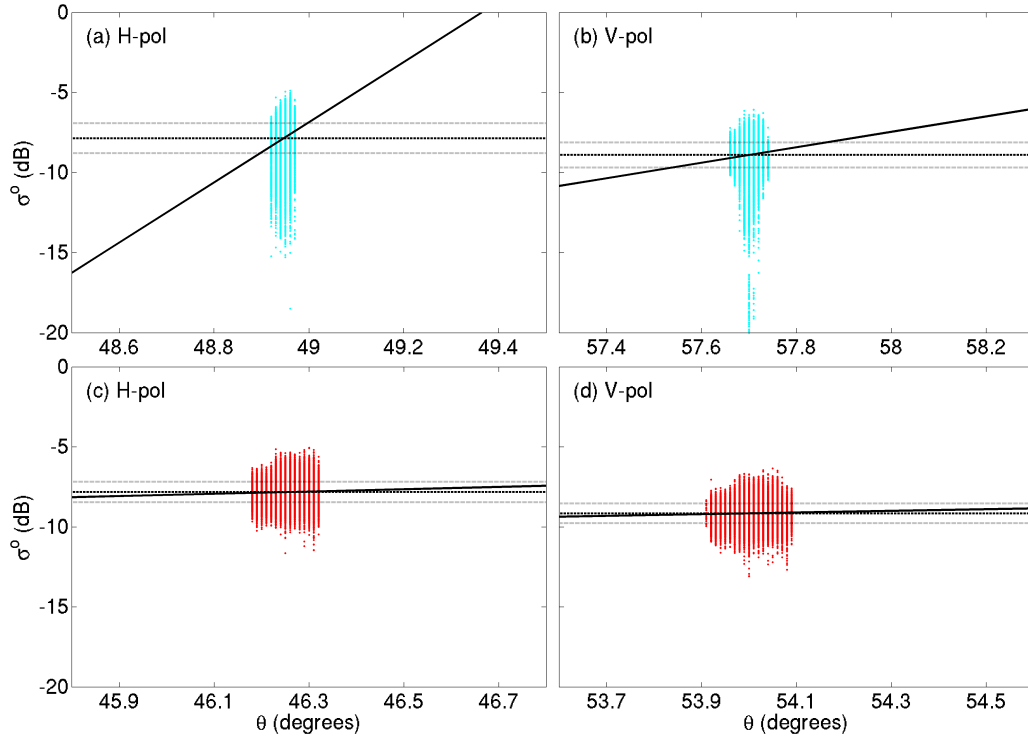


**Figure B.1:** Scatterplots of egg  $\sigma^{\circ}$  versus  $\theta$  for ascending and combined pass data of OSCAT (a) H-pol and (b) V-pol, and QuikSCAT (c) H-pol and (d) V-pol.

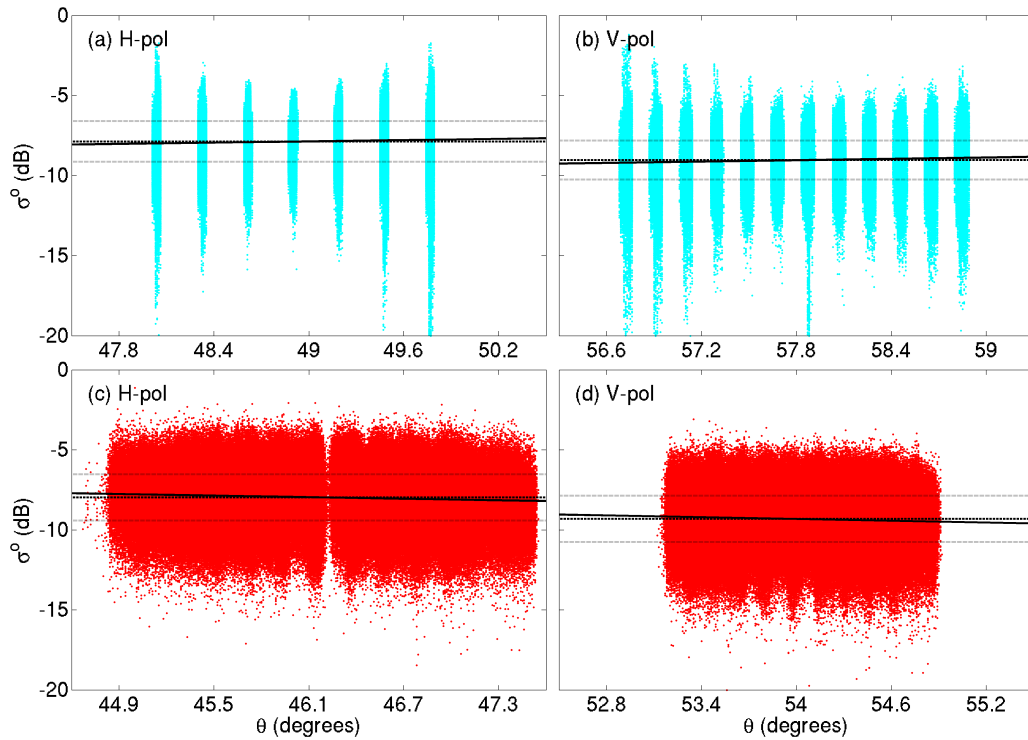


**Figure B.2:** Scatterplots of slice  $\sigma^{\circ}$  versus  $\theta$  for ascending and combined pass data of OSCAT (a) H-pol and (b) V-pol, and QuikSCAT (c) H-pol and (d) V-pol.

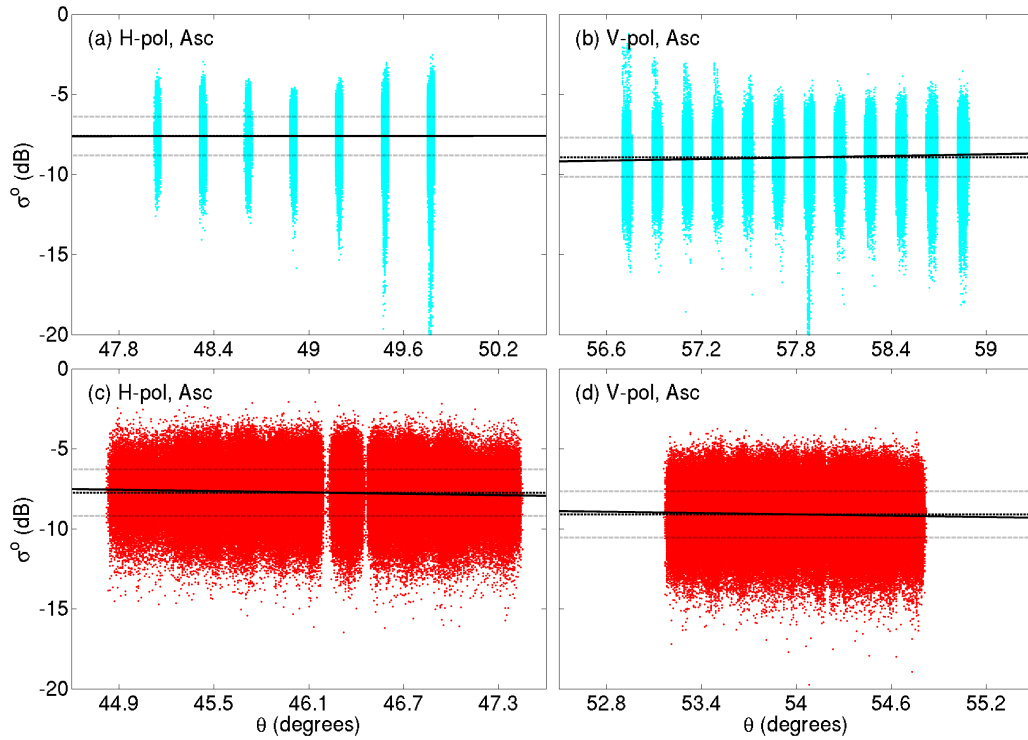


**Figure B.3:** Scatterplots of slice  $\sigma^\circ$  versus  $\theta$  for ascending pass data of OSCAT (a) H-pol and (b) V-pol, and QuikSCAT (c) H-pol and (d) V-pol.

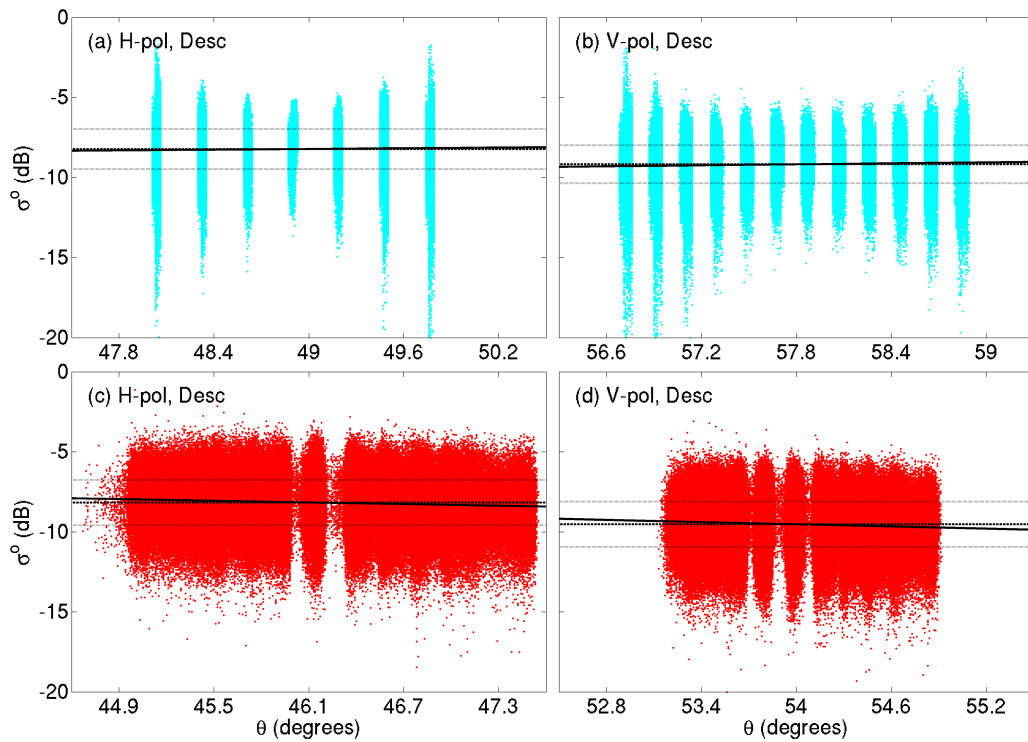


**Figure B.4:** Scatterplots of slice  $\sigma^\circ$  versus  $\theta$  for descending pass data of OSCAT (a) H-pol and (b) V-pol, and QuikSCAT (c) H-pol and (d) V-pol.

## B.2 Azimuth Response

The ascending and descending pass combined  $\sigma^\circ$  versus  $\phi$  response for the selected area is shown for egg measurements and  $\theta$  normalized slice measurements in Figures B.5 and B.6, respectively. For this initial version of OSCAT data, there are extreme inconsistencies in the  $\phi$  response of  $\sigma^\circ$  for both H- and V-pol. The H-pol  $\sigma^\circ$  response exhibits a significant anisotropic nature, while the quality of both H- and V-pol  $\sigma^\circ$  measurements tend to degrade drastically around  $\phi = -100^\circ$ . This represents a potential reduction in the accuracy of the data in scientific studies. As in Chapter 4, the measurements are normalized by estimates of their  $\phi$  response. The same fourth-order Fourier series fit is used to estimate the  $\phi$  response. Azimuth angle-normalized measurements of ascending and descending combined passes are shown in plots of  $\sigma^\circ$  versus  $\phi$  for eggs and slices in Figures B.7 and B.8, respectively.

Figures B.9-B.12 show plots of  $\sigma^\circ$  versus  $\phi$  separately for ascending and descending egg measurements before and after  $\phi$  normalization. Figures B.13-B.16 show plots of  $\sigma^\circ$  versus  $\phi$  separately for ascending and descending slice measurements before and after  $\phi$  normalization. Interestingly, the degradation in  $\sigma^\circ$  at  $\phi = -100^\circ$  only shows up in ascending pass measurements. There also seems to be certain bands of  $\phi$  that exhibit more or less variability. This is visible in the  $\sigma^\circ$  versus  $\phi$  response of descending pass slice measurements in Figures B.15 and B.16. These bands potentially correspond to the left and right sides of the aircraft.

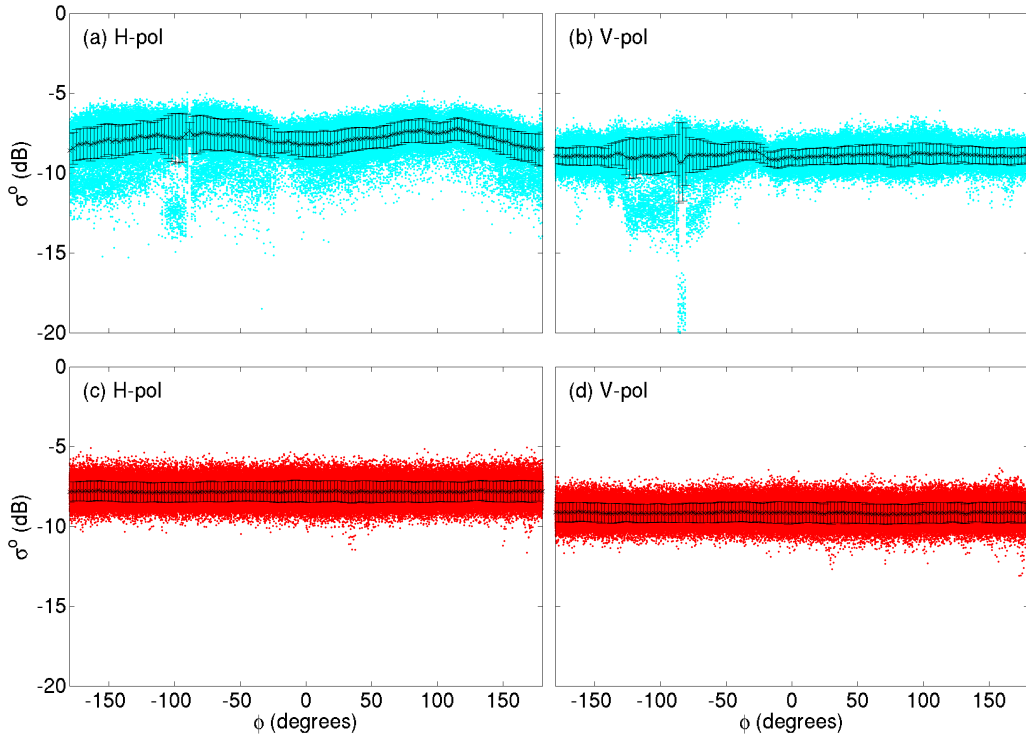


**Figure B.5:** Scatterplots of egg  $\sigma^{\circ}$  versus  $\phi$  for combined pass data of OSCAT (a) H-pol and (b) V-pol, and QuikSCAT (c) H-pol and (d) V-pol.

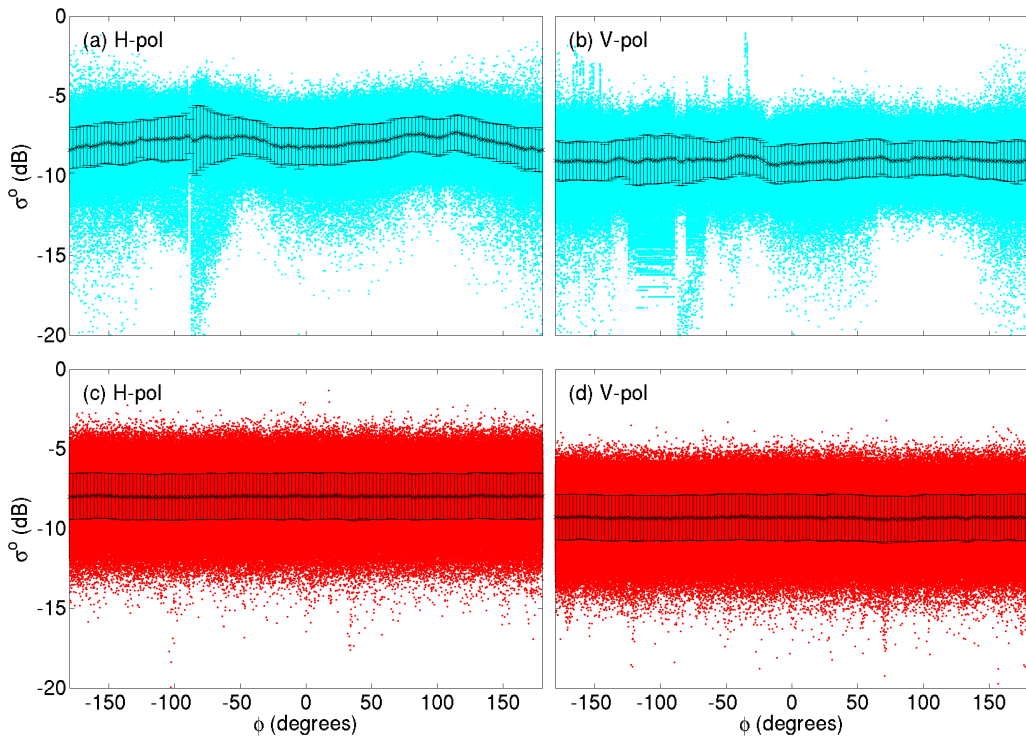


**Figure B.6:** Scatterplots of  $\theta$  normalized slice  $\sigma^{\circ}$  versus  $\phi$  for combined pass data of OSCAT (a) H-pol and (b) V-pol, and QuikSCAT (c) H-pol and (d) V-pol.

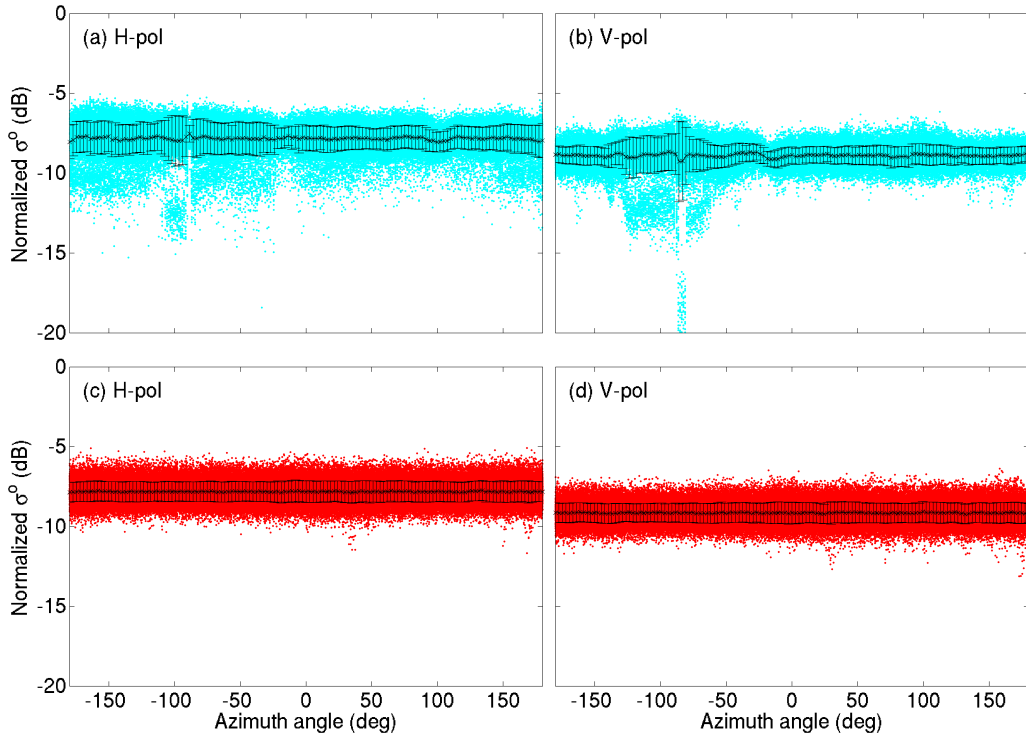


**Figure B.7:** Scatterplots of  $\phi$  normalized egg  $\sigma^\circ$  versus  $\phi$  for combined pass data of OSCAT (a) H-pol and (b) V-pol, and QuikSCAT (c) H-pol and (d) V-pol.

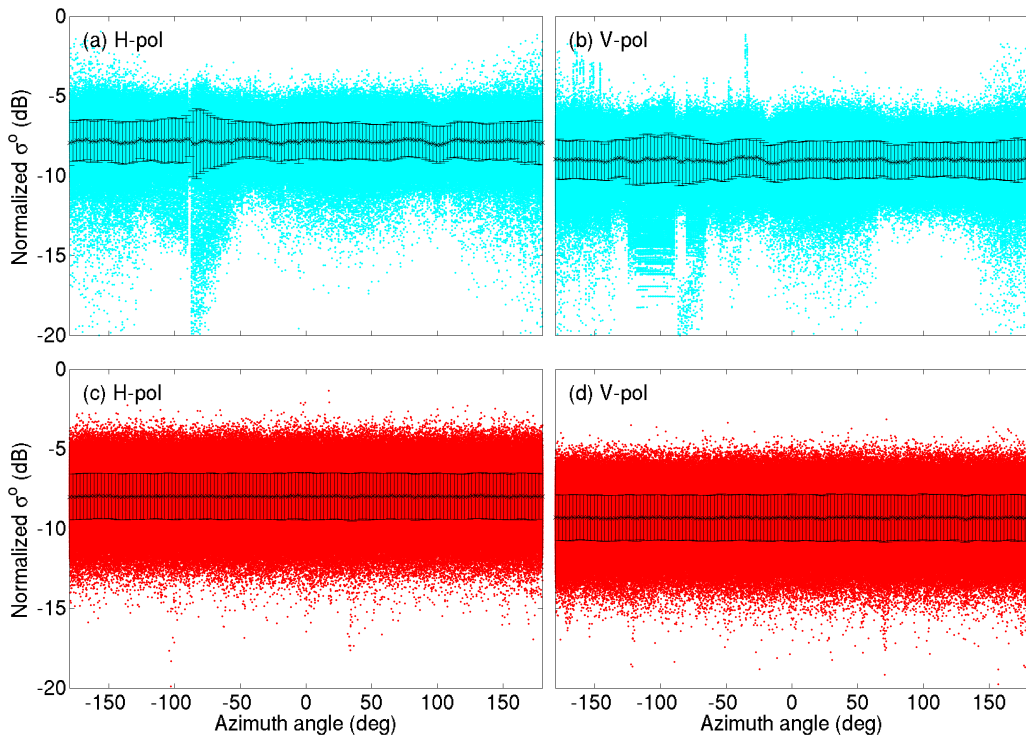


**Figure B.8:** Scatterplots of  $\theta$  and  $\phi$  normalized slice  $\sigma^\circ$  versus  $\phi$  for combined pass data of OSCAT (a) H-pol and (b) V-pol, and QuikSCAT (c) H-pol and (d) V-pol.

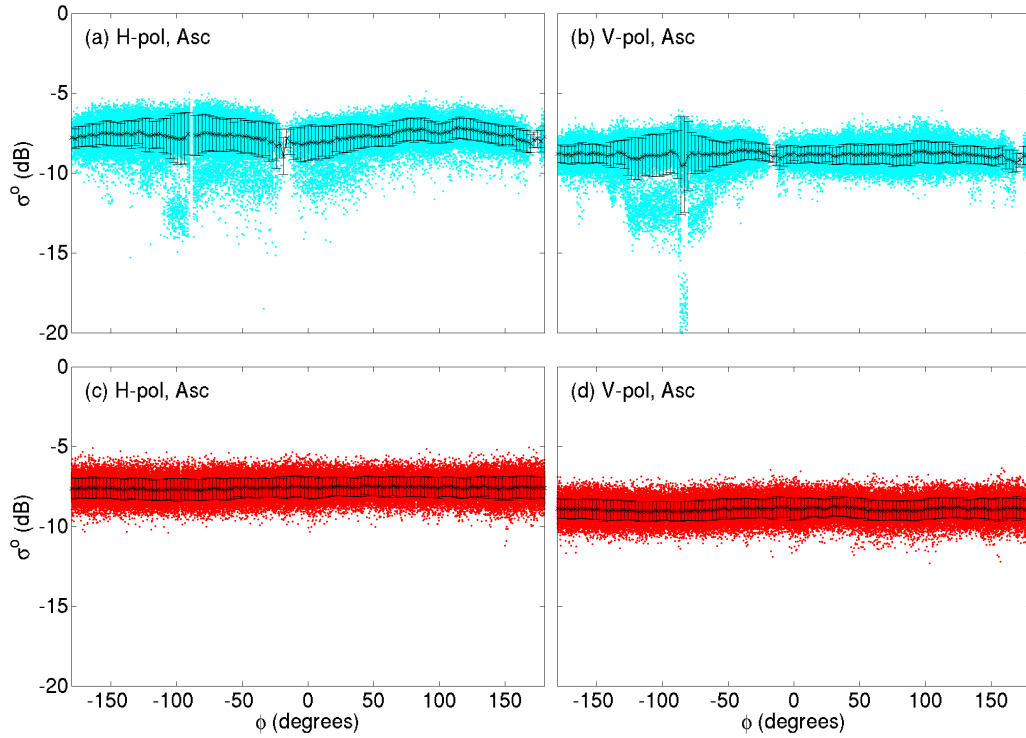


**Figure B.9:** Scatterplots of egg  $\sigma^{\circ}$  versus  $\phi$  for ascending pass data of OSCAT (a) H-pol and (b) V-pol, and QuikSCAT (c) H-pol and (d) V-pol.

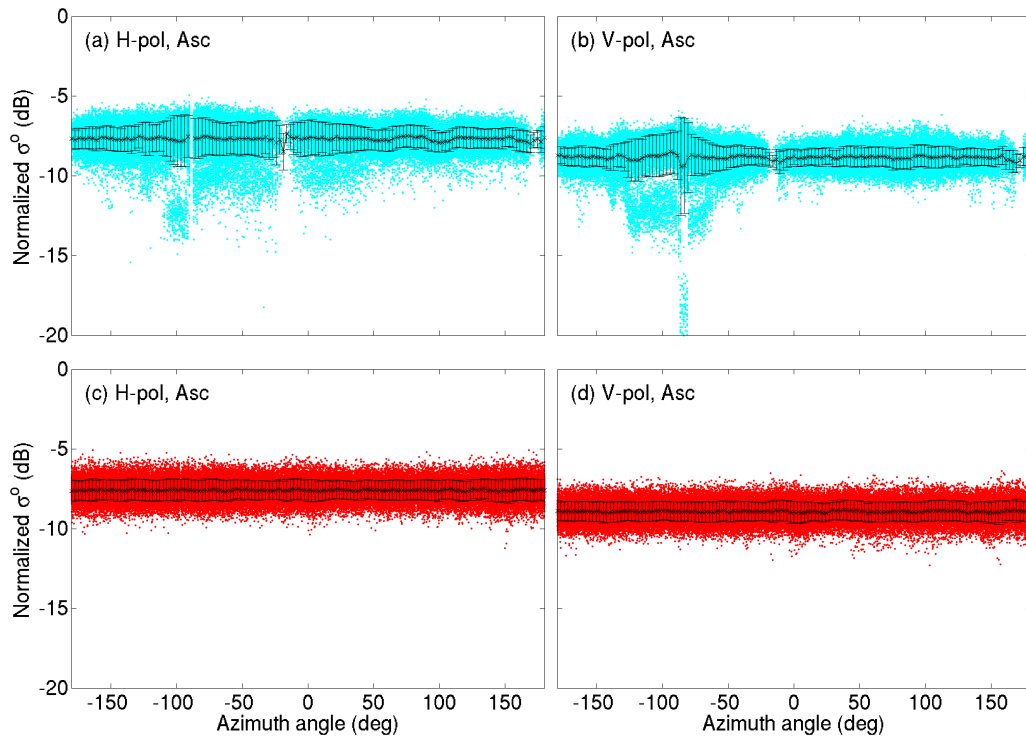


**Figure B.10:** Scatterplots of  $\phi$  normalized egg  $\sigma^{\circ}$  versus  $\phi$  for ascending pass data of OSCAT (a) H-pol and (b) V-pol, and QuikSCAT (c) H-pol and (d) V-pol.

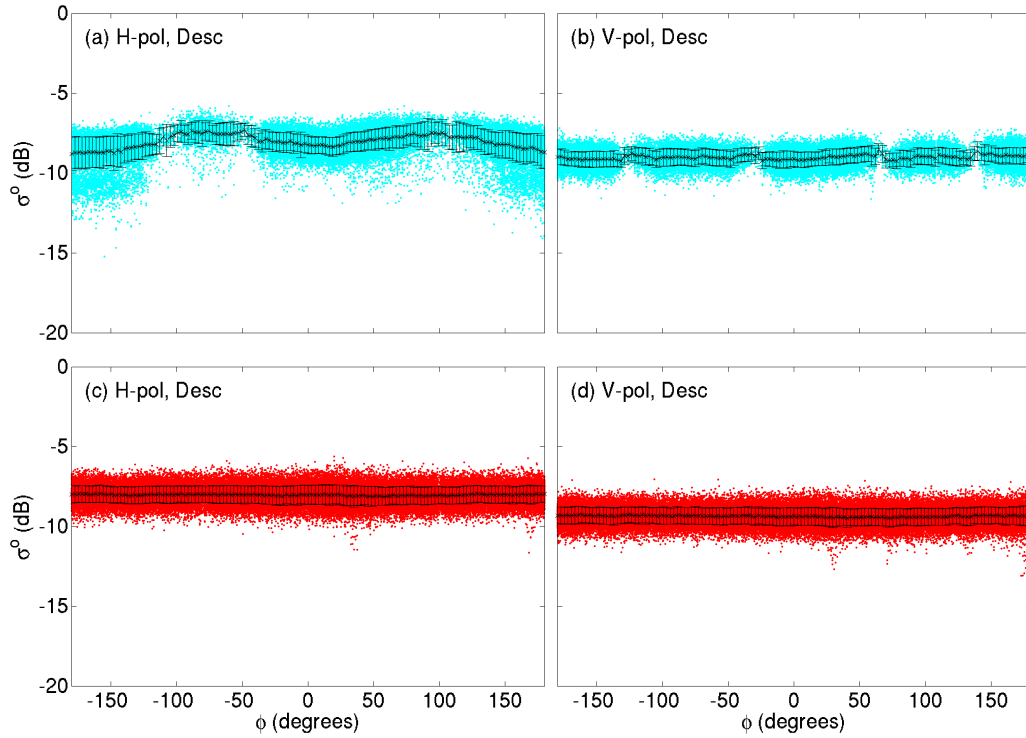


**Figure B.11:** Scatterplots of egg  $\sigma^o$  versus  $\phi$  for descending pass data of OSCAT (a) H-pol and (b) V-pol, and QuikSCAT (c) H-pol and (d) V-pol.

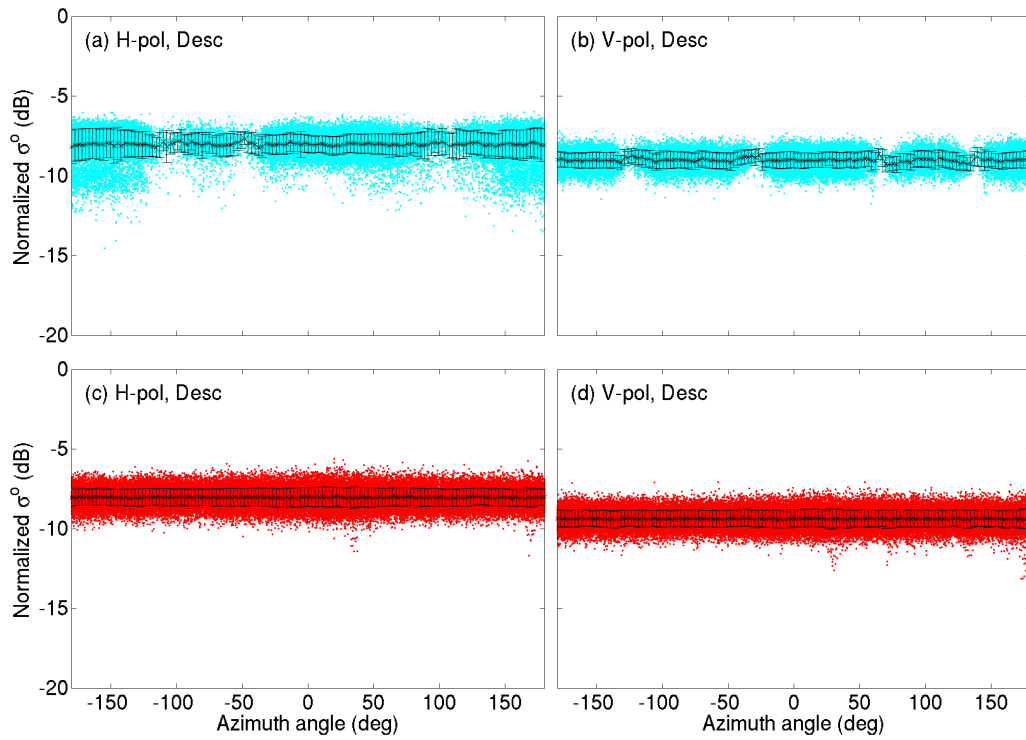


**Figure B.12:** Scatterplots of  $\phi$  normalized egg  $\sigma^o$  versus  $\phi$  for descending pass data of OSCAT (a) H-pol and (b) V-pol, and QuikSCAT (c) H-pol and (d) V-pol.

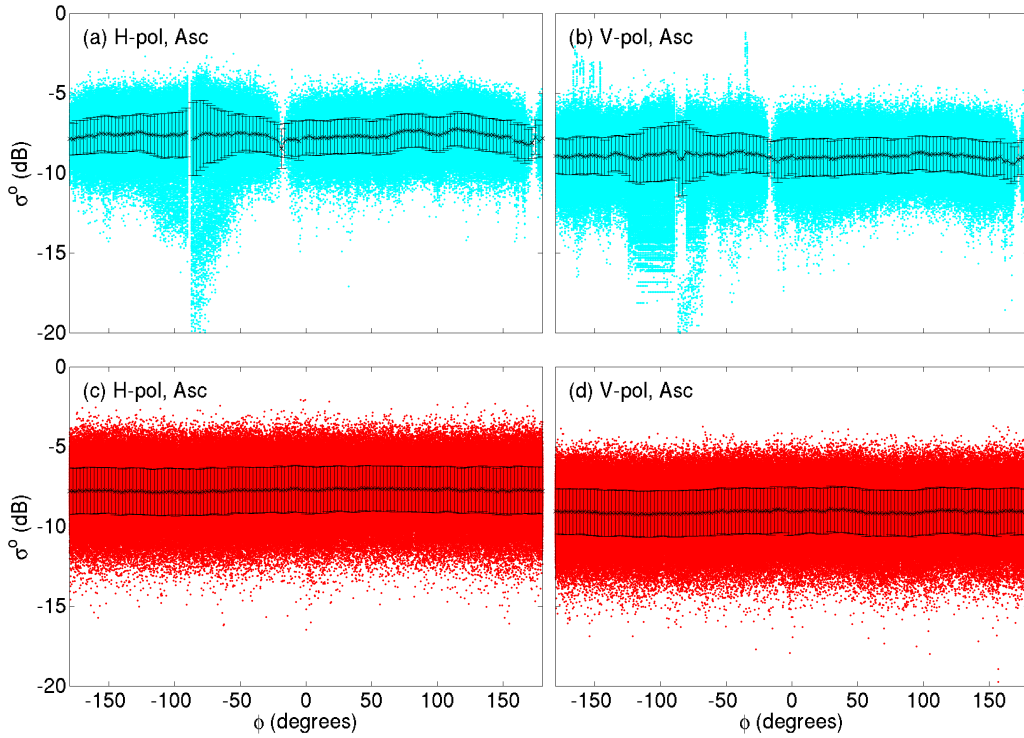


**Figure B.13:** Scatterplots of  $\theta$  normalized slice  $\sigma^\circ$  versus  $\phi$  for ascending pass data of OSCAT (a) H-pol and (b) V-pol, and QuikSCAT (c) H-pol and (d) V-pol.

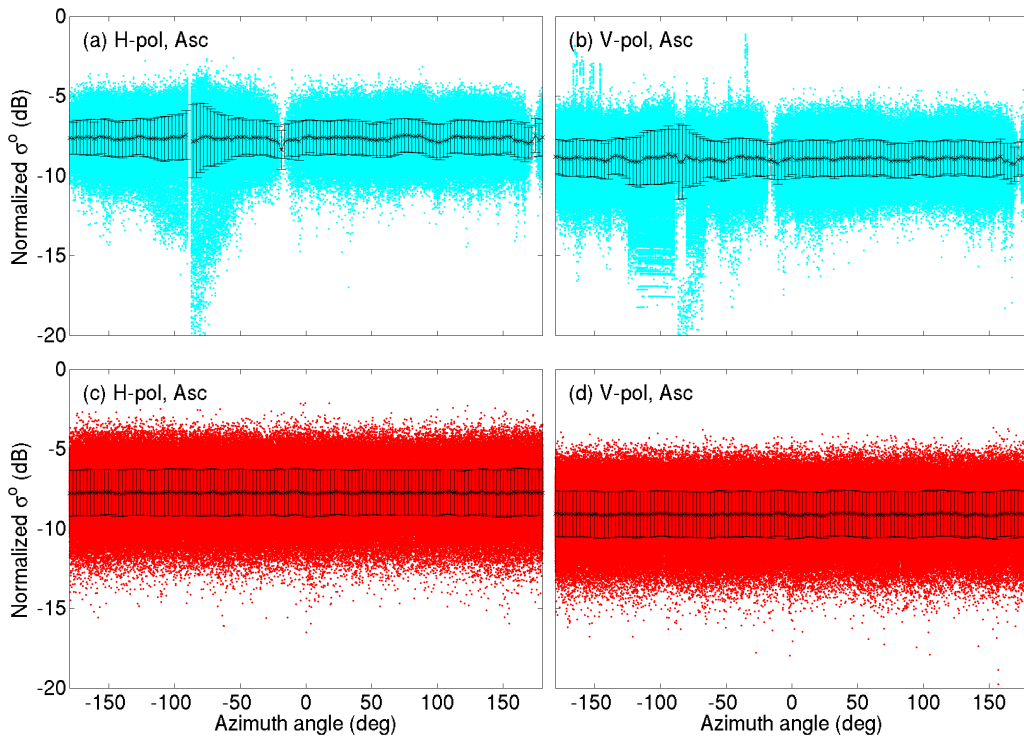


**Figure B.14:** Scatterplots of  $\theta$  and  $\phi$  normalized slice  $\sigma^\circ$  versus  $\phi$  for ascending pass data of OSCAT (a) H-pol and (b) V-pol, and QuikSCAT (c) H-pol and (d) V-pol.

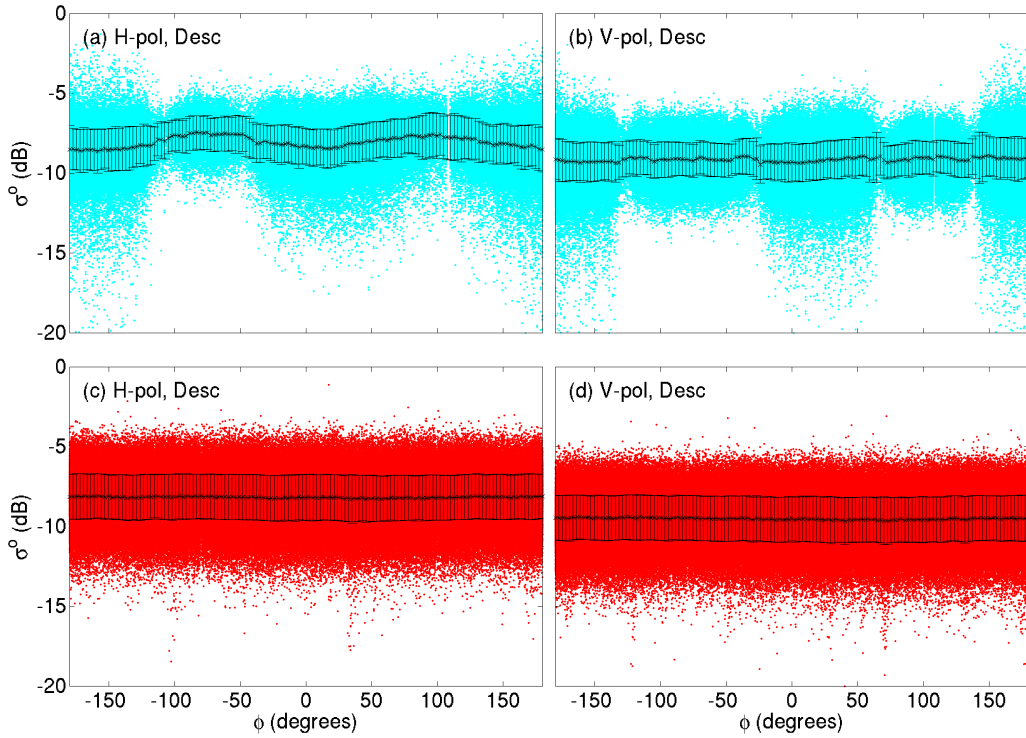


**Figure B.15:** Scatterplots of  $\theta$  normalized slice  $\sigma^\circ$  versus  $\phi$  for descending pass data of OSCAT (a) H-pol and (b) V-pol, and QuikSCAT (c) H-pol and (d) V-pol.

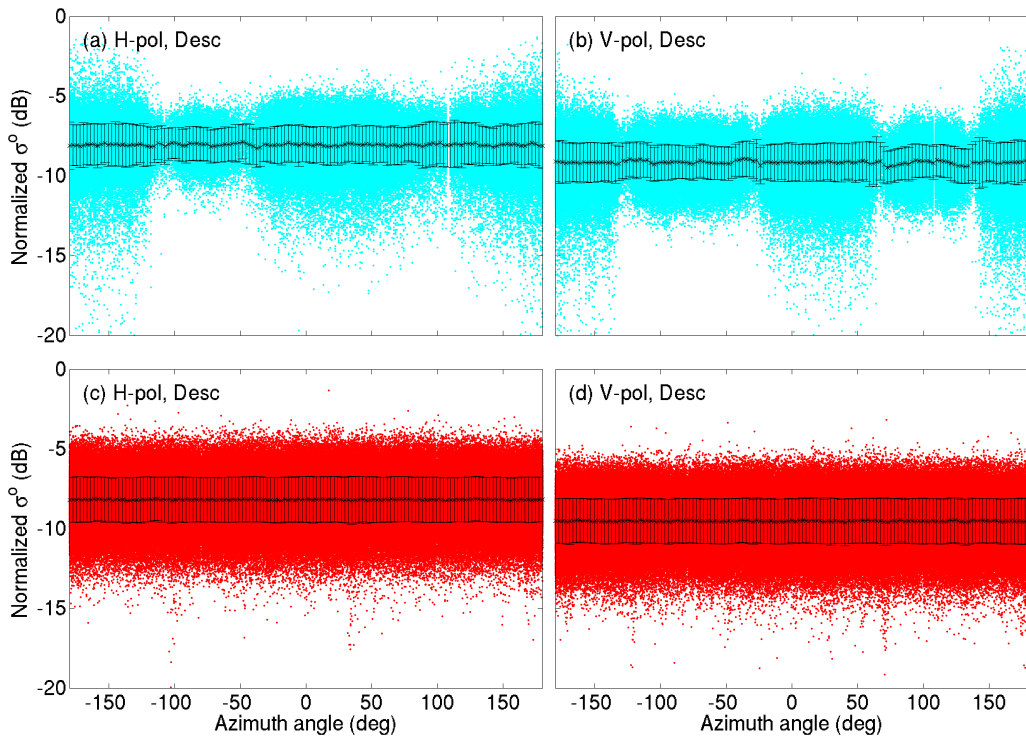


**Figure B.16:** Scatterplots of  $\theta$  and  $\phi$  normalized slice  $\sigma^\circ$  versus  $\phi$  for descending pass data of OSCAT (a) H-pol and (b) V-pol, and QuikSCAT (c) H-pol and (d) V-pol.

**Table B.1:** Relative calibration factors  $\beta_h$  and  $\beta_v$  for  $\sigma^\circ$  of OSCAT egg and slice measurements for ascending, descending, and combined passes.

Type	Satellite Pass	$\beta_h$	$\beta_v$
Egg	Ascending	-0.08	-0.10
	Descending	-0.01	-0.35
	Combined	0.01	-0.26
Slice	Ascending	-0.11	-0.18
	Descending	-0.13	-0.37
	Combined	-0.14	-0.30

### B.3 Data Analysis

The measurement statistics are computed with the normalized  $\sigma^\circ$  measurements. Figure B.17 shows  $f_{\sigma^\circ}(\sigma^\circ)$  for egg measurements with corresponding values of  $\mu_{\text{pol}}$  and  $\varsigma_{\text{pol}}$ , and Figure B.18 shows  $f_{\sigma^\circ}(\sigma^\circ)$  for slice measurements with corresponding values of  $\mu_{\text{pol}}$  and  $\varsigma_{\text{pol}}$ . The calculated values of  $\beta_h$  and  $\beta_v$  are given in Table B.1. These values for the calibration share no resemblance to the values of  $\beta_h$  and  $\beta_v$  calculated with the most recent version of L1B data in Chapter 4.

Plots of  $\sigma^\circ$  measurements as a function of LTD are especially useful for showing inconsistencies of the data. These plots are shown in Figure 4.24 for H- and V-pol. There should not be a significant difference between mean  $\sigma^\circ$  responses at the differing observation LTD of OSCAT. However, in this initial version of the L1B data, there appears to be some variability between the  $\sigma^\circ$  responses at differing observation LTD. Even more significant is the fact that the mean  $\sigma^\circ$  response of OSCAT is greater than that of the descending pass of QuikSCAT for both H- and V-pol. This is in direct opposition to the natural tendency of radar backscatter to decrease with increasing  $\theta$ .

Choosing the descending pass-based relative calibration factors yields  $\beta_h = -0.01$  and  $\beta_v = -0.35$  for egg measurements, and  $\beta_h = -0.13$  and  $\beta_v = -0.37$  for slice measurements. Figure B.20 shows the  $\sigma^\circ$  versus LTD response for OSCAT and QuikSCAT egg measurements after adjusting OSCAT data by the calibration factors. Corresponding plots of slice measurements look similar.

The abnormalities of the  $\theta$  response of OSCAT  $\sigma^\circ$  are even more striking when analyzed collectively across all beams. Measurements of  $\sigma^\circ$  from all beams of both instruments are plotted collectively versus  $\theta$  for ascending and descending combined pass data in Figure B.21 and descending pass data in Figure B.22.

### B.4 Summary

The relative calibration factors computed in this appendix for the 2009 overlap L1B data of OSCAT are not applicable to future data. However, until ISRO retroactively applies the new data processing algorithms to the entire mission dataset, these factors are applicable to OSCAT L1B data from JD 309 of 2009 through JD 120 of 2010.

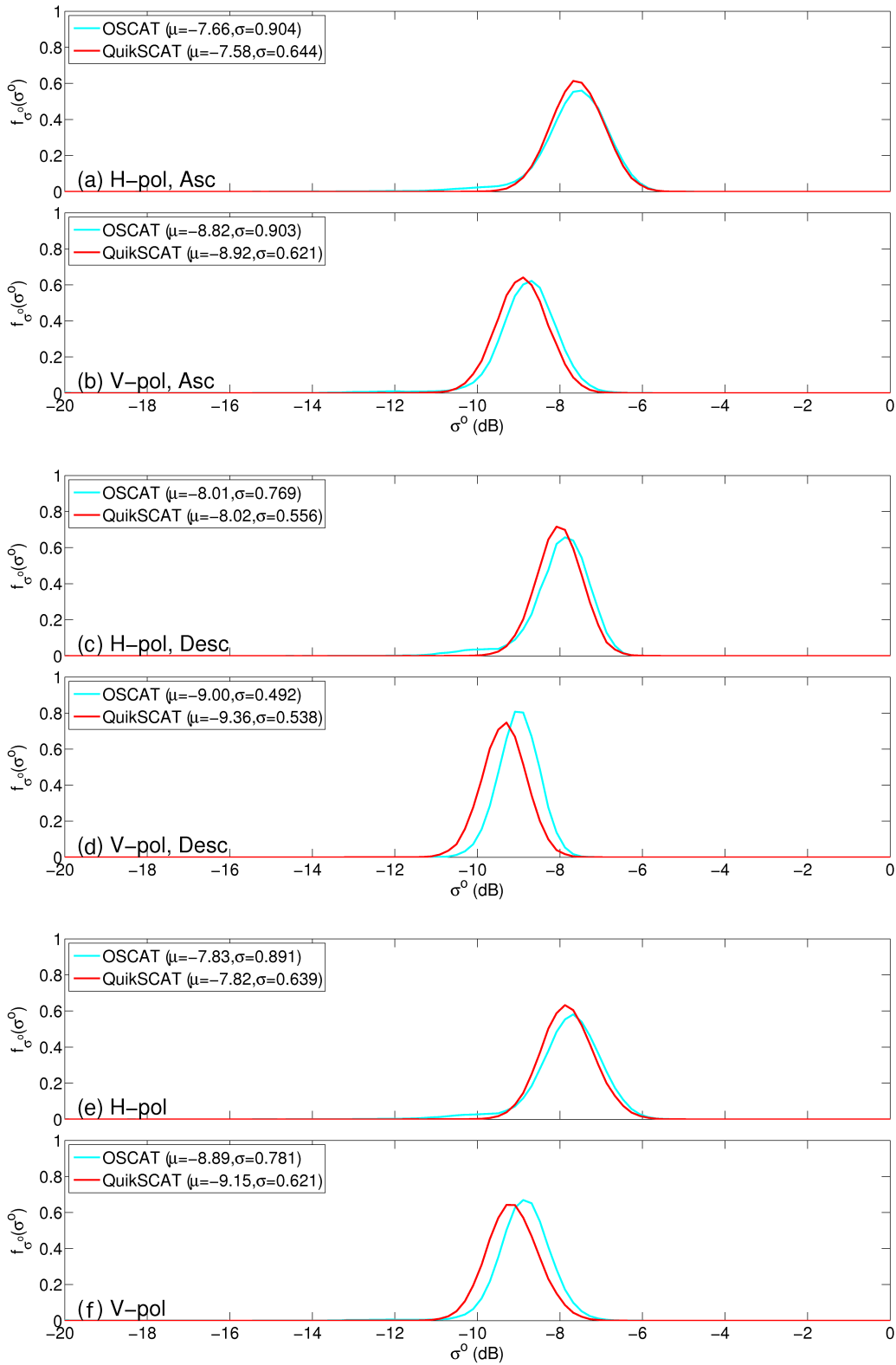


**Figure B.17:** Plots of measurement distribution  $f_{\sigma^0}(\sigma^0)$  for normalized H- and V-pol egg measurements of the (a)-(b) ascending, (c)-(d) descending, and (e)-(f) combined passes.

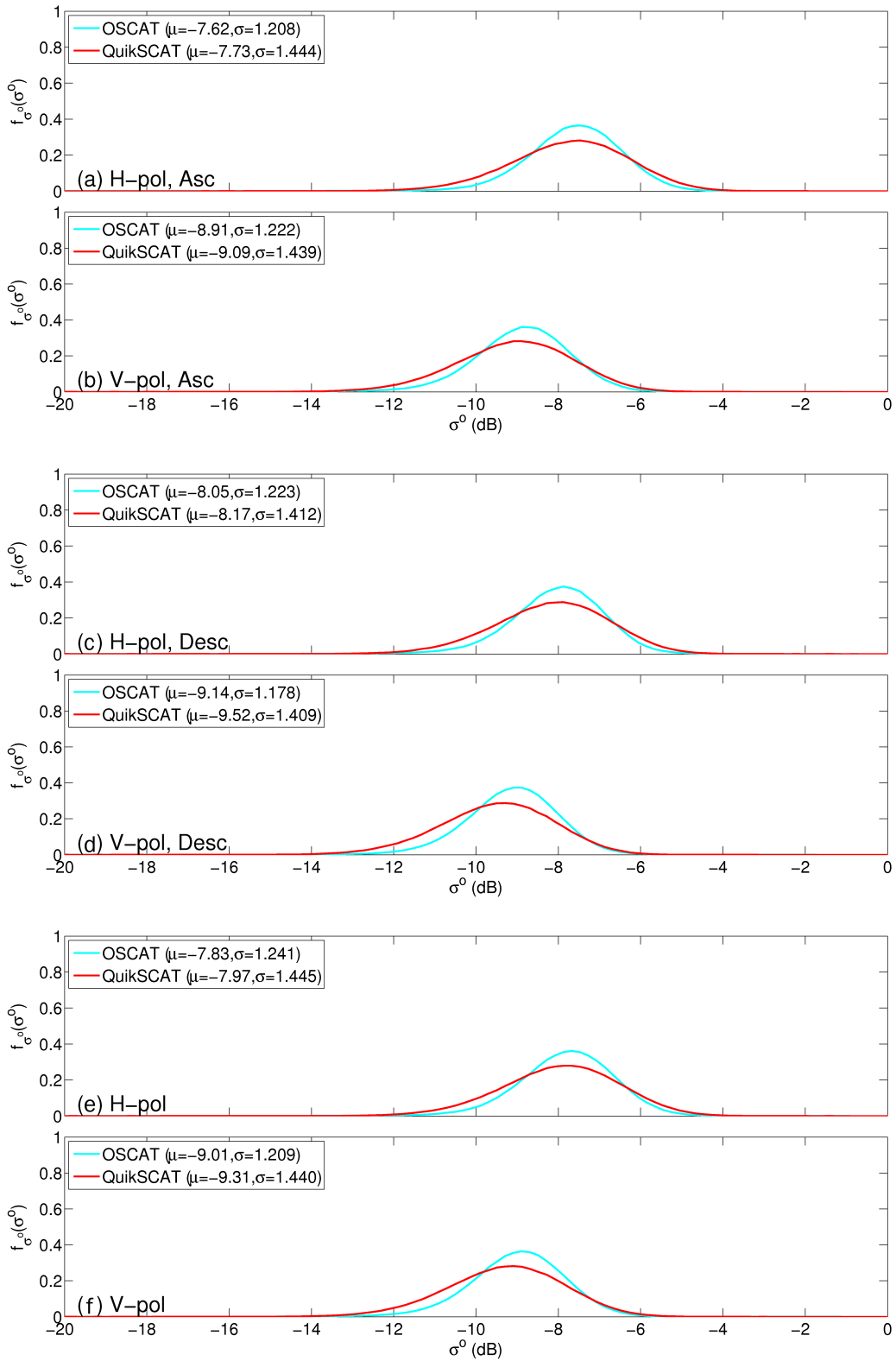


**Figure B.18:** Measurement distributions  $f_{\sigma^o}(\sigma^o)$  for normalized H- and V-pol slice measurements of the (a)-(b) ascending, (c)-(d) descending, and (e)-(f) combined passes.

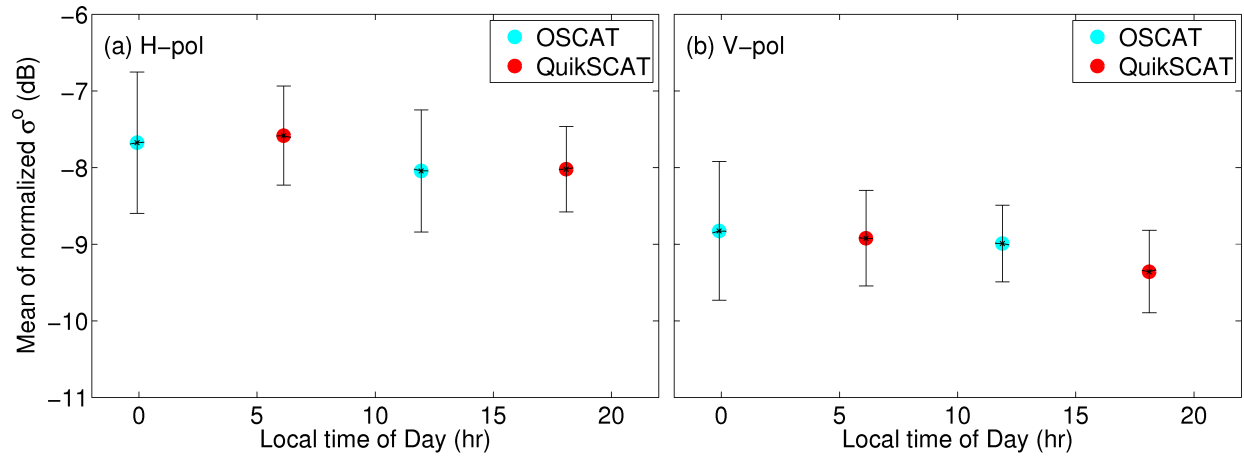


**Figure B.19:** Mean values of normalized egg  $\sigma^o$  from OSCAT and QuikSCAT versus local time of day.

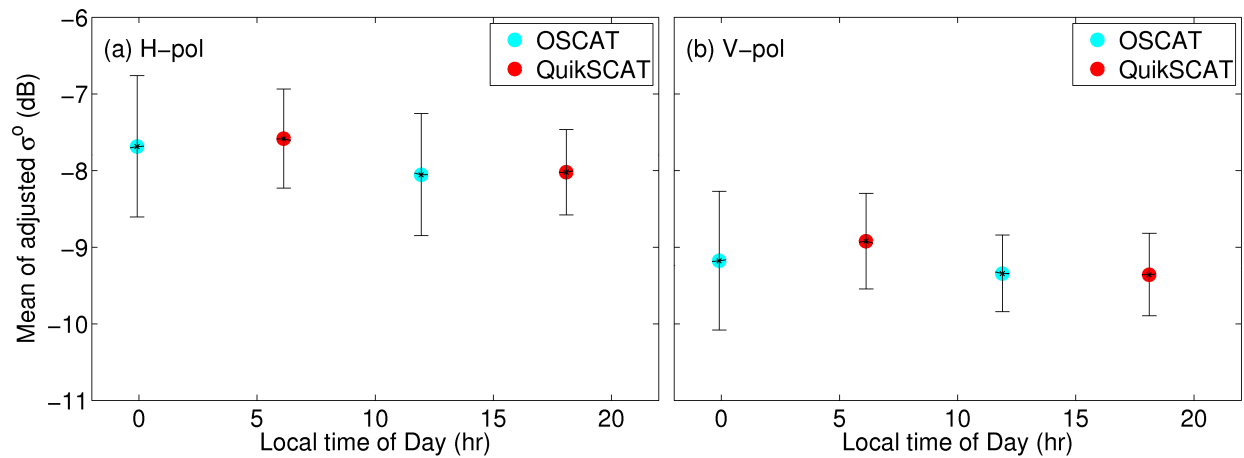


**Figure B.20:** Mean values of normalized egg  $\sigma^o$  from OSCAT and QuikSCAT versus local time of day after adjustment of OSCAT data by the calibration factors.

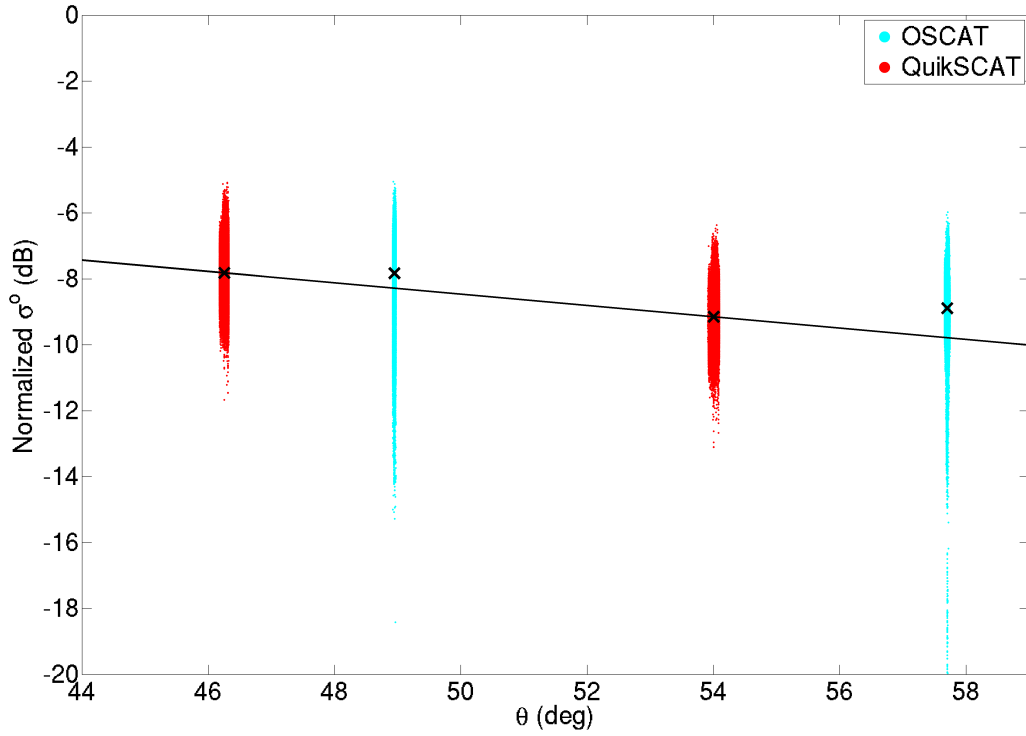


**Figure B.21:** Scatterplot of OSCAT and QuikSCAT normalized slice  $\sigma^o$  versus  $\theta$  for combined pass data of both beams. “x” marks the mean response of each beam.

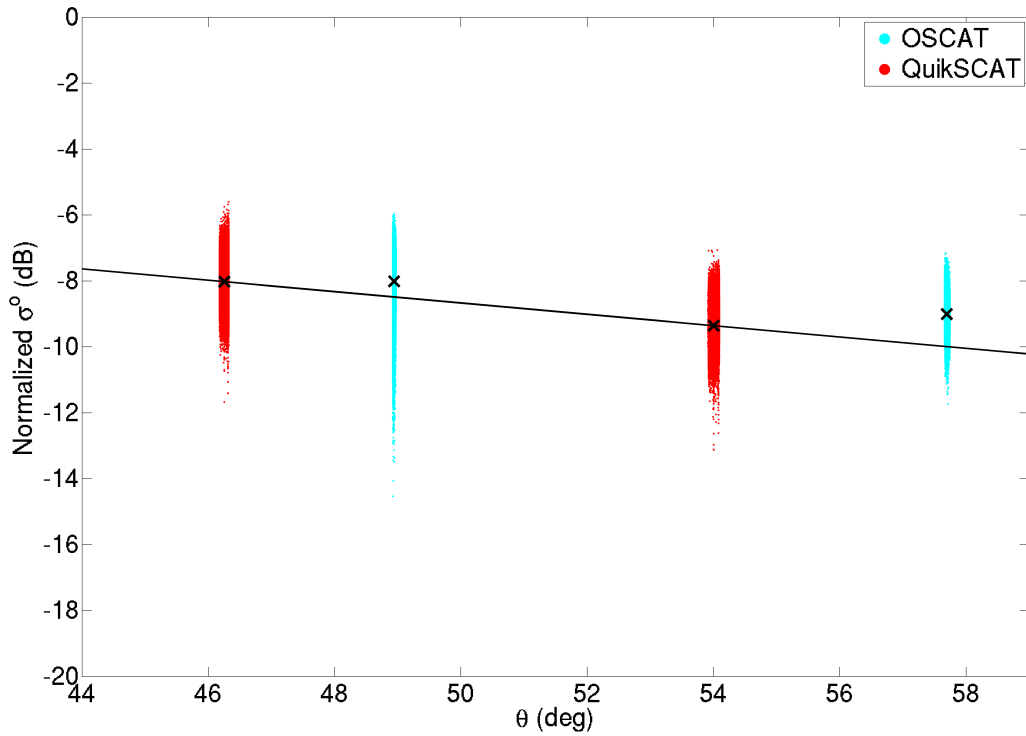


**Figure B.22:** Scatterplot of OSCAT and QuikSCAT normalized slice  $\sigma^o$  versus  $\theta$  for descending pass data of both beams. “x” marks the mean response of each beam.



## Appendix C

### Geolocation Error in OSCAT $\sigma^\circ$ Measurements

OSCAT L1B  $\sigma^\circ$  data is currently being used to make standard SCP products [18] for OSCAT, including SIR images. OSCAT SIR images are made the same way as QuikSCAT. In attempting to determine the effective resolution of OSCAT  $\mathcal{A}_h$ - and  $\mathcal{A}_v$ -SIR images, it was noticed that there is a significant blur present in regional daily SIR images.

In this appendix, I show that the cause of OSCAT SIR image blur is a longitudinal bias in the reported center location of  $\sigma^\circ$  measurements. This is demonstrated using ascending and descending  $\mathcal{A}_h$ - and  $\mathcal{A}_v$ -SIR images over the Peter I [68°50'50" S, 90°35'41" W], Bear (Bjørnøya) [74°25'30" N, 19°2' E], and Niue [19°3' S, 169°51'38" W] islands. Section C.1 presents  $\mathcal{A}_h$ - and  $\mathcal{A}_v$ -SIR images of the islands and discusses their implications. A simple algorithm to correct for the longitudinal location bias in SIR processing is described in Section C.2. A summary is provided in Section C.3.

#### C.1 Longitudinal Bias

I first eliminated the possibility of an antenna pointing bias being the cause of OSCAT SIR image blurring by examining separately ascending-fore, ascending-aft, descending-fore, and descending-aft SIR images for a 10 day period over the Peter I island. As the images did not exhibit a coinciding shift of the island corresponding to antenna scanning geometry, it was evident that an antenna pointing error bias was probably not the cause of blurring. However, common to all ascending images was a westerly shift of the island, and common to all descending images was an easterly shift of the island.

To further investigate this apparent pass-based longitudinal shift, I created ascending and descending SIR images which combine both fore and aft measurements over the islands.  $\mathcal{A}_h$ - and  $\mathcal{A}_v$ -SIR images of the islands made for JD 73-82 of 2011 are shown in Figures C.1-C.3, and for JD 266-275 of 2011 in Figures C.4-C.6. Along with the  $\mathcal{A}_h$ - and  $\mathcal{A}_v$ -SIR images of the islands are shown the squared differences of the SIR images. Ascending pass SIR images show the island to be shifted by a greater amount than for descending passes. The horizontal distances  $\Delta_x$  between the island centroids of the SIR images and the actual center of the island are shown in Table C.1. These values are based on approximations and they are expected to exhibit variability.

I subjectively estimate that the reported H-pol  $\sigma^\circ$  measurement locations have easterly longitudinal biases of  $\Delta_x = -9$  km for ascending and  $\Delta_x = 3$  km for descending passes, and V-pol  $\sigma^\circ$  measurements locations have easterly longitudinal biases of  $\Delta_x = -11$  km for ascending and  $\Delta_x = 3$  km for descending passes. This means that the total discrepancy in measurement longitude is over 12 km from ascending to descending pass. It is also impor-

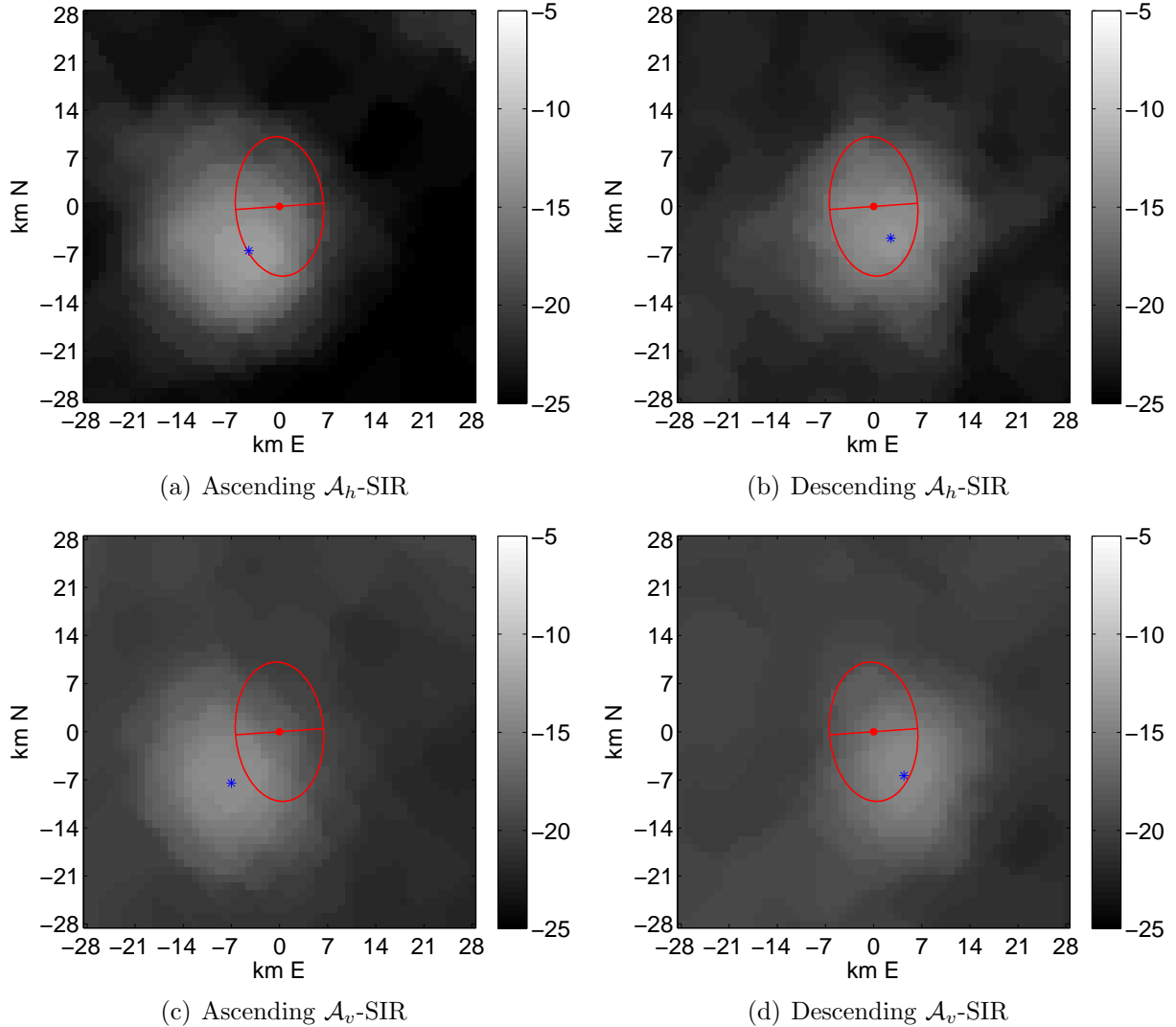


**Figure C.1:** Ascending and descending, slice (a)-(b)  $\mathcal{A}_h$ -SIR images and (c)-(d)  $\mathcal{A}_v$ -SIR images of the Bear island for JD 073-082 of 2011. The pixel resolution is 1.11 km/pix and the color scale is in dB. The blue asterisk marks the centroid of the SIR images as an estimate of the center of the island. The red dot signifies the actual center location of the island and the red line shows the island shape approximated by an ellipse.

tant to note that performing this same study on 2009 OSCAT L1B data yields the same longitudinal biases. This leads me to believe that this error has existed since the onset of OSCAT. Because the bias is present for islands at different latitudes, as demonstrated in the SIR images of the islands, I assume that the bias is not latitude dependent.

## C.2 Longitude Bias Correction Algorithm

To correct for the longitudinal biases, the  $i_{\text{th}}$  measurement longitude  $x_i$  is projected onto a tangent plane centered about the measurement [44], adjusted by the the appropriate

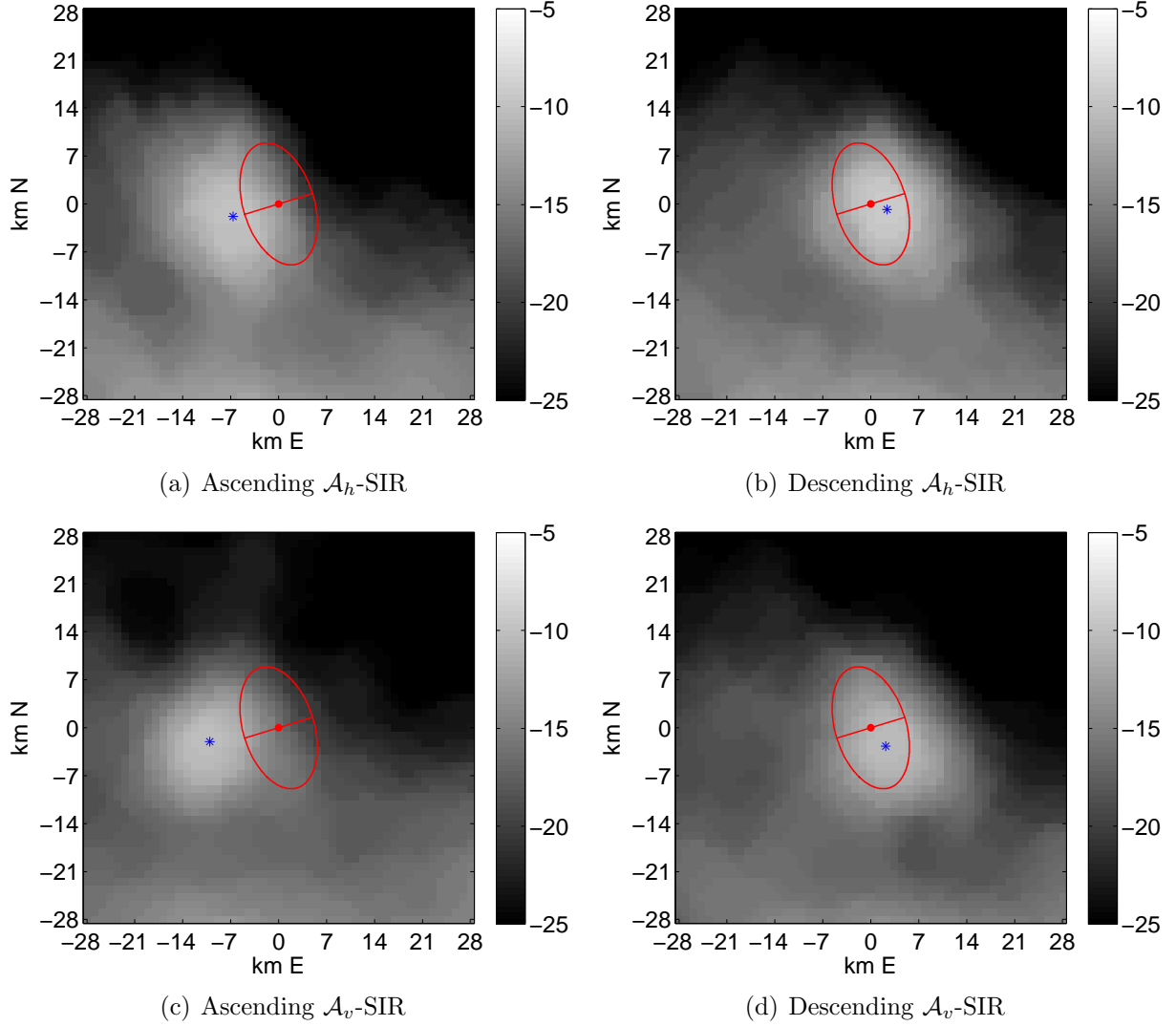


**Figure C.2:** Ascending and descending, slice (a)-(b)  $\mathcal{A}_h$ -SIR images and (c)-(d)  $\mathcal{A}_v$ -SIR images of the Peter I island for JD 073-082 of 2011. The pixel resolution is 1.11 km/pix and the color scale is in dB. The blue asterisk marks the centroid of the SIR images as an estimate of the center of the island. The red dot signifies the actual center location of the island and the red line shows the island shape approximated by an ellipse.

bias factor  $\Delta_x$  for the given pass, and then projected back to the surface of the Earth. Mathematically, this process is given by

$$x_i^c = x_i - \arcsin\left(\frac{\Delta_x}{R_{\text{Lat}}}\right), \quad (\text{C.1})$$

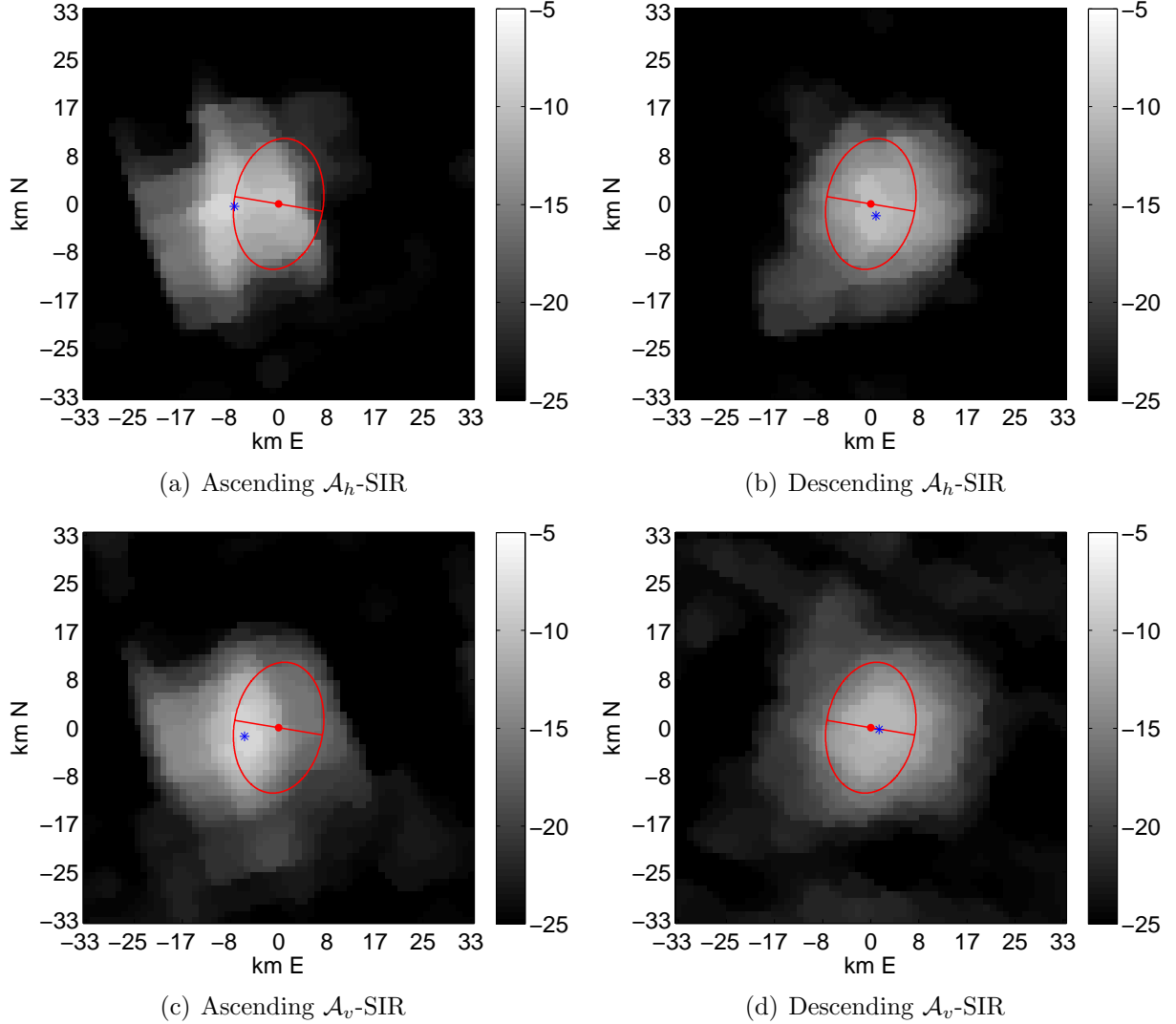


**Figure C.3:** Ascending and descending, slice (a)-(b)  $\mathcal{A}_h$ -SIR images and (c)-(d)  $\mathcal{A}_v$ -SIR images of the Niue island for JD 073-082 of 2011. The pixel resolution is 1.11 km/pix and the color scale is in dB. The blue asterisk marks the centroid of the SIR images as an estimate of the center of the island. The red dot signifies the actual center location of the island and the red line shows the island shape approximated by an ellipse.

where  $x_i^c$  is the corrected longitude position of the  $i_{\text{th}}$  measurement in degrees and  $R_{\text{Lat}}$  is the radius of the local latitude line. The radius of the local latitude line is calculated by

$$R_{\text{Lat}} = R_E \cos(y_i), \quad (\text{C.2})$$

where  $y_i$  is the latitude of the  $i_{\text{th}}$  measurement given in degrees, and  $R_E$  is the local radius of the Earth

$$R_E = (1 - K_{\text{flat}} \sin^2(y_i)) R_a, \quad (\text{C.3})$$

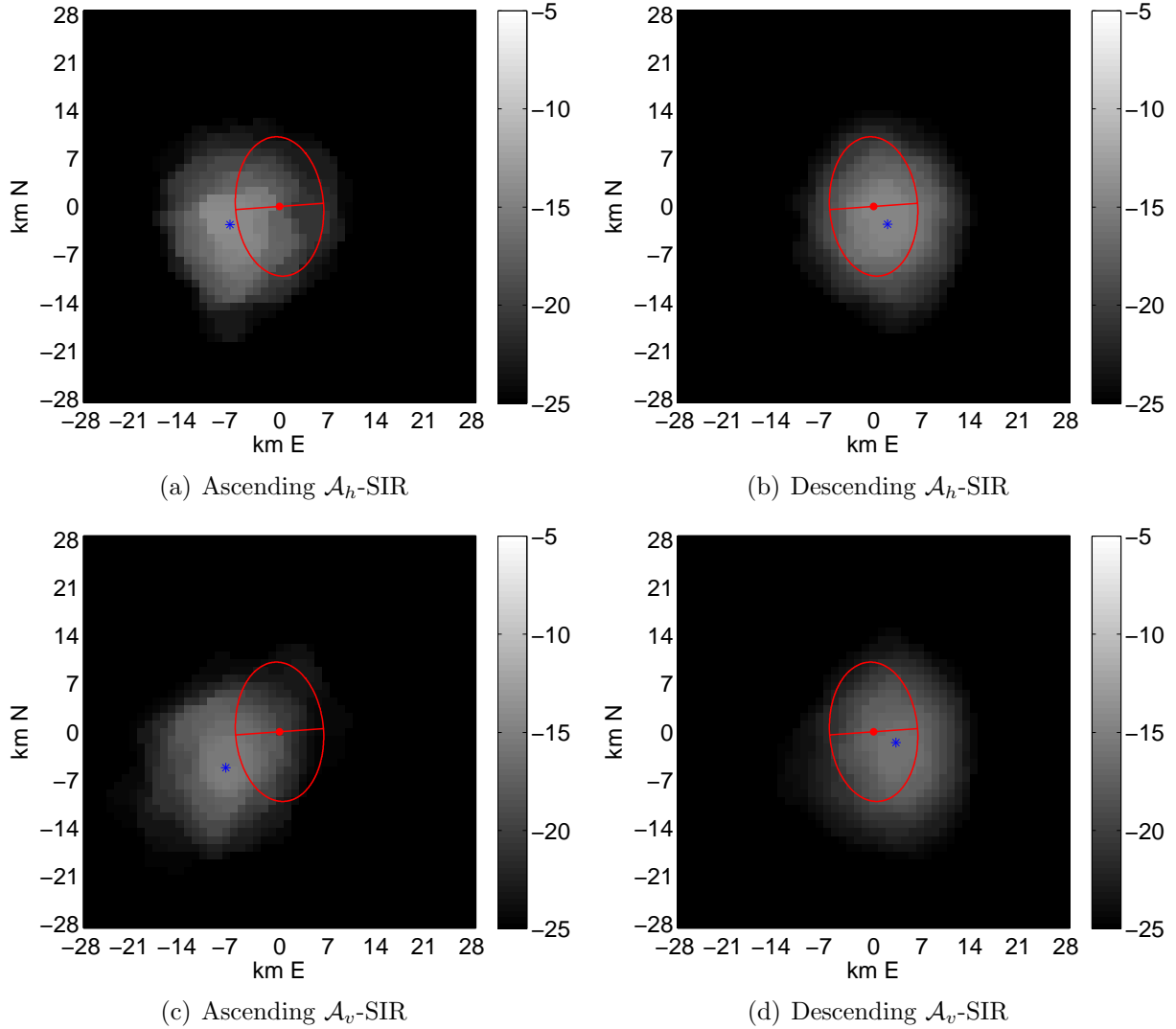


**Figure C.4:** Ascending and descending, slice (a)-(b)  $\mathcal{A}_h$ -SIR images and (c)-(d)  $\mathcal{A}_v$ -SIR images of the Bear island for JD 266-275 of 2011. The pixel resolution is 1.11 km/pix and the color scale is in dB. The blue asterisk marks the centroid of the SIR images as an estimate of the center of the island. The red dot signifies the actual center location of the island and the red line shows the island shape approximated by an ellipse.

where  $K_{flat} = 1/298.257$  is the Earth flatness constant and  $R_a = 6378.1363$  km is the Semi-major axis of the Earth. Applying this simple fix in creation of Antarctic  $\mathcal{A}_h$ -SIR images used in iceberg tracking has significantly decreased blurring and increased the effective resolution.

### C.3 Summary

From ascending and descending pass SIR images over the Peter I island, it has been shown that the OSCAT  $\sigma^\circ$  measurement longitude has errors from ascending to descending

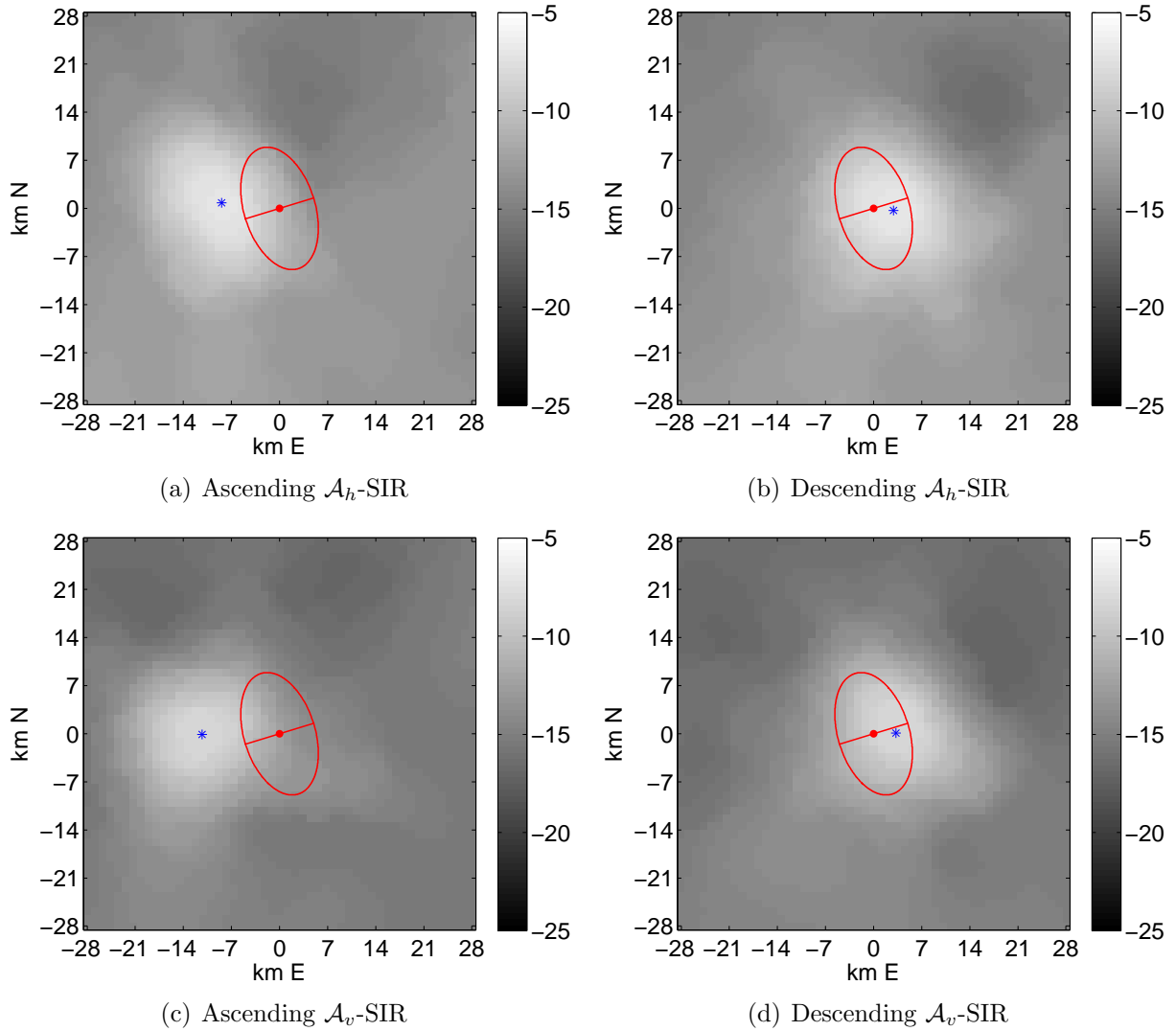


**Figure C.5:** Ascending and descending, slice (a)-(b)  $\mathcal{A}_h$ -SIR images and (c)-(d)  $\mathcal{A}_v$ -SIR images of the Peter I island for JD 266-275 of 2011. The pixel resolution is 1.11 km/pix and the color scale is in dB. The blue asterisk marks the centroid of the SIR images as an estimate of the center of the island. The red dot signifies the actual center location of the island and the red line shows the island shape approximated by an ellipse.

pass. It is recommend that this be fixed in subsequent versions of calibrated OSCAT data in order to provide for more accurate scientific studies.

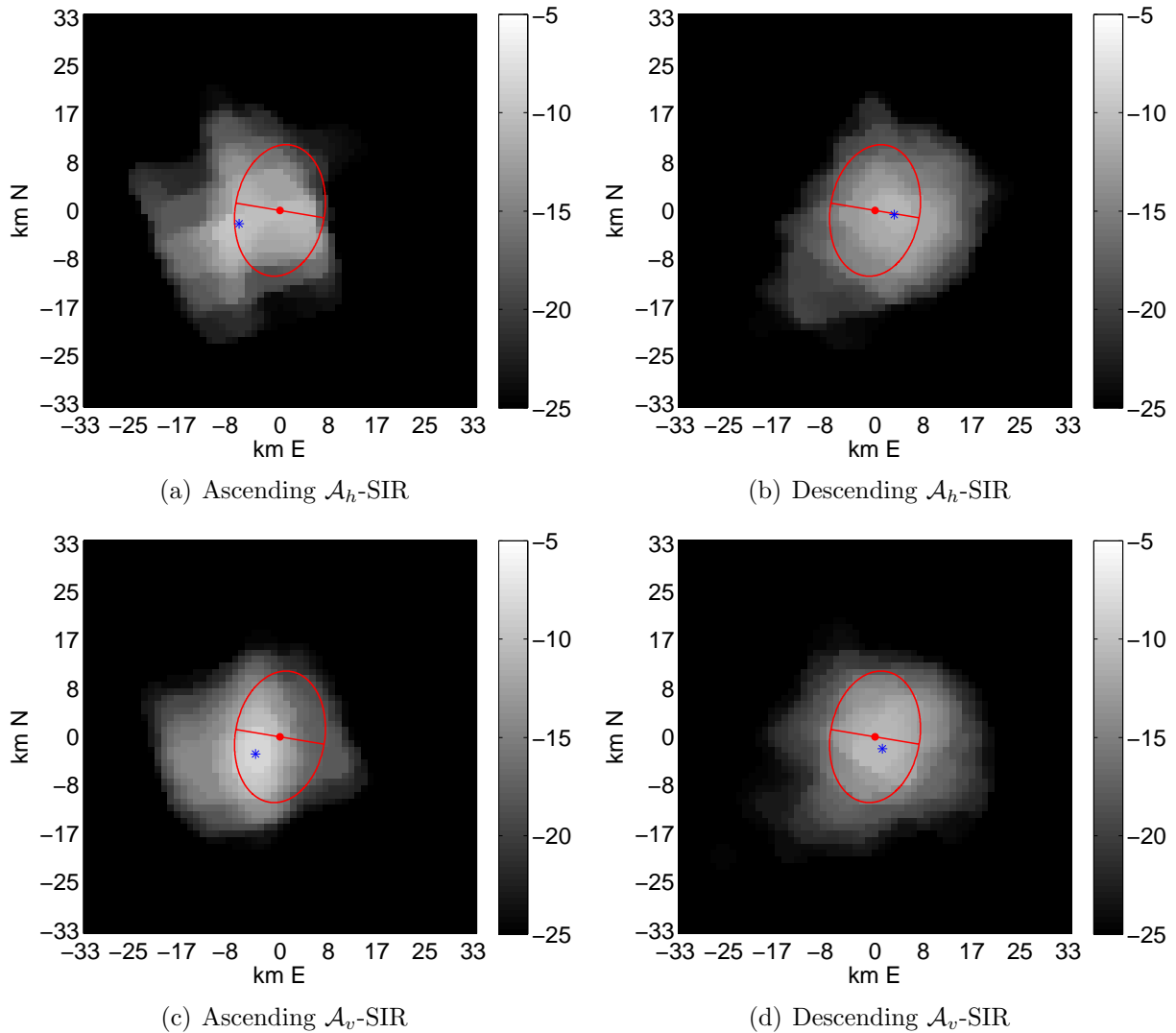


**Figure C.6:** Ascending and descending, slice (a)-(b)  $\mathcal{A}_h$ -SIR images and (c)-(d)  $\mathcal{A}_v$ -SIR images of the Niue island for JD 266-275 of 2011. The pixel resolution is 1.11 km/pix and the color scale is in dB. The blue asterisk marks the centroid of the SIR images as an estimate of the center of the island. The red dot signifies the actual center location of the island and the red line shows the island shape approximated by an ellipse.

**Table C.1:** Horizontal distances  $\Delta_x$  (km) between the island centroids of the SIR images and their actual geographical center locations.

JD	Island	Ascending		Descending	
		H-pol	V-pol	H-pol	V-pol
73-82	Bear	-4.4	-6.9	2.5	4.4
	Peter I	-6.6	-10.0	2.4	2.2
	Niue	-7.7	-5.9	0.9	1.5
266-275	Bear	-7.1	-7.8	2.0	3.2
	Peter I	-8.6	-11.2	2.9	3.2
	Niue	-7.0	-4.2	3.3	1.3

## Appendix D

### Estimation of the OSCAT Antenna Azimuth Angle

The cross-track density of  $\sigma^\circ$  measurements varies for conically scanning pencil-beam scatterometers, with more measurements at the swath edge than at the swath center due to the rotation of the antenna. As a result, there is a larger span of azimuth angles  $\phi$  at the swath edge. Averaging of  $\sigma^\circ$  over a large span of  $\phi$  at the swath edge can expose anisotropy in the  $\sigma^\circ$  response at those locations, introducing artifacts near the swath edges in SIR  $\sigma^\circ$  images. This results in the undesirable presence of clearly visible swath edges in the images.

To ameliorate undesirable artifacts near the swath edges,  $\sigma^\circ$  measurements at the swath edge are not used in generating SIR images. This is done by discarding measurements with antenna azimuth angles  $\varphi$  within  $\pm\chi$  of orthogonal to the along-track direction as shown in Figure D.1, where  $\chi$  is the azimuth exclusion angle given in degrees. An antenna exclusion angle of  $\chi = 15^\circ$  was subjectively chosen for QuikSCAT based on a tradeoff of computation and image artifact reduction. The same value for  $\chi$  is used in OSCAT SIR image processing.

Implementing this method of swath edge measurement exclusion requires  $\varphi$  for each measurement. This complicates the process for OSCAT data because the parameter  $\varphi$  is not provided in the first two versions of OSCAT L1B data. The parameter is provided in the most recent L1B data as a part of the change in data format, however it suffers from a permanent rotation bias caused by flying the aircraft at an off-angle with relation to the flight path direction as shown in Figure D.2. Therefore, to allow for accurate swath edge measurement exclusion in both new and old data, a procedure for calculating  $\varphi$  from alternate common parameters between the L1B datasets is necessary. In this appendix, a method of estimating the  $\varphi$  is presented in Section D.1 and a brief summary is given in Section D.2.

#### D.1 Estimation of the Antenna Azimuth Angle

Because the antenna rotation is synchronized with the PRF, the antenna footprint number  $n$  of a measurement for a telemetry frame is fixed at a given  $\varphi$ . The antenna footprint number is a number sequentially assigned to cell measurements taken during one telemetry frame, where a telemetry frame is defined as one  $360^\circ$  rotation of the antenna starting at  $-90^\circ$  from the along track direction. The first measurement in a telemetry frame is assigned  $n = 0$ , and the last measurement is assigned  $n = 562$ . Measurements are taken alternately between beams with V-pol being first. Thus, V-pol measurements are assigned even values of  $n$  over the range  $[0, 562]$  and H-pol measurements are assigned odd values of  $n$  over the range  $[1, 561]$ . There is one more V-pol measurement than H-pol measurement in every telemetry frame.

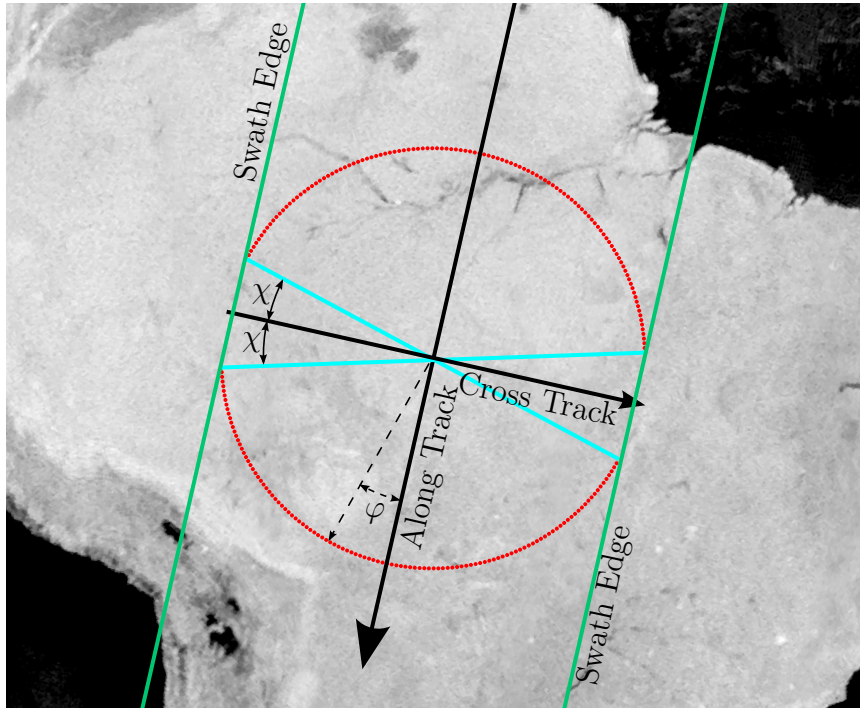


**Figure D.1:** A diagram of the along track and cross track geometry with the antenna azimuth angle and antenna azimuth exclude angles.

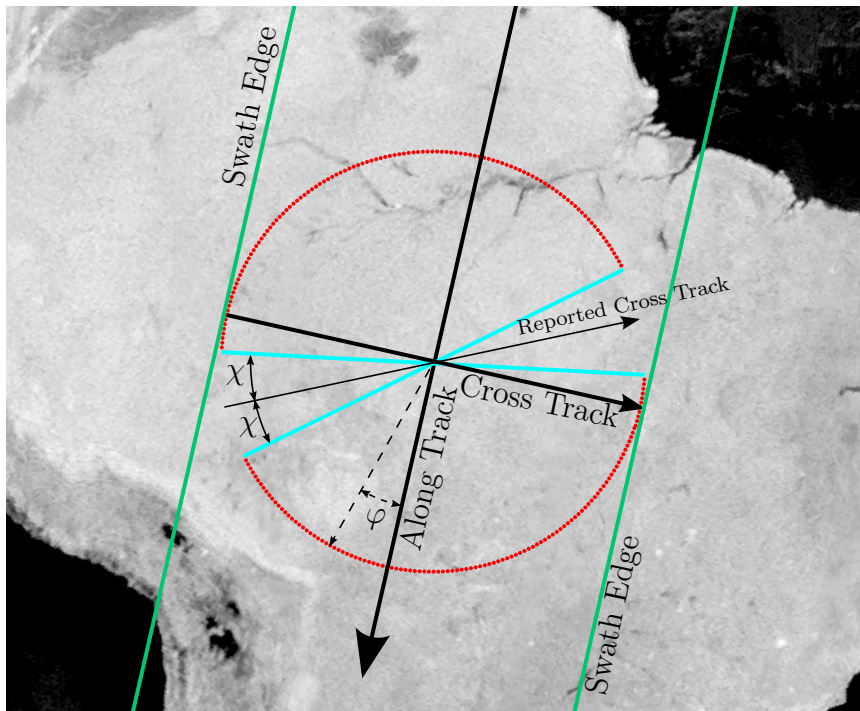


**Figure D.2:** A diagram of the along track and cross track geometry with the antenna azimuth angle and antenna azimuth exclude angles.

Through a simple procedure,  $\varphi$  can be estimated from  $n$  for OSCAT measurements since  $n$  is directly related to  $\varphi$ . For the  $i^{\text{th}}$  measurement,  $n$  is first converted into degrees and rotated so that  $0^\circ$  aligns with the along-track direction by

$$\hat{\varphi}_i = n_i \left( \frac{360^\circ}{n^{\max}} \right) - 81^\circ, \quad (\text{D.1})$$

where  $n^{\max} = 562$  and  $\hat{\varphi}_i$  is the estimated  $\varphi$  of the  $i^{\text{th}}$  measurement, only shifted by  $81^\circ$  degrees due to the off-angle flight of the aircraft. Using Eq. (D.1),  $\hat{\varphi} = 0^\circ$  is aligned with the along-track direction directly over the poles at  $\pm 90^\circ$  latitude. Through validation of the  $\hat{\varphi}$  over the rest of the planet, it was discovered that  $\hat{\varphi}$  rotates by  $-5^\circ$  at the ascending node  $+5^\circ$  at the descending node. The ascending/descending pass-based latitude dependence of  $\hat{\varphi}$  is corrected for by

$$\hat{\varphi}_i = \hat{\varphi}(y_i) \pm \frac{(90^\circ - |y_i|)}{90^\circ} (5^\circ), \quad (\text{D.2})$$

where  $y_i$  is the latitude of the  $i^{\text{th}}$  measurement.

## D.2 Summary

This appendix presents a simple method for obtaining estimates of the antenna azimuth angle from antenna footprint number. The method is used for swath edge measurement exclusion in SIR processing to eliminate artifacts near the swath edge in SIR images. This method is currently applied to all OSCAT SIR processing. Through application of this method, swath edge measurement exclusion properly eliminates OSCAT measurements near the swath edge over the entire planet, as shown in Figure D.1. Because the fore/aft flag associated with the measurements also suffers from the same rotation due to off-angle flight of the aircraft,  $\hat{\varphi}$  is used to reset the fore/aft flag during SIR processing. This has significantly improved the quality of OSCAT SIR images.